

Mechanistic studies of DNP and applications of hyperpolarized probes to study renal physiology and metabolism

Présentée le 4 juin 2021

Faculté des sciences de base
Laboratoire Leenaards-Jeantet d'imagerie fonctionnelle et métabolique
Programme doctoral en physique

pour l'obtention du grade de Docteur ès Sciences

par

Alice RADAELLI

Acceptée sur proposition du jury

Prof. F. Carbone, président du jury
Prof. R. Gruetter, H. A. I. Yoshihara, directeurs de thèse
Prof. P. R. Jensen, rapporteuse
Prof. C. Wagner, rapporteur
Prof. J.-Ph. Ansermet, rapporteur

Abstract

Dissolution dynamic nuclear polarization (dDNP) is a powerful technique that enhances the magnetic resonance signal of nuclear spins by several orders of magnitude. DNP relies on the principle of cross-relaxation by electron spins driven out of equilibrium to enhance nuclear polarization. When coupled to magnetic resonance spectroscopy/imaging (MRS/I), infusion of ^{13}C -labeled tracers hyperpolarized via DNP *in vivo* provides real-time estimates of metabolic fluxes, physiological parameters and/or tissue perfusion.

The present work focuses on fundamental aspects of DNP, in particular how sample composition affects the DNP of low-gamma nuclei, as well as on *in vivo* dDNP applications targeting renal metabolism and physiology.

The DNP properties of the SA-BDPA radical were studied in a sample of ^{13}C -urea. SA-BDPA, a water-soluble derivative of BDPA, is characterized by a small g -anisotropy and unresolved hyperfine coupling to protons. As a result, at 6.7 T, 1.1 K its ESR linewidth is much smaller than the ^{13}C Larmor frequency, which enabled the observation for the first time of ^{13}C DNP *via* the solid effect and pure thermal mixing, the latter defined as the process where the electron non-Zeeman reservoir alone provides the energy required for triple-spin flips.

The effect of solvent deuteration on ^6Li DNP and radical ESR properties was studied in $^6\text{LiCl}$ water:glycerol solutions doped with either the nitroxide radical TEMPOL or the trityl radical OX063. Unexpectedly, the TEMPOL-doped samples polarized better than the trityl-doped ones. Across all samples, the relationship between the degree of solvent deuteration with the buildup time constant and polarization level was notably different from what has been reported for ^{13}C . This behavior is indicative of DNP *via* a combination of the cross effect and thermal mixing mechanisms.

The uptake and metabolism of hyperpolarized L-[1- ^{13}C]alaninamide was investigated in the rat kidney *in vivo*. This probe of aminopeptidase N, which can play a role in tumor growth, was previously studied *in vitro*. Our study showed that alanine production from alaninamide also occurs *in vivo*, however, with spectral overlap of substrate and product. Alaninamide, having a pK_a of 7.9, proved to be sensitive to local pH. Three spectral peaks, corresponding to at least three environments with different pH values, could be observed in the kidney. The two peaks at higher pH were assigned to the blood extra- and (partially) intracellular compartments, while the third one was mainly in the inner part of the kidney. Finally, alaninamide

Abstract

was shown to also be sensitive to dissolved CO₂, with the rapid formation of a carbamate adduct following infusion.

The renal metabolism of D-[1-¹³C]alanine by D-amino acid oxidase (DAO) was also studied. Conversion of hyperpolarized D-alanine to pyruvate and further metabolism to lactate and bicarbonate was observed in the kidney only when DAO was not inhibited. DAO activity could also be detected in blood, where leukocytes express the enzyme, but not in the brain and liver, in line with their lower DAO activity.

Overall, this thesis provides additional insight into how the experimental conditions can favor a particular DNP mechanism over another. It also significantly expands the scope of *in vivo* dDNP applications, showing that additional enzyme-catalyzed processes can be detected, along with the potential of amino-acid based hyperpolarized ¹³C sensors for physiological studies.

Keywords: Nuclear magnetic resonance (NMR), dissolution dynamic nuclear polarization (d-DNP), ¹³C magnetic resonance spectroscopy and imaging (MRS, MRI), electron spin resonance (ESR), polarizing agents, metabolism, kidney, aminopeptidase N (APN), pH mapping, D-amino acid oxidase (DAO).

Resumé

La polarisation dynamique nucléaire avec dissolution (PDN-d) est une puissante méthode permettant d'accroître le signal de résonance magnétique de spins nucléaires de plusieurs ordres de grandeur. Afin d'améliorer la polarisation des noyaux, la PDN utilise le principe de relaxation croisée entre ces derniers et des électrons non appariés excités hors de leur état d'équilibre. Couplée à l'imagerie ou la spectroscopie par résonance magnétique (IRM ou SRM), l'infusion *in vivo* de traceurs marqués au carbone 13 (^{13}C) et hyperpolarisés par la PDN permet notamment d'estimer en temps réel des flux métaboliques, des paramètres physiologiques, ou bien encore la perfusion tissulaire.

Le présent travail porte sur des aspects fondamentaux de la PDN, en particulier comment la composition de l'échantillon affecte la PDN de noyaux avec un petit rapport gyromagnétique, ainsi que sur des applications *in vivo* de la PDN visant à mesurer la physiologie et le métabolisme rénaux.

Les propriétés de PDN du radical SA-BDPA ont été étudiées dans un échantillon d'urée ^{13}C . Le SA-BDPA, un dérivé soluble dans l'eau du BDPA, est caractérisé par une faible anisotropie **g** ainsi qu'un couplage hyperfin non-résolu avec les protons. À 6.7 T et 1.1 K, la largeur de son spectre de résonance paramagnétique électronique (RPE) est largement inférieure par rapport à la fréquence de Larmor du ^{13}C , permettant, pour la première fois, d'observer distinctement la PDN du ^{13}C par l'effet solide et par le mélange thermique pur, ce dernier étant défini par le processus selon lequel l'énergie nécessaire aux triples inversions de spins est uniquement fournie par les électrons du réservoir non-Zeeman.

L'effet de la deutération du solvant sur la PDN du lithium 6 (^6Li) ainsi que les propriétés RPE du radical a été étudié dans des solutions eau-glycérol de 6LiCl dopées avec le radical nitroxyle TEMPOL ou bien avec le radical trityle OX063. De façon inattendue, les échantillons dopés au TEMPOL polarisaient mieux que ceux composés de trityle. Parmi tous les échantillons, la relation entre le degré de deutération du solvant et la constante de temps d'accumulation ainsi que le niveau de polarisation était particulièrement différente de ce qui a été précédemment rapporté pour le ^{13}C . Cette tendance indique une PDN par une combinaison des mécanismes d'effet de croisement et de mélange thermique.

L'assimilation et le métabolisme du L-[1- ^{13}C]alaninamide hyperpolarisé ont été étudiés *in vivo* dans le rein du rat. Cette sonde de l'enzyme aminopeptidase N, qui favorise la crois-

sance tumorale, a été précédemment examinée *in vitro*. Notre étude montre que la production d'alanine à partir de l'alaninamide se déroule également *in vivo*, cependant avec un chevauchement entre les spectres du substrat et du produit. L'alaninamide, avec un pK_a de 7.9, s'est révélé être sensible au pH local. Trois pics spectraux, correspondant à au moins trois environnements avec différents pH, ont été observés dans le rein. Les deux pics à des pH élevés ont été attribués aux compartiments de sang extracellulaire et (partiellement) intracellulaire, tandis que le troisième représentait principalement la partie interne du rein. Finalement, l'alaninamide s'est montré être réactif avec le CO_2 dissous, formant rapidement un adduit carbamate suivant l'infusion.

Le métabolisme rénal du D-[1- ^{13}C]alanine par la D-aminoacide oxydase (DAAO) a également été étudié. Dans le rein, la conversion du D-alanine hyperpolarisé en pyruvate ainsi que le métabolisme subséquent en lactate et bicarbonate ont été observés uniquement lorsque le DAAO n'était pas inhibé. L'activité du DAAO a également été détectée dans le sang, où cette enzyme est exprimée par les leucocytes, mais pas dans le cerveau ni dans le foie en raison de leur plus faible activité de DAAO.

Globalement, cette thèse fournit de nouvelles connaissances sur la façon dont les conditions expérimentales permettent de favoriser un mécanisme particulier de PDN par rapport à un autre. Elle élargit également considérablement la portée des applications *in vivo* de la PDN, montrant la possibilité de détecter de nouveaux processus enzymatiques, de même que le potentiel des acides aminés en tant que senseurs hyperpolarisés pour des études physiologiques.

Mots clefs: Résonance magnétique nucléaire (RMN), polarisation dynamique nucléaire avec dissolution (PDN-d), ^{13}C imagerie et spectroscopie par résonance magnétique (IRM ou SRM), résonance paramagnétique électronique (RPE), agents polarisants, métabolisme, rein, aminopeptidase N (APN), cartographie du pH, D-aminoacide oxydase (DAAO).

Contents

Abstract (English/Français)	i
List of abbreviations	ix
Outline	1
1 Introduction	5
1.1 Sensitivity in NMR	5
1.2 Hyperpolarization techniques	6
1.3 Dissolution DNP	7
1.3.1 dDNP <i>in vivo</i> applications	8
1.4 Conclusions	13
2 DNP mechanisms	15
2.1 Spin Hamiltonian	15
2.2 Solid effect	15
2.2.1 The fundamental transition of solid effect	16
2.3 DNP <i>via</i> triple spin flips: thermal mixing and cross effect	19
2.3.1 Thermodynamic model of thermal mixing	21
2.4 Conclusions	24
3 dDNP: practical considerations	25
3.1 System requirements	25
3.1.1 DNP polarizer	25
3.1.2 LOD-ESR	27
3.2 Sample composition	27
3.3 Sample dissolution	29
3.4 Conclusions	29
4 ¹³C dynamic nuclear polarization using SA-BDPA at 6.7 T and 1.1 K: coexistence of pure thermal mixing and well-resolved solid effect	31
4.1 Introduction	35

Contents

4.2	Methods	36
4.2.1	Sample preparation	36
4.2.2	LOD-ESR measurements	36
4.2.3	DNP experiments	37
4.2.4	Estimation of minimum inter-radical distance	37
4.3	Results	38
4.4	Discussion	40
4.5	Conclusions	44
5	Effects of glassing matrix deuteration on ^6Li dynamic nuclear polarization	45
5.1	Introduction	49
5.2	Methods	50
5.2.1	Sample formulation	50
5.2.2	Hyperpolarization	51
5.2.3	LOD-ESR measurements	51
5.2.4	Data analysis	52
5.3	Results	52
5.4	Discussion	54
5.5	Conclusions	59
6	Probing renal pH and aminopeptidase N activity using hyperpolarized L-[1-^{13}C]alaninamide	61
6.1	Introduction	65
6.1.1	Aminopeptidase N	65
6.1.2	Role of the kidney in pH regulation	65
6.1.3	Measurement of renal pH	66
6.1.4	Carbamate formation in blood	66
6.2	Methods	67
6.2.1	Chemicals	67
6.2.2	Alaninamide synthesis	68
6.2.3	Alaninamide titration	68
6.2.4	Hyperpolarization	68
6.2.5	Polarization measurements	69
6.2.6	Animals	69
6.2.7	<i>In vivo</i> hyperpolarized ^{13}C MRS/I	70
6.2.8	<i>Ex vivo</i> hyperpolarized ^{13}C MRS	74
6.2.9	Carbamate characterization	74
6.3	Results	75
6.3.1	Alaninamide characterization	75

6.3.2	<i>In vivo</i> hyperpolarized ^{13}C MRS/I	75
6.3.3	Carbamate characterization and alaninamide in blood cells	83
6.3.4	<i>Ex vivo</i> hyperpolarized ^{13}C NMR	88
6.4	Discussion	89
6.4.1	Probe of APN activity	89
6.4.2	pH sensitivity	89
6.4.3	Carbamate production	93
6.5	Conclusions	94
7	<i>In vivo</i> detection of D-amino acid oxidase with hyperpolarized D-[1-^{13}C]alanine	97
7.1	Introduction	101
7.2	Methods	101
7.2.1	Hyperpolarization	101
7.2.2	Concentration measurements	102
7.2.3	Animals	102
7.2.4	^{13}C MRS acquisition and data analysis	103
7.3	Results	103
7.4	Discussion	108
7.5	Conclusions	111
8	Conclusions and outlook	113
	Appendices	117
A	^{13}C dynamic nuclear polarization using SA-BDPA at 6.7 T and 1.1 K: coexistence of pure thermal mixing and well-resolved solid effect	119
A.1	Radical concentration measurements	119
A.2	Derivation of the cut-off frequency Δ_0	119
B	Probing renal pH and aminopeptidase N activity using hyperpolarized L-[1-^{13}C]alaninamide	123
B.1	Alaninamide characterization	123
B.1.1	^1H NMR spectra of L-[1- ^{13}C]alaninamide methyl ester $\cdot \text{HCl}$ and L-[1- ^{13}C]alaninamide $\cdot \text{HCl}$	123
B.1.2	Supplemental titration curves	125
B.2	Flow suppression data	125
B.3	Hyperpolarized [1- ^{13}C]glycinamide in the heart	128
C	Flow suppression experiments with hyperpolarized [1-^{13}C]pyruvate: proof of concept	129

Contents

D	Comparison of hyperpolarized ^{13}C 2D-CSI images over the left and right kidney	135
E	<i>In vivo</i> detection of D-amino acid oxidase with hyperpolarized D-[1-^{13}C]alanine	139
E.1	Chiral purity of the D- and L-alanine sample preparations	139
E.2	<i>In vivo</i> and <i>in vitro</i> experiments	141
	Acknowledgements	159
	List of publications and conference proceedings	161
	Curriculum Vitae	163

List of abbreviations

ACZ	acetazolamide
AKI	acute kidney injury
ALT	alanine aminotransferase
APN	aminopeptidase N
AUC	area under the curve
bipg	bipolar gradient
CA	carbonic anhydrase
CE	cross effect
CNS	central nervous system
CSI	chemical shift imaging
DAO	D-amino acid oxidase
dDNP	dissolution dynamic nuclear polarization
DQ	double quantum
dSE	double spin-echo
ELDOR	electron double resonance
ESR	electron spin resonance
FAD	flavin adenine dinucleotide
FD	fully deuterated
FID	free induction decay
FOV	field of view
FP	fully protonated
FWHM	full width at half maximum
LDH	lactate dehydrogenase
LOD-ESR	longitudinally-detected electron spin resonance
MAS	magic angle spinning
MRI	magnetic resonance imaging
MRS	magnetic resonance spectroscopy
MW	molecular weight
NMDA	N-methyl-D-aspartate
NMR	nuclear magnetic resonance

Contents

PA	pulse-acquire
PCT	proximal convoluted tubule
PD	partially deuterated
PDH	pyruvate dehydrogenase
PDK	pyruvate dehydrogenase kinase
PHIP	parahydrogen-induced polarization
PMN	polymorphonuclear
rf	radio-frequency
SE	solid effect
SEOP	spin-exchange optical pumping
SFP	sterile fluid path
SNR	signal-to-noise ratio
TLC	thin layer chromatography
TM	thermal mixing
VTI	variable temperature insert
ZA	zymonic acid
ZQ	zero quantum

Outline

Aim

One of the main limitations of magnetic resonance (MR) of low-gamma nuclei is their intrinsic low sensitivity, that results in poor signal-to-noise ratio and long scan times. Such limitation can be overcome by using hyperpolarized techniques. Among them, dissolution dynamic nuclear polarization (dDNP) has gained a lot of attention as it boosts the signal of any spin-active isotope of several orders of magnitude. While the DNP process requires low temperatures and high magnetic fields, it was recently demonstrated that the spin order can be transiently maintained in liquid-state by rapidly dissolving the sample with a pressurized solvent in a suitably high field. When coupled with conventional MR, dDNP allows to probe the real-time metabolism, physiology and/or perfusion of a targeted tissue.

The aim of the present research project is two-fold: on one side is gaining further understanding of how the sample formulation influences the low-gamma nuclei DNP process and performance. In this regard, the effects of glassing solvent deuteration and radical choice were investigated. Two test samples were considered: ^{13}C urea in water:glycerol doped with SA-BDPA, a radical that to date had not been thoroughly studied as a polarizing agent under dDNP conditions, and $^6\text{LiCl}$ in water:glycerol with different solvent deuteration degrees and doped with either TEMPOL or trityl OX063. On the other side is characterizing the *in vivo* renal uptake of two novel probes to be used as markers of kidney physiology and function. The two investigated substrates are D-[1- ^{13}C]alanine to detect D-amino acid oxidase activity, and L-[1- ^{13}C]alaninamide to probe renal pH and aminopeptidase N activity. The structure of the thesis therefore consists of two blocks dedicated to the two macro themes of dDNP: how does the polarization transfer process take place and how do the different parameters influence it, and to what extent can DNP be used in *in vivo* studies.

Outline of the thesis

The first three chapters of the manuscript provide an introduction to dissolution DNP: the reasons behind the development of the technique, as well as an overview of some of the most relevant applications are discussed in **Chapter 1**. The mechanisms that drive the transfer of polarization from electrons to nuclei in static conditions are described in **Chapter 2**. Finally, system requirements and experimental methods are described in **Chapter 3**.

The experimental studies addressed at shedding light on how the electronic and nuclear spin pool properties affect the DNP process are then reported.

Chapter 4 describes the ^{13}C DNP properties of SA-BDPA, a sulfonated water-soluble derivative of BDPA. This radical, which has a particularly small g -anisotropy resulting in a narrow ESR spectrum primarily broadened by dipolar interactions, is a good candidate for observing DNP *via* pure thermal mixing. From an experimental point of view, when polarizing low-gamma nuclei, the relative contributions of thermal mixing and cross effect to the DNP process usually cannot be readily determined. With nitroxide radicals, thermal mixing was shown to be quenched if a suitably low radical concentration is used, owing to a dipolar coupling between electrons not sufficient to promote triple-spin flip transitions. The opposite, i.e. DNP occurring solely *via* thermal mixing, requires a radical with an electron spin resonance (ESR) linewidth smaller than the Larmor frequency of the nuclear species of interest and a molecular structure that allows for the possibility of having radicals closely packed together in space, and, to date, has yet to be observed.

In **Chapter 5** the high-field DNP properties of another low-gamma nucleus, ^6Li , are presented as a function of degree of solvent deuteration and radical properties. Previous studies on ^{13}C have indeed shown that, at magnetic fields between 3-5 T, the DNP performance with degree of solvent deuteration can be predicted from the radical properties, primarily its ESR linewidth, as the sample behavior is well described by the thermodynamic model of thermal mixing. At higher field strengths, on the other hand, a universal sample formulation rationale for optimal DNP has not been found.

The following block of chapters is then dedicated to renal applications of dDNP.

In **Chapter 6** *in vivo* kidney physiology, and in particular renal pH, is investigated in the rat by means of a bolus injection of hyperpolarized L-[1- ^{13}C]alaninamide. pH mapping can indeed be successfully performed using hyperpolarized precursors if they have exchangeable protons with an acid dissociation constant comparable to physiological pH. The applicability of the method was first demonstrated *in vivo* by using hyperpolarized ^{13}C bicarbonate as substrate, and the one other compound that to date has been tested *in vivo* is ^{13}C zymonic acid. Having an amine group that can be protonated at physiological conditions, alaninamide is

a suitable candidate for pH mapping. Furthermore, its selectivity to the enzyme aminopeptidase N opens the potential for the molecule to probe angiogenesis. With many peptides binding to carbon dioxide dissolved in blood, the reactivity of alaninamide with dissolved CO₂ was also investigated.

Chapter 7 shows the potential of using hyperpolarized D-[1-¹³C]alanine as a probe of D-amino acid oxidase activity. This enzyme, that to date can only be probed invasively, has been shown to play a role in NMDA receptor hypo/hyperfunction, and to act as a detoxifying agent in the kidney. Here, the kidney was chosen as the target organ as it is where the enzyme has the highest activity.

In **Chapter 8**, the main results are summarized and future directions are discussed.

Finally, the **Appendix** is dedicated to supplemental data supporting and validating the results presented in the main chapters.

1 Introduction

Sensitivity in NMR

Nuclear magnetic resonance (NMR) is a versatile technique that has proven to be an invaluable analytical chemistry method and an essential diagnostic tool in medicine.

The basic principle of NMR rests on a fundamental property of matter, the nuclear spin quantum number I , that confers nuclei a magnetic moment $\boldsymbol{\mu} = \hbar\gamma_I\mathbf{I}$, γ_I being the nuclear gyromagnetic ratio. In the presence of an external magnetic field \mathbf{B}_0 , the NMR signal is proportional to the net magnetization $\mathbf{M} = \sum_i \boldsymbol{\mu}_i / V = \chi\mathbf{H}$, with V the volume and χ the magnetic susceptibility of the sample. Therefore, properties of the investigated isotope, such as gyromagnetic ratio and abundance, and external parameters like magnetic field strength and temperature will affect the NMR signal intensity.

From a quantum mechanical point of view, in the presence of an external magnetic field \mathbf{B}_0 , the net magnetization is proportional to the difference in population of the Zeeman energy levels of the nuclear spins multiplied by the number of said spins. For a system of spins $I = 1/2$, the population difference between the levels $m_I = \pm 1/2$ is given by the Boltzmann distribution: $\frac{n_-}{n_+} = \exp(-\Delta E/kT) = \exp(-\hbar\gamma_I B_0/kT) = \exp(-\hbar\omega_I/kT)$, with ΔE the energy difference of the two levels and ω_I the nuclear Larmor frequency. This corresponds to a thermal polarization P of:

$$P = \frac{n_+ - n_-}{n_+ + n_-} = \frac{\exp(-\hbar\omega_I/kT) - 1}{\exp(-\hbar\omega_I/kT) + 1} = \tanh\left(\frac{\hbar\omega_I}{2kT}\right) \quad (1.1)$$

If $kT \gg \hbar\omega_I$, which is the case in typical NMR conditions, the polarization becomes linearly dependent on the magnetic field and inversely proportional to temperature. In the case of protons, the stable isotope with the largest gyromagnetic ratio, at 7 T and room temperature

the polarization is 0.0024 %. That of ^{13}C approaches to $6 \cdot 10^{-4}$ % under the same conditions, owing to a 4-fold smaller gyromagnetic ratio.

These low polarization values result in a low sensitivity of the technique, which becomes particularly limiting when probing low-gamma nuclei. *In vivo*, the body's high water content allows for the acquisition of anatomical images with high resolution. Obtaining the metabolic profile of a specific tissue, on the other hand, is more difficult. ^1H magnetic resonance spectroscopy (MRS) provides information on the total metabolites concentration at a given time, but is limited by the low concentration of the metabolites and the low spectral resolution. Owing to the low natural abundance of the ^{13}C isotope (n.a. = 1.1 %), dynamic information can be obtained by detecting the ^{13}C pool after a long infusion of a ^{13}C -enriched precursor. This technique allows to detect the most concentrated metabolites only, and requires long scan times.

To increase the NMR sensitivity, one can resort to hyperpolarization techniques, of which dissolution dynamic nuclear polarization (dDNP)¹ is the most often used for non solid-state applications.

Hyperpolarization techniques

Several techniques have been developed to enhance the signal-to-noise ratio (SNR). The simplest approach is the brute force method,² which consists of placing the sample at temperatures in the mK region and in strong magnetic fields. With this method, achieving for example a ^{13}C polarization level of 50 % requires a magnetic field strength of 16 T and a temperature of 5 mK. While these conditions can be readily met with commercially available equipment, the long nuclear spin-lattice relaxation time $T_{1\rho}$ sets a lower limit to the time needed to reach thermal equilibrium. Spin-exchange optical pumping (SEOP)³ is instead used to hyperpolarize noble gases, the most common being ^{129}Xe . SEOP is a two-steps process based on the transfer of angular momentum from photons to the electrons of an alkali metal vapor. In the presence of an external magnetic field, the electron spins in the conduction band can be fully polarized by shining resonant circularly polarized light on the vapor. In the second step, their polarization is transferred to nuclei of the noble gas *via* Fermi-hyperfine interactions. The polarization transfer process is highly efficient, with final nuclear polarizations up to 95 % in diluted samples. Nuclear spins can also be hyperpolarized through para-hydrogen induced polarization (PHIP).⁴ In this case the high spin order of para-hydrogen is transferred to a third spin by chemical hydrogenation of an unsaturated bond or *via* a transient magnetic interaction mediated by a catalyst. This technique can only be applied to molecules containing unsaturated carbon-carbon bonds, but PHIP methods have been further developed in recent years to extend its applicability to a broader class of molecules.⁵ PHIP only requires simple and cost-effective instrumentation that allows for a fast throughput, as the polariza-

tion process takes only minutes. However, the polarization levels that can be obtained are usually quite low. Despite requiring an expensive experimental setup, dDNP is to date the most versatile hyperpolarization technique and it is the only one thus far translated to the clinic.

Dissolution DNP

DNP relies on the transfer of polarization from electrons to nuclei. As shown in Figure 1.1, owing to a very large gyromagnetic ratio ($\gamma_S \sim 660\gamma_H$, at high magnetic fields and low temperatures the electron polarization approaches 100 %. Under these conditions, the high electronic polarization can be effectively transferred to nearby nuclei by shining microwave radiation at a frequency suitably close to the electrons' resonance frequency, and a non-equilibrium state where the nuclei are hyperpolarized can be obtained.

DNP was theoretically predicted in 1953 by Overhauser.⁶ He realized that, in a metallic sample, because of the hyperfine interaction, transfer of polarization from electrons to nuclei could be induced by shining microwave radiation at the conduction electrons' resonance frequency. In that same year, Slichter and Carver⁷ experimentally confirmed his intuition by measuring at 3 mT a 100-fold enhancement in the ^7Li NMR signal of a metal sample when the conduction electrons were saturated. A few years later, Jeffries,⁸ and shortly afterwards Abragam and Proctor⁹ extended the theory (that was later called solid effect) to non-metals by showing that the same transitions could be induced if the microwave frequency was set to match the condition: $\omega_{\mu w} = \omega_S \pm \omega_I$, ω_I , with ω_S the nuclear and electronic resonance frequencies. In the 1960s and 70s a great interest in the field arose, as DNP started being used to make polarized targets for particle physics experiments. Other regimes that favor electron-nucleus polarization transfer started being investigated, and the cross-effect and thermal mixing¹⁰ models began to be developed. The invention of dissolution DNP¹ in 2003 gave a new boost to the field, and its limits are still being explored.

The basic principle of dissolution DNP rests on the fact that, once a high solid-state polarization level is achieved, if the sample is rapidly dissolved in a hot, pressurized solvent, the hyperpolarized state can be temporarily maintained in liquid-state, leading to signal enhancements greater than 10000 in the case of ^{13}C .¹ The dissolved solution can then be injected into the targeted system, such as an animal/human for an MRI application, a suspension containing an enzyme/cells/proteins to determine enzyme kinetics, interactions with proteins, *etc.* Given the transient nature of the signal, which decays with the characteristic spin-lattice relaxation time constant $T_{1\rho}$ of the nucleus, the measurement time window is restricted to 1-2 minutes. Moreover, the signal detection is further limited by the fact that each excitation entails a non-recoverable signal loss. A selection of *in vivo* applications of dDNP is presented in

the following Section.

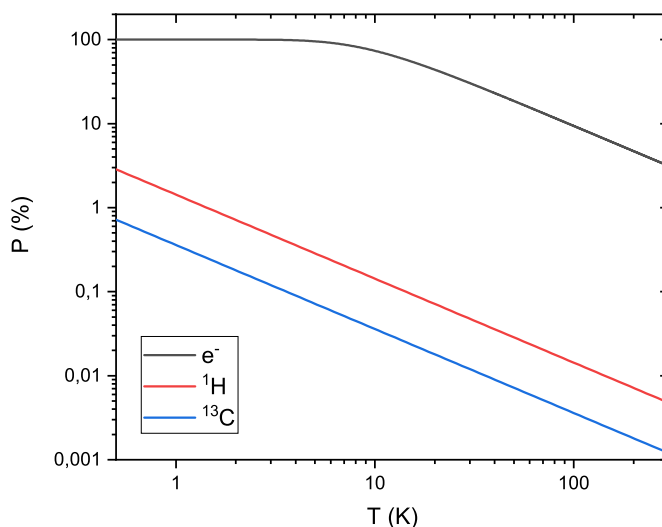


Figure 1.1 – Polarization (in %) of electrons, ^1H and ^{13}C as a function of temperature at 7 T. Both axes are in logarithmic scale.

dDNP *in vivo* applications

Metabolic imaging

DDNP is often used to probe the reaction kinetics of a targeted enzyme. Once injected, if uptake and metabolism of the substrate take place on a time scale comparable to that of the hyperpolarized experiment, its conversion into downstream metabolites can be observed. The ratio of the metabolite's signal intensity to the precursor's will depend on multiple factors including flux, pool sizes and differences in $T_{1\rho}$. Unlike conventional *in vivo* ^{13}C MRS studies, that provide information on the steady-state metabolism, in hyperpolarized studies the transient metabolic state is probed. The two techniques thus provide complementary information.

Because of the high achievable polarization level, long ^{13}C spin-lattice relaxation time and the fact that it is an intermediary in glycolysis, the gold-standard substrate to date for *in vivo* hyperpolarized studies is $[1-^{13}\text{C}]$ pyruvic acid.

Hyperpolarized pyruvate has been widely used to probe the Warburg effect, an increase in aerobic glycolysis favoring lactate production that is characteristic of some types of tumors. The possibility of imaging such metabolic alterations by mapping the lactate-to-pyruvate ratio over the region of interest after the infusion of hyperpolarized pyruvate, thus identifying normal and cancerous tissue, was first demonstrated *in vivo* in rats bearing a P22 tumor by Golman *et al.*¹² This same application constitutes the first dDNP clinical trial.¹³ Prostate can-

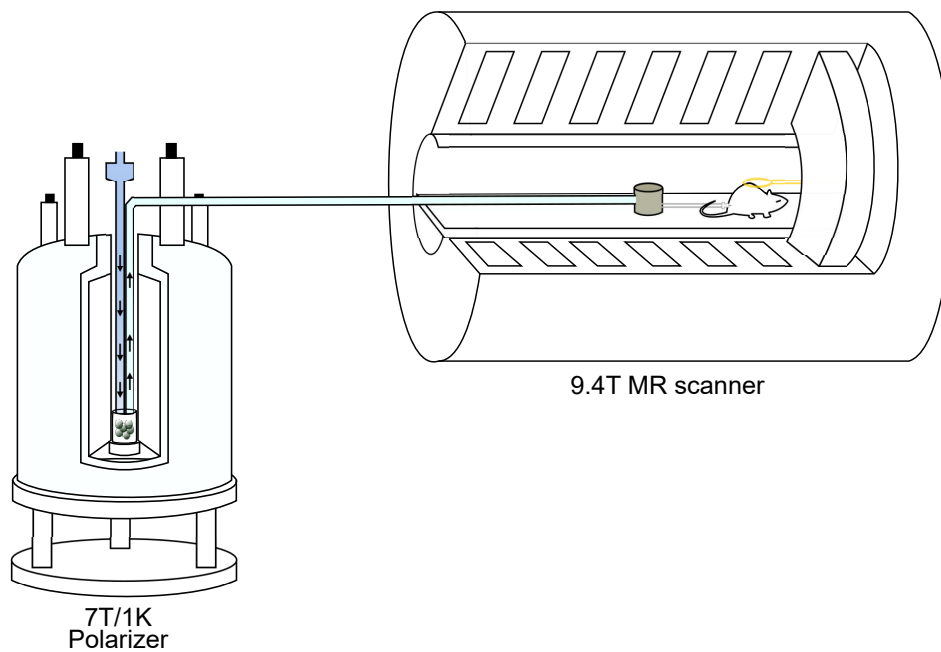


Figure 1.2 – DNP polarizer coupled with a MR animal scanner for *in vivo* preclinical studies. Adapted from: Comment *et al.*¹¹

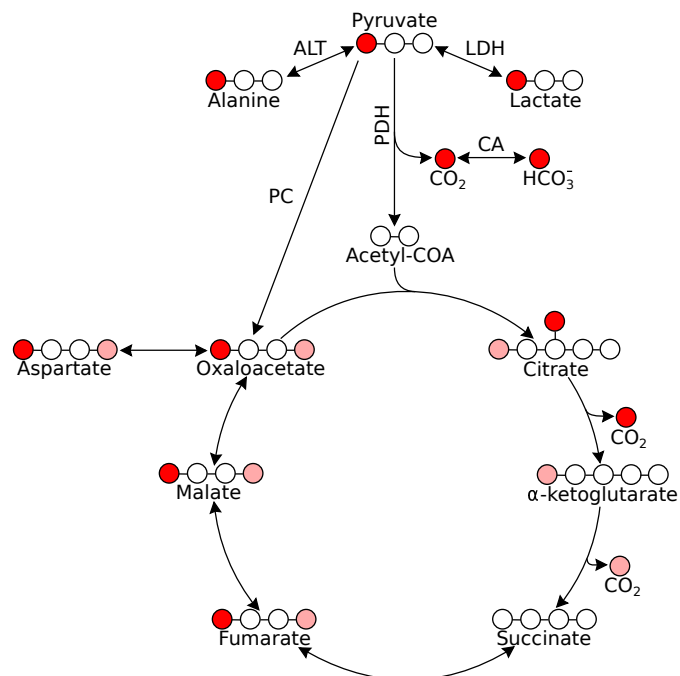


Figure 1.3 – Label transfer from [1-¹³C]pyruvate through the TCA cycle. Red circles represent the ¹³C label.

cer patients were infused a bolus of hyperpolarized pyruvate, and it was demonstrated that the injection of the substrate does not cause adverse episodes. Tumors were identified as those regions with an elevated lactate-to-pyruvate ratio, and in one case a biopsy-proven tumor was identified by hyperpolarized imaging but not by conventional ^1H -MRI. More recently, the rate of pyruvate-to-lactate conversion was proposed as a means to distinguish high-grade from low-grade prostate tumors.¹⁴ Low-grade tumor regions are indeed found to have a conversion rate-constant k_{PL} comparable to that of benign tissues, whereas high-grade regions present a significantly elevated k_{PL} .

[1- ^{13}C]pyruvate can also be used as a metabolic tracer in the heart to obtain information on mitochondrial energy production and to determine cellular damage. The former is acquired by measuring the production of bicarbonate by the mitochondrial pyruvate dehydrogenase (PDH) enzyme, whose expression and activity is closely tied to myocardial substrate selection, while the latter by monitoring alanine production *via* alanine transaminase. The possibility of using hyperpolarized pyruvate to follow cardiovascular disease progression was explored in a model of ischemia and reperfusion¹⁵ and in a dilated cardiomyopathy model of heart failure¹⁶. Experiments on pigs after ischemia¹⁵ revealed a sharp decrease in bicarbonate production starting 15 minutes after occlusion, indicating a diminished flux into the citric acid cycle, while a significant decrease of alanine was observed only 45 minutes after occlusion. A decrease in PDH activity and an early-onset change in Krebs cycle-mediated ^{13}C accumulation in the glutamate pool were on the other hand observed in a dilated cardiomyopathy model of heart failure.¹⁶ ^{13}C images of the human healthy heart have also been acquired, thus demonstrating that cardiac pyruvate metabolism can be probed in humans.

Hyperpolarized pyruvate can also be used to study transport and metabolism in the brain and has the potential to detect neuroinflammation^{17;18;19;20}. The brain inflammatory response indeed entails an increased glycolytic rate, increased pyruvate dehydrogenase kinase (PDK) enzymatic activity and decreased PDH activity, which overall results in an increased lactate-to-pyruvate ratio. However, the main limitations of hyperpolarized pyruvate in the brain are that substrate transport across the blood-brain barrier is rate-limiting,²¹ and anesthesia conditions can strongly influence the apparent metabolic rate²².

Along with pyruvate, many other hyperpolarized precursors have been tested *in vivo*, as Table 1.1 shows. Among them, hyperpolarized [1,4- $^{13}\text{C}_2$]fumarate has proven to be a good substrate to probe early cellular necrosis. Fumarate is a tricarboxylic acid cycle intermediate that is hydrated to produce malate in the reaction catalyzed by fumarase. An increase in malate production was observed in treated lymphoma cells and tumors, which was established to be caused by tumor cell necrosis²⁷. In a rat model of chemically induced acute kidney injury (AKI), instead, an increase in production of malate was detected at an early stage of the disease, before the onset of severe histological changes.²⁸ Other common tracers include [1-

Table 1.1 – Examples of hyperpolarized precursors that have been tested *in vivo*. Adapted from: Ardenkjaer-Larsen.²³

Precursor	Products	Refs.
[1- ¹³ C]pyruvate	[1- ¹³ C]lactate, [1- ¹³ C]alanine, H ¹³ CO ₃ ⁻ , ¹³ CO ₂ , [1,4- ¹³ C]aspartate, [1,4- ¹³ C]malate	12
[2- ¹³ C]pyruvate	[2- ¹³ C]lactate, [2- ¹³ C]alanine, [1- ¹³ C]acetylcarnitine, [5- ¹³ C]citrate, [5- ¹³ C]glutamate	24
[1- ¹³ C]lactate	[1- ¹³ C]pyruvate, [1- ¹³ C]alanine, H ¹³ CO ₃ ⁻ , ¹³ CO ₂	25
NaH ¹³ CO ₃ ⁻	¹³ CO ₂	26
[1,4- ¹³ C ₂]fumarate	[1,4- ¹³ C ₂]malate	27;28
[2- ¹³ C]dehydroxyacetone	[2- ¹³ C]glycerol-3-phosphate, [2- ¹³ C]phosphoenolpyruvate	29
[2- ¹³ C]fructose	[2- ¹³ C]fructose-6-phosphate	30
[5- ¹³ C]glutamine	[5- ¹³ C]glutamate	31
[1- ¹³ C]ethylpyruvate	[1- ¹³ C]lactate, [1- ¹³ C]alanine, H ¹³ CO ₃ ⁻ , ¹³ CO ₂	32
[2,3,4,6,6- ² H ₅ ,3,4- ¹³ C ₂]glucose	[1- ¹³ C]lactate	33
[1- ¹³ C]acetate	[1- ¹³ C]acetyl-carnitine, [5- ¹³ C]citrate	34
[¹³ C]urea	none	35
2-(methyl- <i>d</i> ₃)propan-2- ¹³ C-1,1,1,3,3,3- <i>d</i> ₆ -2-ol	none	36
α-keto-[1- ¹³ C]isocaproate	[1- ¹³ C]leucine	37
[1- ¹³ C]dehydroascorbic acid	[1- ¹³ C]ascorbic acid	38
[1- ¹³ C]alanine	[1- ¹³ C]lactate, [1- ¹³ C]pyruvate, H ¹³ CO ₃ ⁻	39
[1- ¹³ C]glycerate	[1- ¹³ C]pyruvate, [1- ¹³ C]lactate	40
[1- ¹³ C]acetoacetate	[1- ¹³ C]β-hydroxybutyrate, [1- ¹³ C]acetyl-carnitine, [5- ¹³ C]glutamate, [5- ¹³ C]citrate	41
[1- ¹³ C]β-hydroxybutyrate	[1- ¹³ C]acetoacetate, [1- ¹³ C]acetyl-carnitine	41
[1,5- ¹³ C ₂]zymonic acid	none	42
[1- ¹³ C]octanoate	[1- ¹³ C]acetyl-carnitine, [5- ¹³ C]citrate, [5- ¹³ C]glutamate	43
γ-glutamyl-[1- ¹³ C]glycine	[1- ¹³ C]glycine	44

¹³C]alanine for the liver, and [1-¹³C]lactate and [1-¹³C]acetate for the brain. Conversion of hyperpolarized glucose to lactate has been recently observed in tumors⁴⁵ as well as in the healthy brain.³³ The latter, however, requires a specific synthesis and labeling for maximizing the molecule's T₁.

pH mapping

In the body the acid-base balance is tightly controlled through endogenous buffers. Alterations in tissue pH underlie many pathological processes, including ischemia, cancer, inflammation and infection. Therefore, the capability of imaging tissue pH in the clinic could offer new ways of detecting disease and response to treatment.

A number of pH probes belonging to several molecular classes have been studied, but only two substrates were tested *in vivo* and were shown to be effective and non-toxic extracellular pH probes: ¹³C-bicarbonate and [1,5-¹³C₂]zymonic acid (ZA). HCO₃⁻ is the main extracellular buffer that regulates acid-base balance in the blood, and is in rapid exchange with carbon dioxide. Upon injection of hyperpolarized ¹³C-bicarbonate, a mean extracellular pH map can be obtained from the Henderson-Hasselbalch equation by evaluating the ratio between the H¹³CO₃⁻ and ¹³CO₂ spectral peaks, which are separated by ~ 3.5 ppm. This method was first proposed by Gallagher *et al.*²⁶ and its main limitations are sample preparation, as sodium bicarbonate is not readily soluble and highly concentrated samples are difficult to obtain, and a relatively short *in vivo* ¹³C spin-lattice relaxation time constant. ¹³C-labeled carbonated precursors of bicarbonate like glycerol carbonate⁴⁶ and ethyl acetate carbonate⁴⁷ have also

been proposed as pH probes, the underlying principle being that ^{13}C -bicarbonate is readily produced from these precursors either in a rapid basic hydrolysis post-dissolution (as is the case for glycerol carbonate) or in an esterase-catalyzed reaction upon injection *in vivo* (as for ethyl acetate carbonate).

[1,5- $^{13}\text{C}_2$]zymonic acid,⁴² on the other hand, is a degradation product of [1- ^{13}C]pyruvic acid. pH sensitivity of the carbons-13 at the 1- and 5- positions arises from the exchange of the enolic hydroxyl proton. Here, only one resonance per label is observed at a given pH. From the chemical shift of the spectral peaks, one can then directly determine the tissue pH. Like bicarbonate, ZA reportedly probes extracellular tissue pH. The main limitations in the use of this probe lie in its short polarization lifetime and in the fact that, since two carbon positions are labeled, spectral overlap renders quantification difficult. An increase in the $^{13}\text{C}1$, $^{13}\text{C}5$ spin-lattice relaxation times of approximately 15 % and 40 %, respectively, was reported by perdeuterating the molecule.⁴⁸

Intracellular pH can be measured *in vivo* by injecting hyperpolarized [1- ^{13}C]pyruvate: since the produced bicarbonate will mostly have an intracellular origin (at least at the beginning of the experiment), one can calculate a mean pH value using the same ratiometric approach that was proposed by Gallagher *et al.*²⁶ In this case, however, low SNR may be an issue given the low amplitude of the bicarbonate spectral peak, so this approach will work better for tissues having a high PDH activity. Schroeder *et al.*⁴⁹ found a good correlation between the intracellular pH measured with this method and the pH obtained with ^{31}P MRS in perfused hearts.

Perfusion agents

Hyperpolarized molecular probes can be also used to monitor tissue perfusion. Several substrates that have been proposed as perfusion agents. Among them, perdeuterated ^{13}C labeled 2-methylpropan-2-ol has been shown to freely diffuse in the brain and to have a long residence time in the tissue;³⁶ continuous imaging (for tens of seconds) of the agent is thus possible. Blood flow measurements in preclinical cancer models were similarly performed using hyperpolarized ^{13}C urea.³⁵ Different signal patterns were observed between normal and cancerous murine hepatic tissues, with a significant reduction in mean blood flow and an increase in rim detected in tumors. Hyperpolarized water^{50;51} has also been proposed as an angiography/perfusion contrast agent, the main advantage resting on the much higher signal intensity of the probe and the biggest limitation being the short ^1H spin-lattice relaxation time.

Conclusions

dDNP offers a powerful solution to the sensitivity problem intrinsic to NMR of low-gamma nuclei. The technique has been employed in a wide variety of studies targeting a number of metabolic pathways and physiological parameters. Many of these studies have been using hyperpolarized pyruvate given its favorable physical and biochemical properties, namely its long spin-lattice relaxation time and its role in glycolysis. The field however remains open as the search for the “killer” biomarker/application continues.

2 DNP mechanisms

Spin Hamiltonian

The mechanism of polarization transfer is theoretically described starting from the spin Hamiltonian:

$$\begin{aligned}\mathcal{H} &= \mathcal{H}_{ZI} + \mathcal{H}_{ZS} + \mathcal{H}_{SI} + \mathcal{H}_{II} + \mathcal{H}_{SS} + \mathcal{H}_{\mu w} \\ &= -\hbar\gamma_S \mathbf{S} \cdot \mathbf{B}_0 - \hbar\gamma_I \mathbf{I} \cdot \mathbf{B}_0 + \mathbf{S} \cdot \mathbf{A} \cdot \mathbf{I} + \mathbf{I} \cdot \mathbf{C} \cdot \mathbf{I} + \mathbf{S} \cdot \mathbf{D} \cdot \mathbf{S} - \hbar\gamma_S \mathbf{S} \cdot \mathbf{B}_1 \cos(\omega_{\mu w} t)\end{aligned}\tag{2.1}$$

where \mathcal{H}_{ZI} , \mathcal{H}_{ZS} are the nuclear and electronic Zeeman interactions, respectively, \mathcal{H}_{SI} is the hyperfine interaction between nuclei and electrons, \mathcal{H}_{II} , \mathcal{H}_{SS} are the nuclear and electronic dipolar interactions, and $\mathcal{H}_{\mu w}$ is the interaction of the microwave field with the electrons. The second line of Eq. 2.1 was derived for a system composed of one electron and one nucleus only, but its extension to the case of N_S electrons and N_I nuclei is straightforward. Moreover, it is assumed that $\gamma_S < 0$ and $\gamma_I > 0$.

Under dDNP conditions, three different mechanisms can drive the transfer of polarization from electrons to nuclei: solid effect (SE), cross effect (CE) and thermal mixing (TM). Which among the three predominates will depend on the properties of the radical and on the investigated nuclear pool.

Solid effect

When the electron spin resonance (ESR) linewidth $\Delta\omega_S$ is narrower than or comparable to the nuclear Larmor frequency ω_I , DNP takes place *via* the solid effect. This mechanism is a one-step process: the microwave field, at a frequency matching $\omega_S \pm \omega_I$, causes an electron spin to flip down to its ground state and a nuclear spin to change its own orientation. This

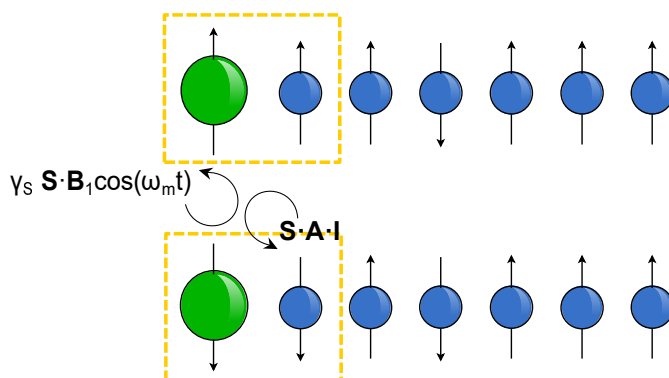


Figure 2.1 – Fundamental step of DNP *via* solid effect: the combined effect of the hyperfine coupling and the microwave field induces the simultaneous flip of one electron and one nucleus.

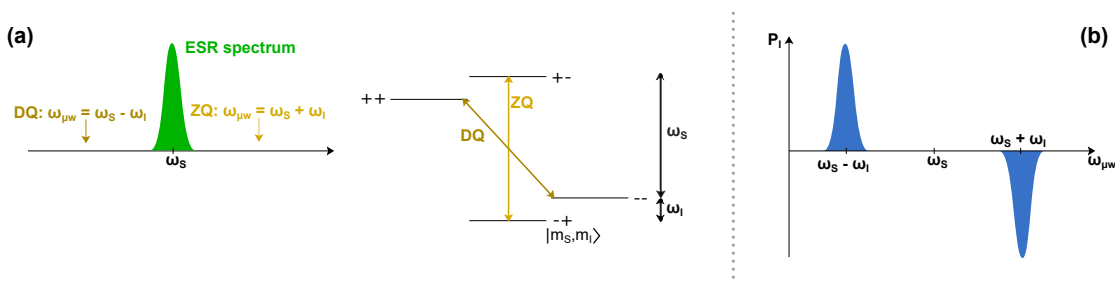


Figure 2.2 – Fundamental transitions of solid effect. (a) Zero-quantum and double-quantum transitions can be induced between the mixed electronic and nuclear states by shining microwave radiation at the frequency $\omega_S \mp \omega_I$, respectively. (b) Characteristic microwave frequency sweep profile of solid effect. Two lobes corresponding to positive and negative enhancement are observed at a frequency distance of $\mp \omega_I$ from ω_S .

transition is made possible by the presence of the hyperfine coupling between electrons and nuclei that generates a mixing of the energy levels. A schematic of the process can be found in Figure 2.1.

Since the hyperfine interaction can be considered to have a purely dipolar nature, the polarization transfer process only involves nuclei that are sufficiently close in space to the radicals. The nuclear polarization is then transferred to the bulk nuclei *via* spin diffusion, and the electron involved in the process relaxes back to its equilibrium configuration.

The fundamental transition of solid effect

A rate equation for the evolution of the nuclear spin polarization under DNP *via* solid effect can be readily derived for a system composed of one electron and one nucleus using an alternative scrambled-states approach. This approach relies on the assumption that the

microwave power $\omega_{1S} = -\gamma_S B_1$ is much lower than the nuclear Larmor frequency ω_I . If this hypothesis holds true, the spin Hamiltonian describing the system:

$$\mathcal{H} = \hbar \left[\omega_S S_z + 2\omega_{1S} S_x \cos(\omega_{\mu w} t) - \omega_I I_z + \frac{1}{2} S_z (A_{z-} I_+ - A_{z+} I_-) \right] \quad (2.2)$$

can be diagonalized by transforming it into a reference frame rotating about \mathbf{B}_0 with $\omega_{\mu w}$ (*rotating frame*), and subsequently into a second reference frame (*tilted rotating frame*) that rotates with the effective frequency ω_{eff} of the electron in the former frame. Energy conservation arguments then allow the new system Hamiltonian to be truncated so that, when transformed back to the rotating frame, it is reduced to:

$$\mathcal{H} = \hbar \left[(\omega_S - \omega_{\mu w}) S_z - \omega_I I_z + \frac{1}{2} \omega_{1S} (S_+ + S_-) - \frac{1}{8} (S_+ + S_-) (A_{z-} I_+ - A_{z+} I_-) \frac{\omega_{1S}}{\omega_I} - \frac{1}{8} (S_+ - S_-) (A_{z-} I_+ + A_{z+} I_-) \frac{\omega_{1S}}{\omega_I} \right] \quad (2.3)$$

where S_{\pm} are the step operators for the electron's energy levels. In Eq. 2.3, the non-diagonal term $\omega_S(S_+ + S_-)$ induces transitions between levels: $|m_S\rangle = |+\rangle \leftrightarrow |-\rangle$. Because of energy conservation, these transitions require the microwave frequency to match exactly ω_S . The other two non-diagonal terms, on the other hand, induce the double quantum (DQ) and zero-quantum (ZQ) transitions between: $|m_S, m_I\rangle = |++\rangle \leftrightarrow |--\rangle$ and $|m_S, m_I\rangle = |+-\rangle \leftrightarrow |-+\rangle$. These transitions require $\omega_{\mu w} = \omega_S - \omega_I$ and $\omega_{\mu w} = \omega_S + \omega_I$, respectively. Given that the microwave frequency cannot take up simultaneously the values ω_S , $\omega_S - \omega_I$ and $\omega_S + \omega_I$ three separate cases can be distinguished:

- $\omega_{\mu w} = \omega_S$: pure electron resonance. The microwave field is saturating the electron spins and no polarization transfer occurs.
- $\omega_{\mu w} = \omega_S - \omega_I$: the terms proportional to $S_+ I_+$ and $S_- I_-$ induce transitions involving both electron and nuclear spins, and polarization transfer can take place. The Hamiltonian describing the system is reduced to:

$$\mathcal{H}_A = \hbar \left[(\omega_S - \omega_{\mu w}) S_z - \omega_I I_z - \frac{1}{4} (A_{z-} S_+ I_+ - A_{z+} S_- I_-) \frac{\omega_{1S}}{\omega_I} \right].$$

- $\omega_{\mu w} = \omega_S + \omega_I$: similarly to the previous case, transitions simultaneously involving electron and nucleus are induced. The system Hamiltonian now reads:

$$\mathcal{H}_B = \hbar \left[(\omega_S - \omega_{\mu w}) S_z - \omega_I I_z - \frac{1}{4} (A_{z+} S_- I_+ - A_{z-} S_+ I_-) \frac{\omega_{1S}}{\omega_I} \right].$$

As in \mathcal{H}_A , \mathcal{H}_B the non-diagonal term is much smaller than the diagonal one, the two Hamiltonians can be solved on the eigenstates basis $|m_S, m_I\rangle$ using perturbation theory. The fol-

lowing rate-equation for the nuclear polarization can thus be derived:

$$\frac{\partial P_I}{\partial t} = -W_h^+(P_I - P_S) - W_h^-(P_I + P_S) \quad (2.4)$$

P_I, P_S being the electron and nucleus polarization and W_h^\pm the electron-nucleus flip-flip transition rate defined as

$$W_h^\pm = \frac{1}{2}\pi \frac{\left|\frac{A_{z+}}{2}\right|^2 \omega_{1S}^2}{\omega_I^2} h(\omega_S - \omega_{\mu w} \mp \omega_I)$$

where $h(\omega_S - \omega_{\mu w} \mp \omega_I)$ is the homogeneous lineshape of the radical (i.e. the spectral density of the fluctuations) at $\omega_S - \omega_{\mu w} \mp \omega_I$.

As Eq. 2.4 holds for a system composed of one electron and one nucleus only, it should be extended to the case of N_I nuclei and N_S electrons and to account for nuclear relaxation. For such a system, the equation describing the growth of nuclear polarization reads:

$$\begin{aligned} \frac{\partial P_I}{\partial t} = & -2 \frac{N_S A^2}{N_I \omega_I^2} \left[W_g^0(\omega_{\mu w} + \omega_I) [P_I - P_S(\omega_{\mu w} + \omega_I)] \right. \\ & \left. + W_g^0(\omega_{\mu w} - \omega_I) [P_I + P_S(\omega_{\mu w} - \omega_I)] + \frac{1}{T_{1S}} (1 - P_L P_S) P_I \right] \end{aligned} \quad (2.5)$$

where:

$$W_g^0(\omega) = \frac{1}{2}\pi \omega_{1S}^2 g(\omega)$$

is the rate of allowed ESR transitions where only electron spins flip, P_L the thermal polarization of the electron spins, $g(\omega)$ the electron ESR line, $A^2 = \frac{2\pi}{5} \frac{n_I}{r_b^3} \left(\frac{\mu_0}{4\pi} \hbar \gamma_I \gamma_S \right)^2$ the average hyperfine interaction, n_I the density of nuclear spins, and r_b the minimal distance between a bulk nucleus and an electron. Here, $g(\omega)$ is non-zero only when $\omega = \omega_S$. Two cases can then be distinguished.

- If the ESR line is narrower than ω_I , at a given microwave frequency $\omega_{\mu w}$ the matching condition $\omega_{\mu w} = \omega_S \pm \omega_I$ will never hold for the + and - sign simultaneously, so either positive or negative polarization will be transferred (*well-resolved* solid effect). The DNP enhancement profile as a function of the microwave frequency will then present a positive and a negative lobe separated by $2\omega_I$ (Figure 2.2).
- If the ESR line is comparable to ω_I , at a given $\omega_{\mu w}$ there might be electron spin packets satisfying both conditions $\omega_{\mu w} = \omega_S \pm \omega_I$. Positive and negative polarization can be

2.3. DNP *via* triple spin flips: thermal mixing and cross effect

transferred simultaneously, and the net nuclear polarization will be given by the difference between the two. In this case the process is called *differential* solid effect.

The maximum nuclear spin polarization P_I^∞ can be calculated from Eq. 2.5 by setting $\partial P_I / \partial t = 0$. Assuming only $W_g^0(\omega_{\mu w} + \omega_I) \neq 0$ this yields:

$$P_I^\infty = \frac{W_g^0(\omega_{\mu w} + \omega_I) T_{1S}}{W_g^0(\omega_{\mu w} + \omega_I) T_{1S} + (1 - P_L^2)} P_L \quad (2.6)$$

This equation shows that the maximum achievable nuclear polarization is independent of the interaction between electrons and nuclei and of the concentration of electrons spins. What determines P_I^∞ are instead the rate of allowed ESR transitions, and hence the microwave power, and the electron spin-lattice relaxation time T_{1S} . Only in the limit of strong saturation, i.e. $W_g^0(\omega_{\mu w} + \omega_I) T_{1S} \gg (1 - P_L^2)$ is the maximum nuclear polarization $P_I^\infty = P_L$.

As discussed above, to observe experimentally the well-resolved solid effect in dDNP conditions the ESR line of the polarizing agent needs to be narrower than ω_I . For this condition to hold, especially at high magnetic fields, the radical **g**-anisotropy needs to be sufficiently small. Trityls were found to fulfill this condition when used to polarize protons,⁵² whereas most radicals have an **g**-anisotropy that is too large to observe SE on low-gamma nuclei.

DNP *via* triple spin flips: thermal mixing and cross effect

If the ESR linewidth is broader than the nuclear resonance frequency ($\Delta\omega_S > \omega_I$), the DNP process is driven by either thermal mixing or cross effect, or by a combination of the two.

The fundamental mechanisms at the base of DNP *via* TM and CE are triple-spin flips. Here, the microwave field saturates the electron spins having $\omega_S = \omega_{\mu w}$, and this depolarization is propagated across the ESR spectrum by energy-conserving flip-flops promoted by the mutual electronic dipolar interaction. Polarization transfer then results from the combined effect of the mutual electronic and hyperfine interactions which induce triple-spin flips involving two electrons and a nucleus. As a consequence, the three spins change their relative orientation. Similarly to SE, the nuclear polarization is then spread to the bulk by means of nuclear spin diffusion. The nuclei get thus polarized. A schematic depiction of this process is shown in Figure 2.3. For DNP *via* triple-spin flips to be efficient, spectral diffusion has to be fast compared to electronic relaxation, so that a significant number of electrons can participate in the polarization transfer. Because they do not involve second-order transitions, CE and TM are usually much more efficient DNP processes than SE.

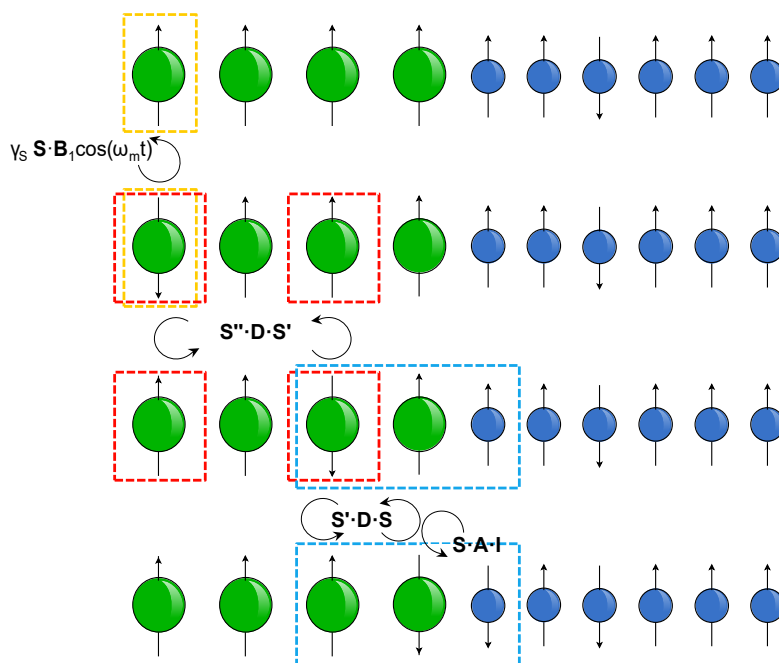


Figure 2.3 – DNP process *via* thermal mixing: (yellow boxes) the microwave field induces the spin flip of an electron, which is in turn propagated through the line by spectral diffusion (red boxes). A triple-spin flip between two electrons and a nucleus generates the polarization transfer to the nucleus (blue boxes).

Motivated by the need for optimized dDNP conditions and sample preparations, a substantial effort has been made in the last decades to achieve a full theoretical understanding of the physical phenomena and circumstances that promote cross effect over thermal mixing and *vice versa*.^{53;54;55;56;57;58;59} Recently, Wenckebach provided a unified model of DNP where he demonstrated that the difference between CE and TM originates in the reservoir that provides/absorbs the energy necessary for triple-spin flips to occur.^{60;61} More specifically, he defined cross effect as the mechanism that takes place when the electron dipolar interaction is weak compared to ω_I , so that the energy required for the triple spin flips is provided by the difference in Zeeman frequencies of the two electron spins resulting from a large **g**-anisotropy or anisotropic Zeeman interactions. In thermal mixing, on the other hand, the energy necessary for the triple-spin flips transitions is provided by the dipolar coupling field experienced by the two electrons. Therefore, TM requires a strongly coupled electronic system. Practically, to determine whether one mechanism is dominant over the other, it is useful to define a cutoff frequency Δ_0 representing the maximum dipolar coupling between an electron pair. Then, it is possible to demonstrate that only if Δ_0 is greater than ω_I is thermal mixing predominant over cross effect. The mathematical formalism behind this model is fairly complex and will not be discussed here. Further details and experimental evidence in support of this model will be provided in Chapter 4. A simplified thermodynamic model of thermal mixing,

that still allows the estimation of the maximum nuclear enhancement and provides information on how the physical properties of the sample affect the process, is instead presented in the following section.

Thermodynamic model of thermal mixing

A thermodynamic model of thermal mixing can be built starting from spin temperature theory.⁶² Provotorov was the first to demonstrate that, in the limit of fast spectral diffusion and high temperature, a spin temperature T_{SS} different from the electron Zeeman spin temperature T_S can be attributed to the electron non-Zeeman reservoir identifiable with \mathcal{H}_{SS} .⁶³ Qualitatively, this can be justified by the fact that, if the electronic polarization is not equal to ± 1 , multiple spin configurations that give rise to the same Zeeman energy but different $\langle \mathcal{H}_{SS} \rangle$ can be found. Then, by shining microwave radiation at a frequency $\omega_{\mu w} = \omega_S \pm \Delta$, it is possible to show that if $\hbar\Delta \simeq \langle \mathcal{H}_{SS} \rangle$ exchange of energy quanta between the electron Zeeman and the electron non-Zeeman reservoirs takes place. As a result, the electron Zeeman system is heated, and correspondingly the electron non-Zeeman reservoir is cooled down, its spin temperature being allowed to take either positive or negative values depending on the sign of $\omega_{\mu w} - \omega_S$. We talk of cooling independently of the sign of T_{SS} because the electron non-Zeeman spin temperature is found to be much lower than the lattice temperature.

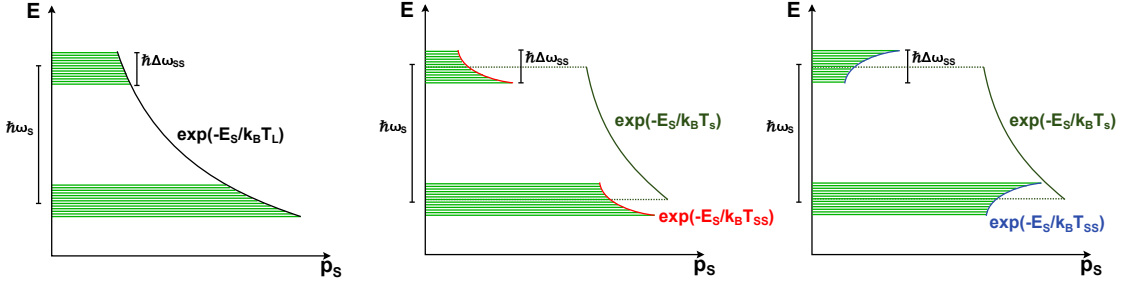


Figure 2.4 – Electron spin population distribution p_S (a) at thermal equilibrium ($T_S = T_L$); (b) under microwave irradiation at a frequency $\omega_{\mu w} < \Delta\omega_{SS}$ ($T_{SS} > 0$); (c) under microwave irradiation at a frequency $\omega_{\mu w} > \Delta\omega_{SS}$ ($T_{SS} < 0$).

In a second step, thermal contact is established between the electron non-Zeeman and the nuclear Zeeman systems through the hyperfine interaction \mathcal{H}_{SI} , so that at steady-state their spin temperatures are equalized. In the limit of fast cross-relaxation (i.e. perfect thermal contact between the electron non-Zeeman and the nuclear Zeeman reservoirs), the inverse temperature of the nuclear Zeeman pool is uniform across the sample and is equal to that of the electron non-Zeeman reservoir at all times. The energy flow between reservoirs is depicted in Figure 2.5.↓

Rate equations can be derived to describe the evolution of the inverse spin temperatures of

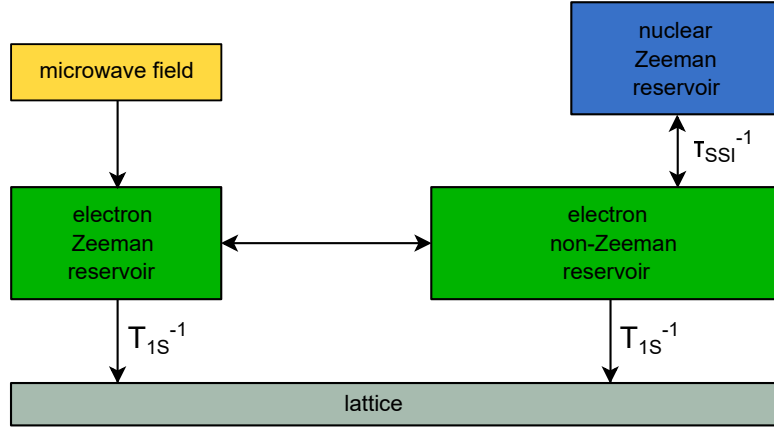


Figure 2.5 – Energy flow between reservoirs.

the electronic and nuclear reservoirs ($\alpha = \hbar/kT_S$, $\beta_{NZ} = \hbar/kT_{SS}$ and $\beta_I = \hbar/kT_I$, respectively) in a reference frame rotating about \mathbf{B}_0 with $\omega_{\mu w}$ by combining the rate equation of triple spin flips with Provotorov's equations describing the dynamics of the electronic system under microwave radiation. One finds:

$$\begin{aligned} \omega_S \frac{\partial \alpha}{\partial t} &= -2W_g(\omega_{\mu w}) [\omega_S \alpha + (\omega_{\mu w} - \omega_S) \beta_{NZ}] - \omega_S \frac{1}{T_{1S}} [\alpha - \beta_L] \\ D^2 \frac{\partial \beta_{NZ}}{\partial t} &= -2W_g(\omega_{\mu w}) (\omega_S - \omega_{\mu w}) [\omega_S \alpha + (\omega_{\mu w} - \omega_S) \beta_{NZ}] + D^2 \left(\frac{1}{\tau_{1SS}} [\beta_I - \beta_{NZ}] - \frac{1}{T_{1S}} \beta_{NZ} \right) \\ \frac{\partial \beta_I}{\partial t} &= -\frac{1}{\tau_{SSI}} \frac{N_S D^2}{N_I \omega_I^2} [\beta_I - \beta_{NZ}] \end{aligned} \quad (2.7)$$

Here, $W_g(\omega) = \frac{1}{2} \pi \omega_{1S}^2 g(\omega)$ is the rate of transitions induced by the microwave field, $g(\omega)$ the full ESR lineshape, D^2 the dipolar energy in frequency units and τ_{SSI}^{-1} the triple spin flip rate defined as:

$$\frac{1}{\tau_{SSI}} = \frac{1}{2} \pi \frac{A^2 M_2^0}{D^2} \int_{-\infty}^{\infty} d\omega_S g(\omega_S) g(\omega_S - \omega_I) \quad (2.8)$$

At steady state, a solution of such equations is:

$$\frac{\beta_{\infty}}{\beta_L} = -\frac{2W_g(\omega_{\mu w}) T_{1S} \omega_S (\omega_{\mu w} - \omega_S)}{2W_g(\omega_{\mu w}) T_{1S} [(\omega_{\mu w} - \omega_S)^2 + D^2] + D^2} \quad (2.9)$$

This shows that the maximum enhancement depends on the microwave transition rate, the

2.3. DNP *via* triple spin flips: thermal mixing and cross effect

electronic spin-lattice relaxation time and the electronic dipolar coupling, but not on the triple-spin flip rate. In the limit of strong saturation, Eq. 2.9 becomes:

$$\frac{\beta_{\infty}}{\beta_L} = \frac{\omega_S (\omega_{\mu w} - \omega_S)}{(\omega_{\mu w} - \omega_S)^2 + D^2} \quad (2.10)$$

If several nuclear species a, b, \dots are present in the sample, it is possible to demonstrate that, because of their thermal coupling with the electron non-Zeeman reservoir, they will all reach the same spin temperature. In this case the efficiency of the DNP process is strictly related to the heat capacity of the nuclear Zeeman reservoirs, defined as:

$$C = \frac{\partial \langle \mathcal{H}_{ZI} \rangle}{\partial T} = \frac{\hbar}{2} [N_{Ia} \omega_{Ia}^2 + N_{Ib} \omega_{Ib}^2 + \dots] \quad (2.11)$$

One should bear in mind that these equations were derived in the high temperature approximation, a limit that is not satisfied under typical dDNP conditions. A simplified model describing the low temperature case was initially presented by Borghini,⁶⁴ and only recently a formal extension of the Provotorov equations was developed by Wenckebach.^{57;56} Moreover, the results presented here do not account for leakage, i.e. sources of nuclear relaxation different from the interactions (both *direct* and *indirect*) with the radical, that has the net effect of decreasing the achievable nuclear enhancement.

Early experimental evidence of the existence of a coupling between the electron dipolar and the nuclear Zeeman reservoirs was provided by Wenckebach *et al.*⁶⁵ They showed that, in a crystal sample of $\text{La}_2\text{Mg}_3(\text{NO}_3)_{12} \cdot 24 \text{ H}_2\text{O}$ doped with N_p centers, the decay constant of the hyperpolarized proton signal matched the relaxation time of the asymmetry in the EPR line generated by microwave saturation, indicating a contact between the two systems. Further experimental proof was collected by Cox *et al.*⁶⁶ in a LiF crystal doped with F-centers. By simultaneously monitoring the ^7Li and ^{19}F signal evolution after hyperpolarization they were able to show that upon RF saturation of one of the two nuclear species, the two systems would evolve together until an identical spin temperature was reached, and only then relaxed back to equilibrium. The coupling between the nuclear reservoirs was adduced to their separate contact with the dipolar electronic reservoir. This same experiment was proposed as a way to determine whether TM is the predominant mechanism in systems employing nitroxide radicals.⁵⁴

More recently, evidence of good thermal contact between the electron non-Zeeman and the nuclear Zeeman reservoirs was reported also in the case of amorphous solids at magnetic field strengths $B_0 \leq 5 \text{ T}$. Kurdzesau *et al.*⁶⁷ systematically studied the DNP properties of a series of labeled compounds dissolved in water-alcohol mixtures and found at steady-state the

different nuclear Zeeman pools had equal spin temperatures. At higher magnetic fields, however, the situation was observed to become more complicated, as spectral diffusion slows down and experimental results can no longer be explained using the traditional thermal mixing formalism.⁶⁸

Conclusions

The three mechanisms that give rise to polarization transfer in dDNP conditions are solid effect, cross effect and thermal mixing. The theoretical background of SE has been widely studied and is well understood; the same, however, cannot be said for CE and TM, which happen to be the most efficient mechanisms under these conditions. A number of efforts have been made in the recent years to model and explain how the chemico-physical properties of the sample influenced the DNP process. Despite the many advances, a model that perfectly reproduces experimental results has yet to be found. The present chapter focused on illustrating the polarization transfer mechanisms alone, but the concomitant processes, including spectral and spin diffusion, as well as spin relaxation, that contribute to DNP and contribute determining its efficiency, were not described.

3 dDNP: practical considerations

System requirements

DNP polarizer

As illustrated in Chapters 1 and 2, in dDNP, high magnetic fields and low temperatures are needed to obtain a high electronic polarization, while microwave radiation is required to induce polarization transfer to nuclei.

Superconducting magnets are used to generate the magnetic field \mathbf{B}_0 . Typical field strengths range between 3.35 T and 7 T. Performing DNP at even higher fields was shown not to be advantageous,⁶⁹ as the increase in the relaxation time constants it entails causes a lengthening of the polarization buildup dynamics so significant that higher radical concentrations are required to obtain polarization levels comparable to those at lower field. The constraints on magnetic field homogeneity are generally lower than for high-resolution NMR owing to the broad low-temperature NMR lines (FWHM \sim few kHz): $\Delta B_0 / B_0 < 25$ ppm usually suffices.

The temperature in the sample space can be lowered to 4.2 K by supplying liquid helium to it. In open systems, this is done either by using a continuous-flow cryostat connected to an external helium storage dewar^{70;71} or by coupling the Variable Temperature Insert (VTI) hosting the sample to the helium can of the magnet through a needle valve.¹ Temperatures around 1 K can then be reached by mechanically pumping on the sample space (200-500 m³/h), the helium gas then being vented to atmosphere. Such setups have a high liquid helium consumption (approximately 2 L per sample), and are therefore quite costly. Cryogen-free systems offer the advantage that the cryogen is not lost in the operation. Most of these systems^{69;72;73} rely on a closed circuit where a compressor and a cold-head provide the cooling power and condense helium gas into a helium pot, in turn connected to the VTI through a needle valve. The sample space temperature is maintained using a dry pump, and the recovered helium

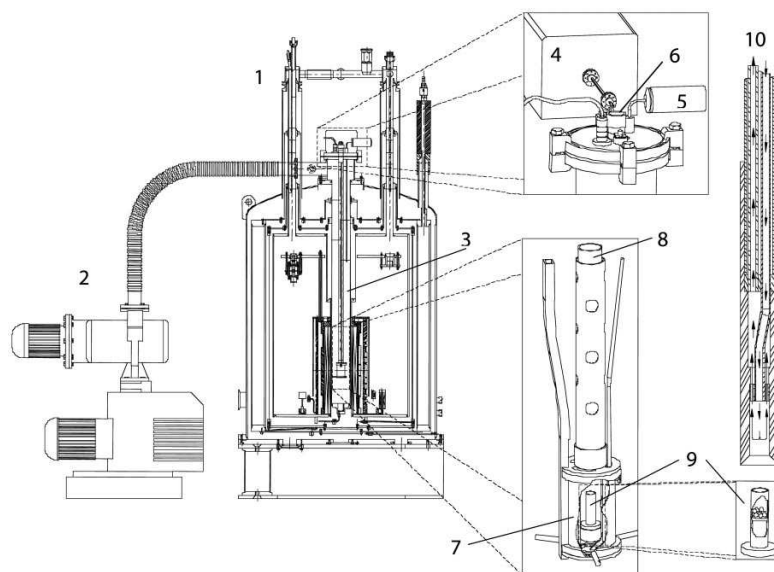


Figure 3.1 – Schematic drawing of the first d-DNP polarizer:¹ 1, DNP polarizer; 2, vacuum pump; 3, VTI; 4, microwave source; 5, pressure transducer; 6, sample port; 7, microwave container; 8, sample holder; 9, sample container; 10, dissolution wand. ©National Academy of Sciences, 2003.

gas is purified and sent back to be re-liquefied. A cryogen-free multi-sample system based on a commercial dilution refrigerator with a 1 K-stage was recently proposed.⁷⁴ Thanks to its stability, the setup does not require the use of a needle-valve to regulate the influx of helium in the sample space. As a result the system is more robust, but at the same time requires a complete warmup in case of a spill during dissolution.

The systems described above have all been intended for research purposes, so concerns like sterility and quality control of the sample were not taken into account in the designs. The SpinLab polarizer was on the other hand commercially developed for clinical use.^{75;76} This cryogen-free system operates at a magnetic field of 5 T and is equipped with a cryocooler and a sorption pump to keep the sample space temperature at 0.8 K. A sterile fluid path (SFP) made of polyether ether ketone or polysulfone can be integrated in the setup. The SFP, which is provided with a vial holding up to 2 mL of sample, is designed to prevent any contamination of the sample by the contact with superfluid helium, and allows for radical filtration, and pH, temperature and precursor concentration quality control measurements after dissolution.

Commercially-available sources tuned to the electrons' resonance frequency are employed to generate the microwave field. At the low temperatures required for dDNP, because of the slow electronic relaxation ($T_{1S} \approx 0.1\text{-}1\text{ s}$), output power levels in the range 0-100 mW are generally sufficient to have saturation of the ESR line. The microwave radiation is then delivered to

the sample space by means of a waveguide. Modulation of the microwave frequency/power can also be implemented. This was observed to be beneficial when spectral diffusion across the ESR line is not fast compared to the electron spin-lattice relaxation time, as it allows the saturation of a greater number of electron spin-packets.^{77;78;79}

LOD-ESR

The DNP polarizer can be easily coupled to a longitudinally-detected (LOD)-ESR system to probe the electron dynamics,^{80;81} the advantage in developing such a setup mostly lying in its cost-effectiveness. The basic principle of LOD-ESR is to induce a periodic change in the electronic magnetization by modulating the microwave power with a square-wave function. This change in magnetization can then be detected using a pickup coil aligned parallel to the \mathbf{B}_0 field. Pump-probe experiments can be performed with an LOD-ESR setup. The electron spin-lattice relaxation time T_{1S} can be measured by monitoring the full evolution of the signal induced by the microwave power oscillating at a modulation frequency $\nu_M \ll T_{1S}^{-1}$, or by means of saturation-recovery experiments. The ESR spectrum can be obtained by incrementally changing the modulation frequency and recording the mean induced voltage as a function of the microwave frequency. Finally, if two microwave sources are available, electron double-resonance (ELDOR) experiments⁸² can be performed to determine how spectral diffusion influences the spin dynamics.

Sample composition

The choice of the substrate to be used in *in vivo* studies is limited by two factors: the liquid-state spin-lattice relaxation time T_{1I} of the nucleus of interest should be on the order of tens of seconds, and the metabolism to be probed should take place on a timescale comparable to the duration of the experiment. Furthermore, *in vivo* applications require a post-dissolution substrate concentration between 10 and 150 mM; therefore, frozen samples have to be fairly concentrated. Several expedients can be undertaken if the substrate has a low solubility. In the case of salts, substrate solubility may be increased by changing the counter ion. For amino acids, instead, high or low pH preparations are found to increase solubility.

Along with the substrate, the most important ingredient in the DNP sample is the polarizing agent. Radicals used in dDNP need to be chemically stable, have low toxicity, and readily dissolve in the sample matrix. Generally, a radical concentration ranging between 15-60 mM is required to have efficient DNP. The most widely used polarizing agents are nitroxides, trityls and BDPA organic radicals. Trityls and BDPA, owing to their narrow ESR linewidth, usually perform well with low- γ nuclei. In particular, with trityl OX063 and AH111501 polarization levels as high as 70% in the case of $[1-^{13}\text{C}]$ pyruvic acid at 7 T were measured.⁸³

Trityl AH111501 is also routinely used in clinical studies with pyruvic acid as, because of its hydrophobicity, it has a low water solubility at low pH and is thus easily filtered after sample dissolution. BDPA was shown to lead to enhancements comparable to those of trityls on ^{13}C -labeled molecules.⁸⁴ However, the radical is not water-soluble, and sample formulation requires the addition of organic solvents like sulfolane or polyethylene glycol. Nitroxide radicals like TEMPOL provide a cheaper alternative to trityls: thanks to their broad linewidth, they work well to polarize protons, while on low-gamma nuclei they are generally not as efficient. Nitroxides can be scavenged upon dissolution by adding a frozen droplets of ascorbate to the sample cup.⁸⁵ UV photo-induced radicals have recently been proposed as an alternative to persistent radicals,^{86;81} the basic principle behind them being that by carefully choosing a precursor molecule, a radical species can be generated from it by shining UV light at low temperature. The resulting radical is labile and annihilates at temperatures above 170 K, thus overcoming the need for radical scavenging/filtration before injection. The use of UV-radicals opens the possibility of being able to store and transport between different sites hyperpolarized compounds,⁸⁷ thus making dDNP experiments more widely accessible.

For DNP to be efficient, the polarizing agent needs to be dissolved and homogeneously distributed within the matrix. A glassy sample is therefore sought-after. If the substrate does not form a glassy solid when frozen alone or in solution, crystallization can be prevented by mixing or dissolving it in a suitable co-solvent like glycerol or DMSO. Depending on the magnetic field strength and polarizing agent, the glassing solvent can be fully or partially deuterated. Up to 5 T, higher polarization levels can be obtained with a fully-deuterated matrix when the polarizing agents have a broad ESR linewidth. Conversely, fully-protonated matrices are found to work better with narrow ESR radicals.^{88;89} The reasons behind such behavior can be traced back to the DNP mechanism promoting the polarization transfer and will be discussed in Chapter 5. At magnetic fields higher than 5 T, on the other hand, a clear and reproducible trend across samples was not observed, and sample optimization is required.

Low concentrations (1-2 mM) of chelated Gd^{3+} are observed to improve the DNP enhancement of factors up to 50-100 %. The improvement is due to the combined shortening of the electron spin-lattice relaxation time T_{1S} and a narrowing on the radical ESR line.^{89;90;91} In particular, on a sample of glucose in H_2O :glycerol doped with trityl, the optimal gadolinium concentration was found when the electronic T_{1S} and ESR line matched that of the same radical in pyruvic acid. On its own, Gd^{3+} was not observed to cause any DNP effect.⁹⁰

Finally, depending on the sample, neutralization prior to infusion of the hyperpolarized solution may be required. This can be achieved by adding a suitable amount of frozen acid/base solution in the sample cup prior to loading.

Overall, the main rationales for developing sample formulations for DNP-MR can be found

in Karlsson *et al.*⁹²

Sample dissolution

Once the sample is fully polarized, it can be rapidly dissolved and injected in the targeted system without significant polarization losses. The dissolution step requires a heated and pressurized (~ 10 bar) solvent, typically water, to be propelled onto the sample. Buffering of the dissolution solvent may be needed in order to maintain the pH in the physiological range and can be achieved with phosphate/TRIS buffers. EDTA is also usually added to chelate paramagnetic impurities that would otherwise be source of nuclear relaxation. Dissolution has to take place at a relatively high magnetic field to minimize the fast relaxation of the nuclear spins to their equilibrium state occurring at high temperatures. This is the reason why the sample is usually dissolved right above the liquid helium surface. The solution is then chased out of the polarizer using pressurized helium gas and collected prior to the *in vivo* *in vitro* infusion to allow for degassing.

Different strategies have been developed to automatically inject the hyperpolarized sample. Comment *et al.*⁷¹ designed a separator-infusion pump to collect the sample out of the dissolution line and inject it *in vivo* in a rodent placed in an MRI scanner. The injection is activated using a hydraulically-driven piston, and starts 3 s after dissolution. Katsikis *et al.*⁹³ proposed a design for the automatic injection of the hyperpolarized solution into a 5 mm NMR tube placed in a high-resolution magnet employing Arduino-based software control. The setup depends on a two-state valve that directs a predefined sample volume into the NMR tube.

Conclusions

The basic components of a dDNP setup are all commercially available and reasonably affordable, but operation costs are usually quite high. These costs can be significantly decreased by installing the most recently developed systems, at the expense of a substantial initial investment. Having the setup in place, sample formulation has to be addressed: while there are a few rationales that can be followed to prepare the sample, when targeting a new substrate a careful optimization is always required. Not discussed in the present chapter but an important consideration for applications are the acquisition strategies to put in place once the dissolved substrate is injected *in vivo*.

4 ^{13}C dynamic nuclear polarization using SA-BDPA at 6.7 T and 1.1 K: co-existence of pure thermal mixing and well-resolved solid effect

Adapted from:

^{13}C dynamic nuclear polarization using SA-BDPA at 6.7 T and 1.1 K: coexistence of pure thermal mixing and well-resolved solid effect

Radaelli A, Yoshihara HAI, Nonaka H, Sando S, Ardenkjaer-Larsen JH, Grütter R, Capozzi A. J Phys Chem Lett 2020, 11, 16:6873-6879.

DOI: <https://doi.org/10.1021/acs.jpclett.0c01473>

This work results from a collaboration with the Hypermag center at the Denmark Technical University and the University of Tokyo. SS and HN synthesized the SA-BDPA radical. I performed experiments in collaboration with AC, and analyzed the data. HAIY did the molecular models to estimate the inter-radical distance. AC derived the formula for the cutoff frequency Δ_0 . The interpretation of the data and the manuscript writing have been done by myself in collaboration with all the co-authors.

Abstract

SA-BDPA is a water-soluble, narrow-linewidth radical whose DNP properties to date have only been studied in magic angle spinning (MAS)-DNP conditions. Here, the LOD-ESR and ^{13}C DNP properties at 6.7 T, 1.1 K of an 8.4 M ^{13}C urea sample in a water:glycerol matrix doped with either 60 mM or 120 mM SA-BDPA are reported. DNP microwave frequency sweep profiles revealed the presence of two distinct DNP mechanisms promoting the polarization transfer: well-resolved solid effect and pure thermal mixing. Indeed, the very narrow radical ESR linewidth of the radical (30-40 MHz in the investigated concentration range), broadened predominantly by dipolar coupling, excluded any contribution from cross effect. Moreover, at 60 mM SA-BDPA, modulation of the microwave frequency led to a boost in the maximum achievable polarization *via* both thermal mixing and solid effect. These results, especially when compared to what is observed with the trityl radical AH111501, highlight the unusual ^{13}C DNP properties of SA-BDPA.

Introduction

For most low-gamma nuclei in dDNP conditions, the polarization transfer process takes place *via* cross effect and/or thermal mixing. As illustrated in Section 2.3, both mechanisms rely on triple-spin flips involving two electrons and a nucleus that, owing to the combined effect of the electronic dipolar coupling and the hyperfine interaction, change their relative orientation. The difference between CE and TM then lies in which reservoir provides the energy for the triple-spin flips to take place. While in CE the energy is provided by the electron Zeeman reservoir, in TM it is the electron non-Zeeman pool that supplies it. Therefore, cross effect requires an anisotropically-broadened ESR line, whereas TM entails a strongly-coupled electron dipolar system. Theoretically one can determine the dominant mechanism by estimating the ratio Δ_0/ω_I , Δ_0 being the maximum dipolar interaction between electron pairs Δ_0 . Experimentally, however, isolating the contributions of the two mechanisms is not straightforward. Indeed, CE and TM usually take place simultaneously, given that most radicals used in dDNP have an ESR linewidth greater than ω_I and are used at sufficiently high concentrations that ensure a strong dipolar coupling. Recently, Guarin *et al.*⁵⁴ provided an elegant experimental demonstration of the conditions necessary to exclude the contribution of thermal mixing from the DNP process. They investigated the ^1H , ^{13}C and ^{31}P DNP properties at 6.7 T, 4 K of a series of amorphous solids doped with nitroxide radicals at concentrations ranging between 10-100 mM. By looking at the evolution of the spin temperatures of the nuclear pools, both in the presence and absence of a microwave field, they observed that TM was quenched at sufficiently low radical concentration (< 50 mM), in line with an electron dipolar interaction not sufficiently strong to promote triple-spin flips. To the best of our knowledge, under these experimental conditions, no demonstration of the opposite, i.e. of DNP of low-gamma nuclei taking place solely *via* thermal mixing, has however been provided. This would require a narrow-ESR line radical primarily broadened by dipolar coupling.

We herein report the use of the polarizing agent SA-BDPA to perform dDNP on ^{13}C urea at 6.7 T, 1.1 K. SA-BDPA is a sulfonated water-soluble derivative of BDPA that, to date, has only been studied in magic anfile spinning (MAS)-DNP conditions.^{94;95;96;97;98} We performed LOD-ESR and ^{13}C DNP measurements of samples of 8.4 M of ^{13}C urea dissolved in a solution of water:glycerol and doped with either 60 or 120 mM of SA-BDPA. For comparison, we also investigated a ^{13}C urea sample doped with 30 mM of trityl AH111501 radical.

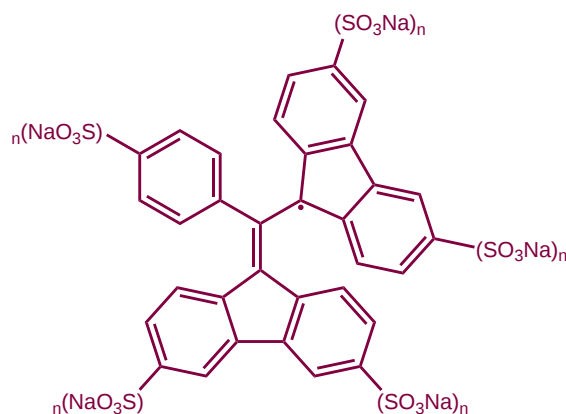


Figure 4.1 – Molecular structure of SA-BDPA.

Methods

Sample preparation

SA-BDPA was synthesized following a procedure described by Haze *et al.*⁹⁴ Our preparation showed a UV-vis absorbance maxima at 508 nm and 881 nm as previously reported⁹⁴ (data not shown). 250 mg of ^{13}C urea (Sigma-Aldrich, Buchs, SG, Switzerland) was dissolved in 320 μL of a 50:50 (v/v) solution of water:glycerol. The urea concentration was measured to be 8.4 M. Either 60 or 120 mM of SA-BDPA (nominal concentration, MW = 817.82 g/mol), or 30 mM trityl AH111501 (GE Healthcare, Denmark A/S) were then dissolved in the urea solution by sonication at 40°. The three samples are referred to as SA60, SA120, and TR30, respectively.

LOD-ESR measurements

LOD-ESR measurements were performed at 6.7 T, 1.1 K following methods previously described.⁸¹ On all three samples, the ESR spectrum was measured twice by sweeping over the frequency range in steps of 5 MHz. At each step, microwaves were switched on and off at a rate of 5 Hz (lock-in demodulation frequency). The average signal intensity was then plotted against the microwave frequency. The electron spin-lattice relaxation time T_{1S} was measured by recording the full evolution of the ESR signal as a function of time upon microwave chopping. In this case, the demodulation frequency was decreased to 0.4 Hz for the SA-BDPA samples, and to 0.2 Hz for the AH111501 sample. The curves were then fitted to the function: $S = A [\exp(-t/T_{1S}) - \exp(-t/\tau)]$, with S , A and τ the ESR signal intensity, a proportionality constant and the pickup coil time constant, respectively. The T_{1S} measurements were repeated three times, and the values are expressed as mean \pm S.D.

DNP experiments

All solid-state ^{13}C NMR acquisitions were performed at 6.7 T, 1.1 K using a Varian INOVA console (Palo Alto, CA, USA). The ^{13}C DNP microwave frequency profile was acquired by shining microwave radiation on the sample for 30 min at each frequency. After acquiring an NMR spectrum with a 5° hard pulse, the signal was saturated with a train of 50000 5° rf-pulses at a rate of 50 kHz. For all samples, the full polarization build-up was monitored by applying a 2° hard pulse every 5 min. On the SA-BDPA samples, the sweeps and build-ups were repeated for three different microwave frequency modulation amplitudes: 0, 10 and 25 MHz, at a modulation rate of 1 kHz and following a sine function modulation scheme.

The ^{13}C urea signal enhancement was measured in liquid state at 37°C . After at least 2 hours of microwave radiation, the samples were rapidly dissolved with 8 mL D_2O + EDTA and manually transferred in approximately 10 s in a 10 mm NMR tube. The NMR tube was subsequently placed in a 9.4 T vertical bore magnet (Agilent, Palo Alto, CA, USA), and the hyperpolarized signal decay was monitored by applying a 5° hard pulse every 3 s. After complete relaxation of the signal, 100 μL of gadodiamide (50 mM) were added to the sample to shorten the nuclear spin-lattice relaxation time $T_{1\rho}$. The thermal signal was then measured by averaging 400 scans with a repetition time (TR) of 2 s and the same flip angle as for the hyperpolarized measure. The enhancement was calculated as the ratio between the hyperpolarized and the thermal signal. These measurements were repeated three times on the SA120 sample, twice on the TR30 sample, and once on the SA60 sample. For samples where repeated measurements were performed, polarization level and buildup times are expressed as mean \pm S.D., otherwise a 10 % error was attributed to the experimental values.

Estimation of minimum inter-radical distance

3-dimensional molecular models of SA-BDPA and trityl AH111501 were generated using MarvinSketch (ChemAxon, Budapest, HU). For each radical, two copies were manually fit in a close-packing interaction without steric clashes using PyMol (<https://pymol.org>). Side chain conformational flexibility and electrostatic interactions were not taken into account when generating these models. Stereoscopic images of the packed radical pairs and Van der Waals (Connolly) surfaces were generated with ChimeraX (<http://www.rbvi.ucsf.edu/chimerax>). In these models, the SA-BDPA radicals are separated by 8 Å, and the AH111501 radicals by 10.5 Å, but closer packing may be possible taking conformational flexibility into account.

Results

^{13}C microwave frequency sweep profiles of the SA60 sample presented uncommon features, as Figure 4.2 shows. With monochromatic microwave irradiation, in addition to the set of lobes overlapping with the ESR spectrum, positive DNP enhancement was also measured at frequencies around 187.90 GHz and negative DNP enhancement around 188.04 GHz. These maxima, of lower intensity than the central ones, were separated in frequency by 144 ± 1.0 MHz. With 10 MHz microwave frequency modulation, the two sets of lobes grew in intensity and the central one shifted further from the zero-crossing frequency. With 25 MHz of modulation, the outer set was no longer discernible from the inner one, which instead shifted of approximately 25 MHz away from the zero-crossing frequency. Moreover, the enhancement almost doubled compared to the non-modulated case. The ESR spectrum (Figure 4.2) was centered at $\omega_S = 187.97$ GHz and presented a fairly symmetric shape, in line with the radical having a negligible **g**-tensor anisotropy and unresolved hyperfine coupling to protons.^{94;95} The full-width-at-half-maximum (FWHM) was only 30.5 ± 1.0 MHz, less than half the ^{13}C Larmor frequency at 6.7 T (71.8 MHz), and comparable to what was previously reported.^{94;95} The radical longitudinal relaxation time (T_{1S}) measured 230 ± 4 ms, as shown in Figure 4.2.

For the SA120 sample, T_{1S} decreased by approximately 10% compared to SA60, revealing a relatively small dependence on radical concentration (Figure 4.3). The ESR linewidth, on the other hand, increased by 30%, with a FWHM of 41.5 ± 1.0 MHz. This is consistent with a stronger dipolar interaction among the electron spins due to the increased radical concentration (Figure 4.3). Doubling the radical concentration also affected the DNP spectra. With monochromatic microwaves, the two sets of lobes were still visible, but the separation between them was less marked, in particular for positive enhancements (Figure 4.3), and at 10 MHz modulation amplitude the two sets merged together. The enhancement was observed to be independent of the microwave modulation amplitude.

For the trityl sample (TR30), the ESR spectrum presented an asymmetric line-shape due to its characteristic **g**-tensor anisotropy, in good agreement with previous studies at high field^{99;100} (Figure 4.4). The center of gravity was at 188.015 GHz, and the FWHM was 110 ± 5 MHz. The T_{1S} was 610 ± 15 ms, approximately three times longer than that of the SA-BDPA samples. In this case, the microwave frequency sweep profile displayed the typical two-lobed DNP pattern (Figure 4.4) and no DNP enhancement was measured outside the ESR line. Here, the effect of microwave modulation was not investigated, as it was previously shown not to be beneficial when using trityl radicals.^{69;91}

The DNP performance of the three samples were compared at their best DNP condition (Figure 4.5, 4.6, experimental details in Table 4.1). A liquid-state ^{13}C polarization of 25.8 ± 2.6 % was measured on the SA60 sample, and this value increased to 42.7 ± 3.4 % for the SA120

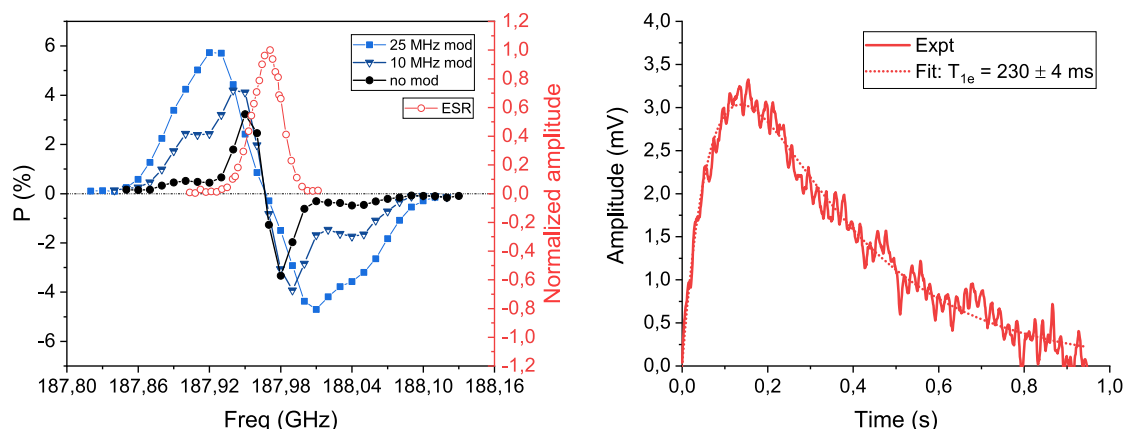


Figure 4.2 – ^{13}C DNP and ESR properties of 8.4 M ^{13}C urea doped with 60 mM SA-BDPA radical (SA60 sample). Left: normalized LOD-ESR spectrum of the radical and ^{13}C DNP frequency sweep profiles at different microwave frequency modulation amplitudes (modulation rate: 1 kHz). The LOD-ESR spectrum intensity was normalized to 1, while the DNP profiles were normalized according to the polarization measured after dissolution for the best performing conditions (i.e. 25 MHz microwave frequency modulation amplitude). Right: representative LOD-ESR buildup and decay curve with fit used to measure T_{1e} . All measurements were performed at 6.7 T, 1.1 K.

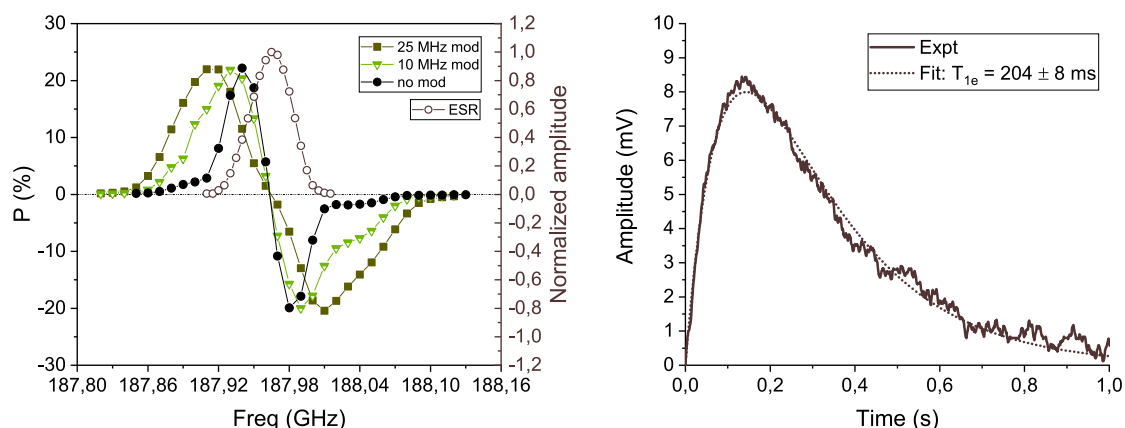


Figure 4.3 – ^{13}C DNP and ESR properties of 8.4 M ^{13}C urea doped with 120 mM SA-BDPA radical (SA120 sample). Left: normalized LOD-ESR spectrum of the radical and ^{13}C DNP frequency sweep profiles at different microwave frequency modulation amplitudes (modulation rate: 1 kHz). The LOD-ESR spectrum intensity was normalized to 1, while the DNP profiles were normalized according to the polarization measured after dissolution for the best performing conditions (i.e. 25 MHz microwave frequency modulation amplitude). Right: representative LOD-ESR buildup and decay curve with fit used to measure T_{1e} . All measurements were performed at 6.7 T, 1.1 K.

sample. The polarization buildup time constant τ_p decreased from 16200 ± 2000 s to 3070 ± 60 s upon doubling the SA-BDPA concentration. Overall, the TR30 sample showed the best performance in terms of both polarization level and build-up time constant, with values

Chapter 4. ^{13}C dynamic nuclear polarization using SA-BDPA at 6.7 T and 1.1 K: coexistence of pure thermal mixing and well-resolved solid effect

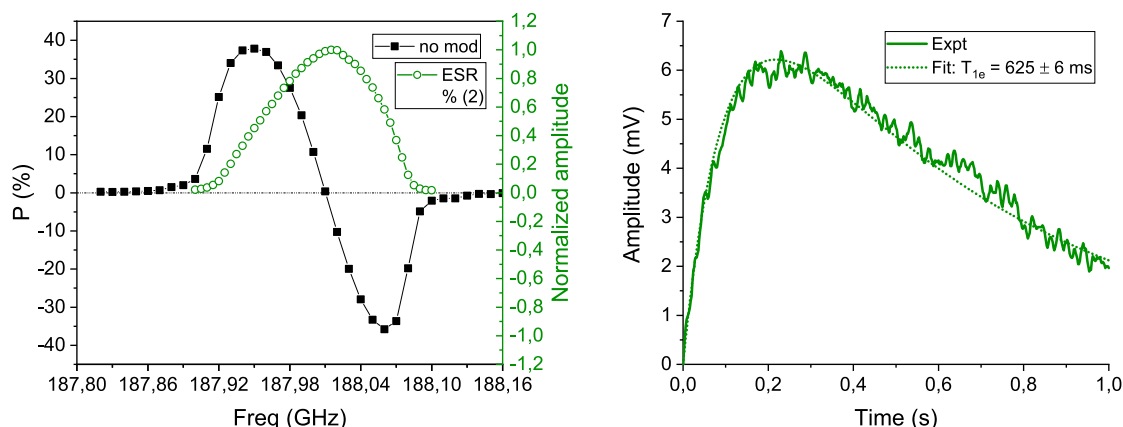


Figure 4.4 – ^{13}C DNP and ESR properties of 8.4 M ^{13}C urea doped with 30 mM AH111501 trityl radical (TR30 sample). Left: normalized LOD-ESR spectrum of the radical and ^{13}C DNP frequency sweep profiles. Right: representative LOD-ESR buildup and decay curve with fit used to measure T_{1S} . All measurements were performed at 6.7 T, 1.1 K.

comparable to those previously reported.^{83;69;91}

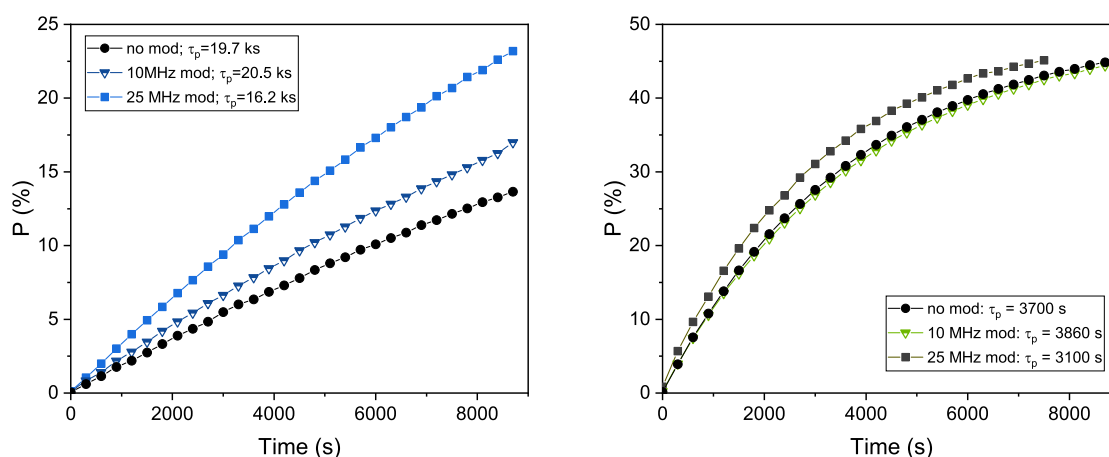


Figure 4.5 – Representative ^{13}C polarization buildup curves at 6.7 T, 1.1 K of the SA60 (left) and SA120 (right) samples at the three investigated microwave frequency modulation amplitudes.

Discussion

At low SA-BDPA concentration, the ^{13}C microwave frequency sweeps present evidence of an interplay of two different mechanisms in the polarization transfer process. Outside the ESR line, the two peaks at a relative distance of twice the nuclear Larmor frequency can be ascribed to the well-resolved solid effect.^{8;101;102} Unusual under these experimental conditions, solid effect involves zero-quantum and double-quantum transitions induced by the

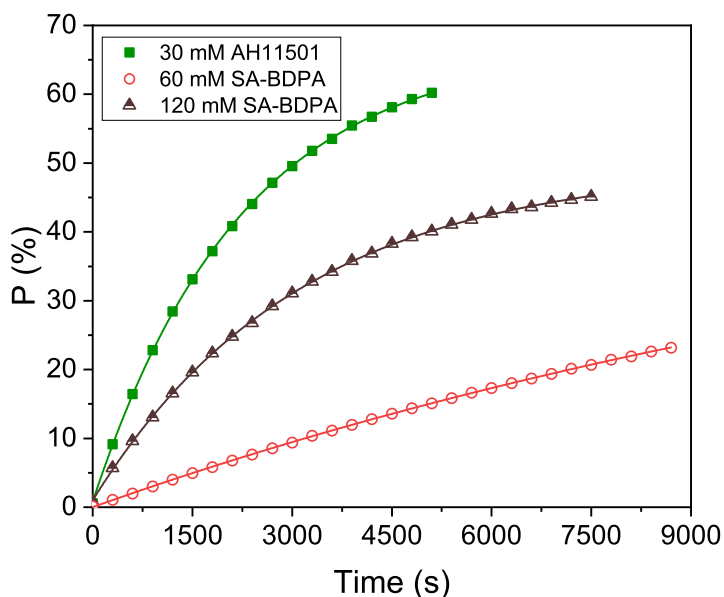


Figure 4.6 – Representative ^{13}C urea polarization buildup curves of the SA-BDPA and AH11501 samples at 6.7 T, 1.1 K. While the trityl data were acquired while shining monochromatic radiation, the SA-BDPA datasets were acquired with a modulation amplitude of the microwave frequency of 25 MHz. The reported polarization levels are the back-calculated values from the liquid-state measurements.

Table 4.1 – Summary of the experimental parameters and results.

Sample	LOD-ESR parameters		DNP parameters			DNP parameters		
	FWHM (MHz)	T_{1S} (ms)	μw freq (GHz)	Mod ampl (MHz)	τ_p (s)	SS P (%)	LS T_{1I} (s)	LS P (%)
SA60	30.5 ± 1.0	230 ± 4	187.93	25	16200 ± 2000	30.6 ± 3.0	58 ± 4	25.8 ± 2.6
SA120	41.5 ± 0.5	204 ± 8	187.91	25	3070 ± 60	42.8 ± 3.4	58 ± 1	36.0 ± 3.0
TR30	110.0 ± 5.0	610 ± 15	187.93	0	2060 ± 160	64.5 ± 1.8	55 ± 5	53.5 ± 1.5

microwave field when the conditions: $\omega_{\mu w} = \omega_I + \omega_S$ and $\omega_{\mu w} = \omega_I - \omega_S$, respectively, are met. The intensity of the two peaks is weak, as SE is a second order process that strongly depends on the microwave power.^{94;95;102} The enhancement of the nuclear spins near the center of the ESR spectrum is instead ascribed to triple-spins flips at the base of DNP *via* cross effect and thermal mixing. In the case of SA-BDPA, the ESR linewidth is smaller than the ^{13}C Larmor frequency and therefore it is unlikely to find two distinct electron spin packets S, S' with a Zeeman energy difference sufficiently large to satisfy the CE condition: $\omega_I = \omega_S - \omega_{S'}$. Thermal mixing, on the other hand, can drive the polarization transfer in this frequency range provided that the condition: $\Delta_0 \geq \omega_I$ is met. For an ensemble of randomly oriented electron

Chapter 4. ^{13}C dynamic nuclear polarization using SA-BDPA at 6.7 T and 1.1 K: coexistence of pure thermal mixing and well-resolved solid effect

spins, Δ_0 can be expressed in frequency units as:¹⁰²

$$\Delta_0 = \sqrt{\frac{1}{5}} \frac{\mu_0}{4\pi^2} \frac{\hbar \gamma_S^2}{r_0^3}$$

with r_0 the minimal distance between two radicals. A derivation of this formula can be found in the Appendix A. The minimal distance between SA-BDPA electron pairs estimated by means molecular modeling was 8 Å, corresponding to a Δ_0 value of 91 MHz, i.e. 1.3 times the ^{13}C Larmor frequency at 6.7 T. It is therefore reasonable to ascribe the center lobes of the microwave spectrum to electron dipolar energy transfer to nuclei.^{59;61} This interpretation is further supported by the fact that when the SA-BDPA concentration is doubled, and the electrons are thereby more strongly coupled together, thermal mixing becomes more efficient, and the process leads to a higher polarization and a smaller build-up time constant.

The cut-off frequency model of TM does not consider the possibility of radicals clustering. In this regard, an interesting remark can be made concerning an old experiment performed in 1976 by W. de Boer on ^1H nuclei in a *m*-xylene-*d*₆ sample doped with BDPA at 2.5 T and 0.5 K.¹⁰³ In that case the well-resolved solid effect was the main mechanism, but some TM was still visible although the proton Larmor frequency was greater than the radical linewidth and the radical concentration was only $6 \cdot 10^{18}$ spins/cm³ (10 mM).

Unlike the case with trityl, microwave frequency modulation was observed to boost the ^{13}C urea polarization level in the 60 mM SA-BDPA sample. This behavior is readily explained within the thermal mixing framework by looking at one of the other essential elements in the DNP process, spectral diffusion.^{102;56;104} When spectral diffusion is fast compared to the electron spin-lattice relaxation time, the hole burned by the microwave into the ESR spectrum spreads across its whole width via energy-conserving electron-electron flip-flops. In this case, all the electron spins participate in the polarization transfer to nuclei. Conversely, with slow spectral diffusion, only a fraction of electron spins will participate, making the DNP mechanism less efficient.^{102;56} The flip-flop transition probability is a function of the electron spins' average dipolar coupling and increases with radical concentration.^{102;57} If the coupling is not sufficiently strong compared to the ESR line width, microwave frequency modulation can help in broadening the initial hole by engaging more spin packets.^{77;78;79}

When the SA-BDPA concentration is raised to 120 mM, no boost in polarization level is obtained by modulating the microwave frequency. This is consistent with the lower gains in enhancement at increasing radical concentration and at a given modulation amplitude previously observed,^{78;79} and can be related to the stronger dipolar coupling between electrons that renders spectral diffusion more efficient.

It is worth noting that, in the SA60 sample, microwave frequency modulation also yielded an

increase of the SE enhancement. At 10 MHz modulation amplitude, where the SE and TM lobes could still be resolved, the SE enhancement improvement was proportionally higher than the TM one, suggesting it is not a mere effect of the superposition between TM and SE. This phenomenon is new and deserves further investigation. Herein, we propose a qualitative argument. The g -anisotropy being negligible (see Figure 3 in Haze *et al.*⁹⁴), a possible explanation might be related to SA-BDPA's unresolved hyperfine interaction to protons. Early reports show that, when modulating the frequency with sufficient amplitude, all hyperfine lines within the modulated range share the power. As a consequence, a larger part of the ESR spectrum responds to the excitation rather than only the electron spins on resonance with monochromatic irradiation.¹⁰⁵ Therefore, several forbidden-transitions can be excited at the same time speeding up the DNP process and making it more efficient.

With tritylAH111501, the polarization transfer was ascribed to CE. The tritylAH11150 molecule is too large to fulfill the cut-off frequency condition ($r_0 = 10.5 \text{ \AA}$, $\Delta_0 = 40 \text{ MHz} < \omega_I$). But in this case, differently from SA-BDPA, the radical g -tensor anisotropy results in electron spin packets spreading across almost 150 MHz, thus allowing for the CE condition to be met. In this regard, it is worth noting that J. Wolber *et al.*⁵² in the context of ^1H dDNP at 3.35 T using trityl radicals did not report any enhancement overlapping with the radical ESR line. Indeed, there, with a proton $\omega_I = 144 \text{ MHz}$, neither the TM condition nor the CE one could be fulfilled.

The DNP performance difference between trityl and SA-BDPA was remarkable. This can be ascribed to the cut-off frequency being very close to the ^{13}C Larmor frequency for SA-BDPA, meaning that only few radical pairs hold enough dipolar energy to participate to TM. The polarization transfer process is therefore less efficient than with trityl, which relies instead on a well-matched CE condition.

At 3.35 T, BDPA and its benzyl derivatives at concentrations between 40 mM and 60 mM have been reported to yield excellent polarization levels in a very short time,^{106;107;90} whereas at 6.7 T SA-BDPA yielded high ^{13}C polarization only at substantially higher radical concentration. The latter did not appear to have any detrimental effect on the ^{13}C urea liquid state relaxation time $T_{1\rho}$ (Table 4.1); however, investigating whether this high amount of radical would present an issue for possible future applications remains to be determined. Whether an even higher radical concentration would be beneficial in terms of DNP efficiency was not investigated. Furthermore, an increase in the ^{13}C DNP performance of SA-BDPA is not expected to take place upon sample doping with a metallic complex as it is the case with trityl and, partially, with BDPA,^{90;108;91} primarily because of the already short electronic T_{1S} of the radical.

Finally, we can note that, when investigating low-gamma nuclei, while the well-established

Chapter 4. ^{13}C dynamic nuclear polarization using SA-BDPA at 6.7 T and 1.1 K: coexistence of pure thermal mixing and well-resolved solid effect

criterion for TM mechanism occurrence, which relies on the comparison between the radical ESR spectrum FWHM and the Larmor frequency of the nucleus of interest ($\text{FWHM} > \omega_I$),^{62;102} may be appropriate for very broad radicals like nitroxides, it does not necessarily hold for all narrow linewidth radicals. The cut-off frequency Δ_0 being a crucial parameter, it would be more appropriate to consider the full ESR spectral width at its base instead. In our case these values measured 81 ± 5 MHz for the SA60 sample and 99 ± 5 MHz for the SA120 sample, thus matching the TM condition for the ^{13}C Larmor frequency at 6.7 T. An extreme case would be represented by radicals showing an ESR linewidth much smaller than the nuclear Larmor frequency. Here, the strong dipolar couplings offering a mechanistic basis for TM-DNP would exceed by far the spectrum FWHM and tend to broaden into the background, making them difficult to be detected experimentally. This has been recently demonstrated to be possible by Equbal *et al.* in the case of ^1H TM-DNP at 7 T using trityls at very high concentration.¹⁰⁹ They reported proton enhancement spreading over 300 MHz, while the ESR linewidth measured only 100 MHz. This represents a clear case where the ESR spectrum FWHM does not correspond to the DNP mechanism involved because of radical clustering. This study provided also experimental evidence of another parameter of remarkable importance for efficient thermal mixing: the asymmetry of the dipolar coupling network.⁵⁹ Although we could not directly observe it in our experiments, this asymmetry is the key for a pure quantum mechanics treatment of TM.

Conclusions

In this study we investigated the properties of the water-soluble radical SA-BDPA in dDNP conditions for direct ^{13}C urea hyperpolarization. The unique properties of this polarizing agent at 6.7 T, 1.1 K allowed us to observe two distinct ^{13}C DNP mechanisms, well-resolved SE and TM. To the best of our knowledge, this is the first experimental demonstration of such a resolution of separate DNP mechanisms on a low-gamma nucleus.

5 Effects of glassing matrix deuteration on ^6Li dynamic nuclear polarization

Adapted from:

Effects of glassing matrix deuteration on ^6Li dynamic nuclear polarization

Radaelli A, Capozzi A, Yoshihara HAI, Mishkovsky M, Grütter R.

Manuscript in preparation.

My contribution consisted in performing experiments and data analysis. The interpretation of the data has been done by myself in collaboration with the co-authors.

Abstract

The effect of glassing matrix deuteration on DNP of low-gamma nuclei at high magnetic fields is not completely understood. Here, we report the influence of solvent deuteration on ^6Li DNP at 7 T, 1 K of $^6\text{LiCl}$ samples doped with either the broad-linewidth radical TEMPOL or the narrow-linewidth trityl OX063 radical. Upon solvent deuteration, a slow-down of the ^6Li DNP dynamics was observed on all samples. While with trityl this did not result in a significant variation in the final ^6Li polarization level, with TEMPOL the fully-deuterated sample polarized so slowly that at the time of dissolution the polarization level was approximately 30 % lower. OX063 was found to be less efficient than TEMPOL, resulting in lower ^6Li polarization levels and slower buildup dynamics, likely because of the long spin-lattice relaxation time of the radical. Additional measurements performed on the TEMPOL samples showed that at 1.5 K solvent deuteration had no significant effect on the polarization level.

Introduction

When hyperpolarizing low-gamma nuclei, deuteration of the glassing matrix can influence the DNP efficiency in a way that depends on the properties of the polarizing agent. Experiments on a number of ^{13}C -labeled substrates^{67;88;89;110} have shown that for temperatures in the range of 1-2 K and magnetic fields between 3-5 T, the use of deuterated solvents improves the ^{13}C polarization level with gains as high as 100 % when broad ESR linewidth radicals like nitroxide radicals are employed. The opposite trend is instead observed with radicals with a narrow ESR line like trityls and BDPA; with these polarizing agents, DNP is more efficient with protonated matrices. The rationale behind these observations is found in the mechanism responsible for DNP. In the investigated temperature and field range, the polarization transfer from broad linewidth radicals to the different nuclear species in the sample takes place *via* thermal mixing (TM). Then, as discussed in Section 2.3.1, the DNP process can be described using a thermodynamic model involving transfer of energy between reservoirs, namely the nuclear Zeeman, electron Zeeman and electron non-Zeeman reservoirs. While the microwave field has the net effect of cooling the electron non-Zeeman reservoir, a thermal contact established between the nuclear Zeeman and electron non-Zeeman reservoir induces heat transfer between the two, so that the spin temperature of the former is in turn reduced. Moreover, if multiple nuclear species are present in the sample, they all reach the same spin temperature. Given that the total nuclear Zeeman heat capacity scales with $\sim \sum_i N_i \omega_{Li}^2$, N_i being the number of spins of the species i , and that the gyromagnetic ratio of ^2H is significantly lower than that of ^1H (6.536 MHz/T *vs.* 42.577 MHz/T, respectively), deuteration of the solvent has the net effect of lowering the total nuclear Zeeman heat capacity. As a consequence, the electron non-Zeeman reservoir can cool the nuclear Zeeman reservoir to a lower spin temperature. The same does not apply when narrow line radicals are used as polarizing agents because with such radicals, under these conditions, ^1H are generally not polarized *via* thermal mixing⁵² as their Larmor frequency exceeds the radical spectral breadth.

At field strengths greater than 5 T, on the other hand, the effect of solvent deuteration on the DNP properties of low- γ nuclei is not well understood. At 7 T, and at both 1.5 K and 1 K, ^{13}C DNP of [1- ^{13}C]acetate and TEMPOL in a water:glycerol mixture was observed to be more efficient with a partially-deuterated glassing matrix, and higher polarizations were found to correlate with shorter buildup times.^{68;111} Breakdown of thermal mixing regime was assumed⁶¹ to be the cause of the discrepancy with low field behavior. In support of this hypothesis was the fact that the spin temperatures of ^1H and ^{13}C were not observed to equilibrate at steady-state. These observations were shown not to be general, as measurements performed on the same Na-acetate and TEMPOL sample in a water:ethanol matrix revealed that the use of a fully-deuterated solvent yielded more efficient DNP compared to the partially-deuterated one. Finally, consistently higher ^{13}C enhancement was observed at 7

Chapter 5. Effects of glassing matrix deuteration on ^6Li dynamic nuclear polarization

T, 4.2 K in fully-deuterated samples of 4.5 M ^{13}C urea compared to protonated ones.¹¹² Here, however, the polarization dynamics could be modeled using rate equations derived from the thermodynamic model of thermal mixing.

^6Li is a spin $I = 1$ nucleus characterized by a low gyromagnetic ratio ($\gamma_I = 6.266 \text{ MHz/T}$), a low natural abundance (7.42 %), a small quadrupolar moment ($Q = -0.083 \text{ fm}^2$) and a long liquid-state spin-lattice relaxation time T_{1I} ($\sim 500 \text{ s}$ for a 0.5 M $^6\text{LiCl}$ solution in D_2O at 9.4 T). The DNP properties of ^6Li have been studied in crystalline samples, as ^6LiD was a popular material for polarized targets.^{113;114;115} MAS-DNP has been successfully used to hyperpolarize $^6\text{Li}/^7\text{Li}$ ions in anodes of rechargeable lithium batteries, with the aim of exploiting the gain in sensitivity to probe the local environment of electrodes, electrolytes, and their interface.^{116;117} DDNP biological applications of hyperpolarized ^6Li have generally relied on the good sensitivity of the ion to paramagnetic species, as hyperpolarized $^6\text{Li}^+$ was successfully used to detect Gd^{3+} contrast agents in submicromolar concentrations in phantoms,¹¹⁸ and to probe the hemoglobin oxygenation level.¹¹⁹ Recently, hyperpolarized ^6Li was studied at pharmacological doses in the rat brain to evaluate whether its pharmacokinetic profile could be monitored in real time.¹²⁰

The aim of the present study was to determine if and how the presence of ^2H in the glassing matrix influenced the ^6Li DNP properties. The effects of deuteration were investigated at 7 T, 1 K/1.5 K using water:glycerol solutions of $^6\text{LiCl}$ (3 M) doped with either the nitroxyl radical TEMPOL or the trityl OX063 radical. LOD-ESR measurements of the samples were performed at the same field and temperatures to gain further insights on the DNP behavior.

Methods

Sample formulation

$^6\text{LiCl}$, 4-hydroxy-TEMPOL (TEMPOL), sodium-ascorbate, D_2O , glycerol and glycerol- d_8 were purchased from Sigma-Aldrich (Buchs, SG, CH), while trityl OX063 was purchased from Albeda Research (Copenhagen, DK).

TEMPOL samples: 3 M $^6\text{LiCl}$ and 58 mM TEMPOL was dissolved in a 1:1 (w/w) water:glycerol mixture. The solution was either fully deuterated (FD) 100 % (D_2O :gly- d_8), partially deuterated (PD) 50 % (H_2O :gly- d_8) or fully protonated (FP) 0 % (H_2O : gly).

Trityl samples: Samples of 3 M $^6\text{LiCl}$, 25 mM trityl OX063 in a 1:1 (w/w) water:glycerol mixture were prepared. In this case, the glassing matrix was either fully deuterated (FD) 100 % (D_2O :gly- d_8) or fully protonated (FP) 0 % (H_2O : gly).

Hyperpolarization

DNP measurements were performed in a custom-built polarizer operating at 7 T.⁷¹ ^6Li microwave frequency profiles were acquired on both sets of samples at 4.2 K. TEMPOL samples: the output power of the microwave source was kept constant at 50 mW, while the frequency was swept between 196.50 GHz and 197.25 GHz in steps of 0.05 GHz. At each frequency, the sample was polarized for 45 min, and the ^6Li polarization buildup monitored by applying small flip angle rf-pulses every 5 min. Trityl samples: given the narrower line of the radical, the DNP sweep profile was acquired between 196.52 GHz and 196.72 GHz in steps of 0.017 GHz, with constant microwave power of 50 mW. At each frequency, the sample was polarized for either 90 min (FP) or 130 min (FD), during which the polarization buildup was monitored using the same parameters as for the TEMPOL samples.

The 1 K DNP dynamics and polarization levels of each sample were probed by hyperpolarizing 8 frozen beads 8 μL in volume. For the TEMPOL samples, polarization measurements were also performed at 1.5 K. In this case, the sample volume was not kept fixed across experiments, and frozen pellets of Na-ascorbate in D_2O were added to the sample cup in suitable amounts to ensure radical quenching.^{85;119} Monochromatic microwave radiation centered at the optimal frequency for DNP was shone onto the samples for up to 5 h. During this time, the ^6Li solid-state polarization buildup was monitored by applying small flip angle ($\lesssim 5^\circ$) rf-pulses every 5 min. The ^6Li signal enhancement was measured in liquid state after rapid dissolution (with 6 mL D_2O) and transfer (3 s) to a separator-infusion pump placed in a 9.4 T rodent scanner (Magnex Scientific, Oxford, UK) interfaced with a VNMRs console (Varian, Palo Alto, CA). A single-loop ^1H and double-loop ^6Li coil were built around the separator-infusion pump and used to excite the spins and measure the NMR signal. The hyperpolarized ^6Li signal decay was monitored with a series of pulse-acquire scans (hard pulse, 9° flip angle, 10 s repetition time), while the thermal signal was measured by averaging multiple acquisitions using the same flip angle and $\text{TR} = T_1$. With this choice of flip angle and TR the steady-state magnetization was estimated to be greater than 99 %. For the 1.5 K measurements only, 5 μL of a 0.5 M gadoteric acid solution was added to the separator-infusion pump prior to the beginning of the thermal acquisition. In this case, owing to the effect of Gd^{3+} on the nuclear relaxation properties, the TR was reduced to 2 s. Three experiments per sample were acquired at 1 K. At 1.5 K, measurements were repeated twice on the PD and FD samples, and performed only once on the FP one.

LOD-ESR measurements

LOD-ESR measurements were performed in the same custom-built polarizer used for the DNP measurements using a method previously described.^{81;121} TEMPOL samples: the ESR

lineshape and electronic spin-lattice relaxation time T_{1S} of the fully-protonated and fully-deuterated samples were measured at both 1.5 K and 1 K. The ESR spectrum was probed by sweeping the frequency between 196.4 GHz and 197.4 GHz in steps of 10 MHz. At each step, the output power of the microwave source was modulated between 0 to 55 mW with a square wave at a frequency of 4.8 Hz, and the signal intensity was averaged over 10 s. The full evolution of the ESR signal with time, from which the T_{1S} value was extracted, was instead recorded at the center frequency of the ESR line by setting the modulation frequency to 0.16 Hz. 50 averages were acquired. Trityl samples: like in the DNP measurements, the ESR lineshape and electronic spin-lattice relaxation time were only measured at 1 K. For the ESR spectrum, the frequency was swept between 196.6 GHz and 196.9 GHz in steps of 4 MHz. The T_{1S} was measured at the center frequency by modulating the power at 0.1 Hz. 100 averages were acquired. Because of the noise in the experimental data, the signal was filtered by placing a 15 Hz low pass filter at the output of the differential amplifier.

Data analysis

Measurements with three replicates are expressed as mean \pm standard deviation. A 10 % error was assigned otherwise. Buildup time constants were derived by fitting the DNP curves with a single exponential function, with the exception of the 1 K buildups of the FD TEMPOL sample, for which a double-exponential function better matched the data. Liquid-state nuclear spin-lattice relaxation time T_{1L} values were extracted from the fit of the exponential decay of the hyperpolarized signal and corrected for rf-pulse depletion.

The electronic spin-lattice relaxation time was estimated by fitting the experimental curves using: $y(t) = A \cdot (\exp(-t/T_{1S}) - \exp(-t/\tau))$, τ being the time constant of the circuit. τ was measured to be 13.4 ms at 1.5 K and 12.6 ms at 1 K in the TEMPOL experiments, and 20 ms in the trityl ones.

Results

In TEMPOL samples, the frequency sweep profile obtained at 4.2 K, shown in Figure 5.1 for the fully-protonated sample, presented a broad and asymmetric shape. The positive and negative maxima were found at (+): 196.65 GHz and (-): 197.1 GHz. The two maxima gave rise to approximately the same enhancement. In this temperature regime neither the enhancement nor the shape of the sweep profiles were influenced by the degree of deuteration of the glassing matrix (data not shown).

At 1.5 K the FP TEMPOL sample presented an average buildup time τ_p of 1180 ± 10 s and a corresponding liquid-state polarization level of 10.5 ± 1.0 %. Buildup time and polariza-

tion level slightly increased with increasing deuteron concentration in the glassing matrix, as shown in Table 5.1. A maximum polarization level of 12.0 ± 0.4 % and buildup time of 1470 ± 20 s were measured on the fully-deuterated sample.

At 1 K, the situation changed. The lower temperature led to both an increase in the final polarization level and a slow-down of the DNP rate. A ^6Li polarization of 17.4 ± 0.1 % was measured on the FP sample, while polarizations of 17.9 ± 0.5 % and 11.4 ± 3.4 % were measured on the partially- and fully-deuterated sample, respectively. Unlike the FP and PD samples, where upon lowering the temperature the buildup time increased by approximately 60 %, the FD sample presented a more severe slow-down of the DNP process. The buildup curve could no longer be fitted with a single exponential function, but two components were necessary to match the data. While the time constant of the fast component was comparable to τ_{pol} at 1.5 K, the slow component was characterized by a time constant of 13780 ± 2330 s. One should bear in mind that given the short duration of the experiment compared to the buildup time, this estimate is not extremely accurate. Table 5.2 summarizes the results obtained at 1 K, while Figure 5.3 shows representative buildup curves.

The trityl samples behaved somewhat differently. Deuteration of the glassing matrix did influence the shape of the ^6Li sweep profiles: the position of the positive and negative maxima did not change upon deuteration, with the positive maximum at 196.57 GHz and the negative at 196.655 GHz, but the lobes of the FP sample were slightly larger, and the zero-crossing was located at a different frequency.

At 1 K, a polarization level of 13.8 ± 0.7 % was measured on the fully-protonated sample, and 13.7 ± 1.2 % on the fully-deuterated one. A significantly faster DNP buildup was observed in the fully-protonated matrix (2200 ± 50 s *vs* 5170 ± 170 s in the FP and FD samples, respectively).

The ESR spectra of the investigated samples are shown in Figure 5.5, while the ESR parameters (FWHM and T_{1S}) are reported in Tables 5.1, 5.2 and 5.3. When the sample was doped with TEMPOL, at 1.5 K and 1 K deuteration of the glassing matrix reduced the radical linewidth by approximately 20 % and 25 %, respectively. The temperature did not appear to strongly influence the radical linewidth. A short electronic spin-lattice relaxation time of approximately 50 ms was measured on all TEMPOL samples, with neither temperature variation nor degree of deuteration of the glassing matrix having a significant effect on it. With trityl as a polarizing agent, the ESR linewidth grew slightly broader upon solvent deuteration, and concomitantly the ESR center frequency appeared to shift approximately 7 MHz higher. A T_{1S} of 1.27 s and 1.29 s was measured on the FP and FD samples, respectively.

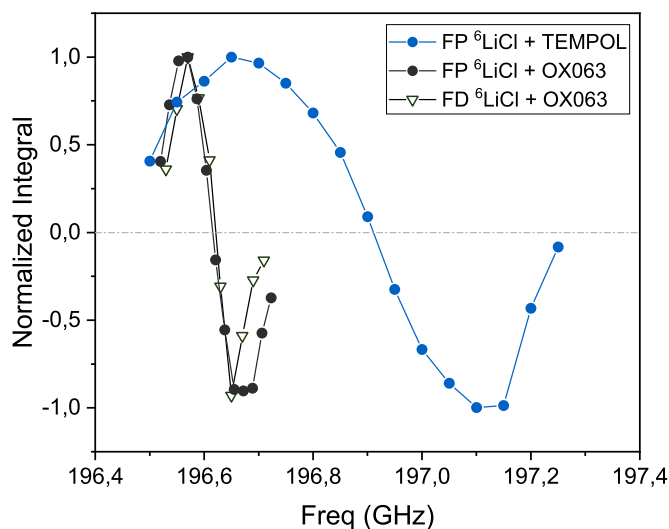


Figure 5.1 – ^6Li frequency sweep profiles acquired at 7 T, 4.2 K. The lines connecting the points are drawn to guide the eye.

Table 5.1 – Summary of the ESR and DNP properties of the three $^6\text{LiCl}$ and TEMPOL samples at 7 T, 1.5 K.

Sample	ESR parameters		DNP parameters		
	FWHM (MHz)	T_{1S} (ms)	τ_p (s)	LS P (%)	LS T_{1I} (s)
FP $^6\text{LiCl}$	380 ± 10	50 ± 5	1180 ± 10	10.5 ± 1.0	226 ± 22
PD $^6\text{LiCl}$	-	-	1200 ± 90	11.2 ± 0.4	264 ± 26
FD $^6\text{LiCl}$	305 ± 10	46 ± 5	1470 ± 20	12.0 ± 0.4	248 ± 20

Discussion

In the present study, the dependence of the ^6Li polarization level on the degree of solvent deuteration was investigated at two temperatures, 1 K and 1.5 K, and for two polarizing agents, TEMPOL and trityl OX063. The polarization measurements were performed in liquid state because of the excessively long solid-state spin-lattice relaxation time of ^6Li , that prevented an accurate estimate of the thermal polarization in a reasonable time frame. For the same reason, the ^6Li solid-state spin-lattice relaxation time was not measured. LOD-ESR measurements were performed at the same field and temperatures to determine how the electronic properties of the radicals affected the DNP process.

Neither the TEMPOL nor the trityl OX063 samples presented the linear dependence of the ^6Li signal enhancement with the degree of solvent deuteration characteristic of DNP *via* thermal mixing and reported for ^{13}C at lower magnetic fields.^{67;88;89;110}

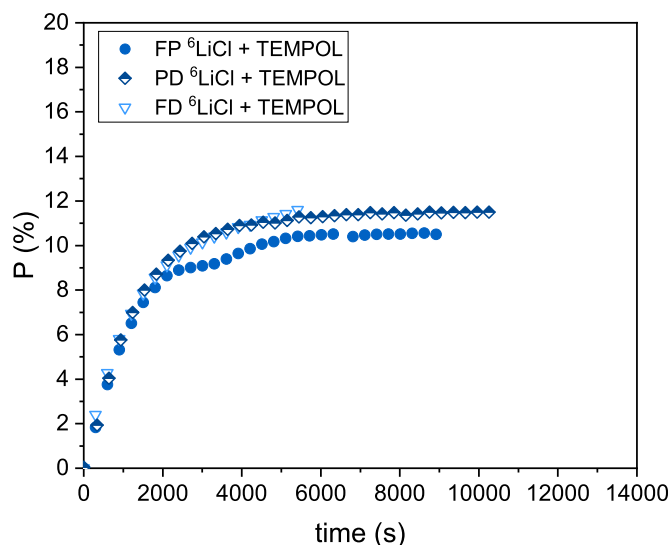


Figure 5.2 – Representative ^6Li buildup curves acquired at 7 T, 1.5 K on a 3 M $^6\text{LiCl}$ sample doped with 58 mM TEMPOL at different degrees (0 % FP, 50 % PD and 100 % FD) of solvent deuteration.

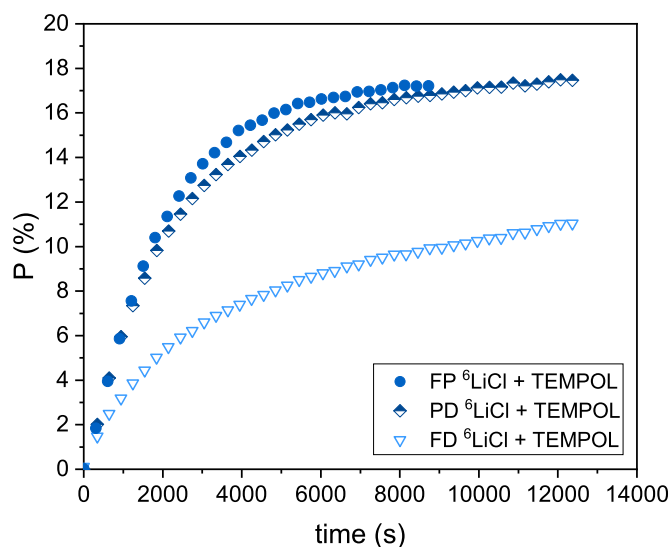


Figure 5.3 – Representative ^6Li buildup curves acquired at 7 T, 1 K on a 3 M $^6\text{LiCl}$ sample doped with 58 mM TEMPOL for different degrees (0 % FP, 50 % PD and 100 % FD) of solvent deuteration.

With TEMPOL, a significant difference in ^6Li polarization level across the three investigated matrices was not observed at 1.5 K, while the DNP dynamics were slightly slowed upon deuterium substitution. When the temperature was lowered to 1 K, while the FP and PD samples still presented similar ^6Li DNP properties, a significantly lower polarization level at the time of dissolution was measured in the FD sample, owing to a much longer buildup time

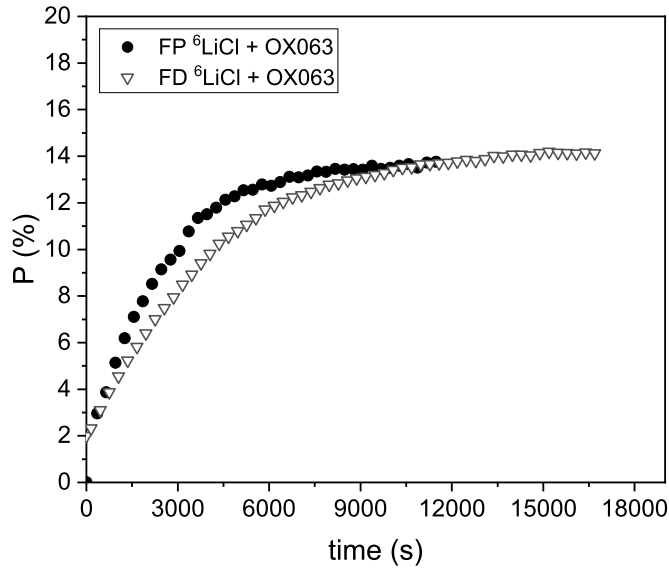


Figure 5.4 – Representative ^6Li buildup curves acquired at 7 T, 1 K on a 3 M $^6\text{LiCl}$ sample doped with 25 mM trityl OX063 for two degrees (0 and 100 %) of glassing matrix deuteration.

Table 5.2 – Summary of the ESR and DNP properties of the three $^6\text{LiCl}$ and TEMPOL samples at 7 T, 1 K.

Sample	ESR parameters		DNP parameters		
	FWHM (MHz)	T_{1S} (ms)	τ_p (s)	LS P (%)	LS T_{1I} (s)
FP $^6\text{LiCl}$	360 ± 10	51 ± 5	1860 ± 140	17.4 ± 0.1	176 ± 10
PD $^6\text{LiCl}$	-	-	1950 ± 160	17.9 ± 0.5	197 ± 35
FD $^6\text{LiCl}$	276 ± 10	49 ± 5	f: 1720 ± 100 s: 13780 ± 2330	11.4 ± 3.4	215 ± 6

constant. Unlike ^{13}C -labeled molecules polarized under the same conditions,^{68;111} higher ^6Li signal enhancements here did not necessarily correlate with faster DNP buildups. Overall, these results point to thermal mixing not being the dominant DNP process driving the polarization transfer. The same conclusion can be drawn by estimating the product of the autocorrelation function of the radical ESR spectra evaluated at the Larmor frequency of the nuclear pool of interest ($I = ^1\text{H}, ^2\text{H}$) and the Zeeman heat capacity of that same nuclear pool:

$$\frac{\int_{-\infty}^{\infty} d\omega g(\omega) g(\omega - \omega_I)}{\int_{-\infty}^{\infty} d\omega g^2(\omega)} \cdot N_I \omega_I^2 \quad (5.1)$$

Here, $g(\omega)$ is the ESR lineshape normalized over its area, $N_I \omega_I^2$ is the nuclear Zeeman heat capacity, and the ratio of the two integrals represents the probability that two electrons sep-

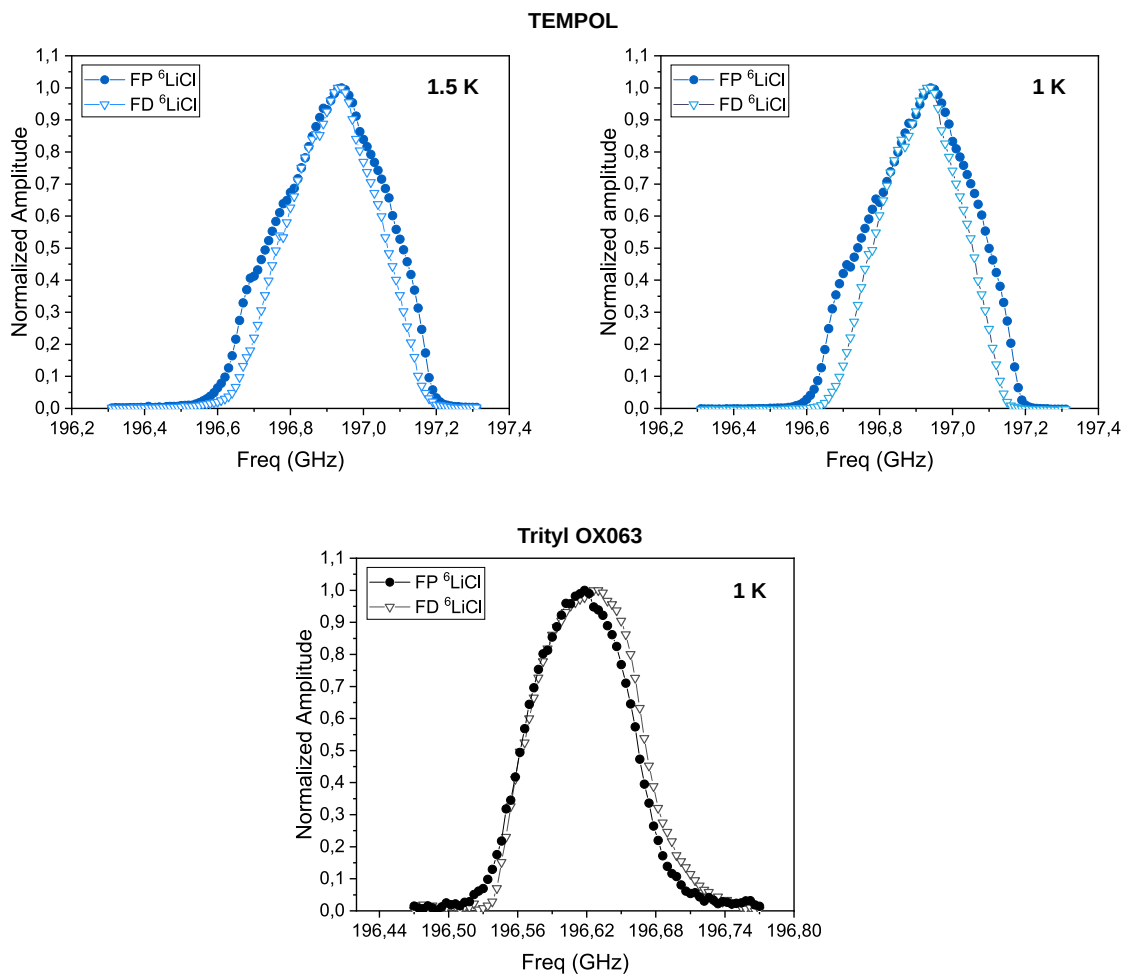


Figure 5.5 – ESR spectrum of the investigated samples at 7 T, 1.5/1 K.

arated in frequency by ω_I participate in a flip-flop.^{122;123} In thermal mixing, the product 5.1 gives an estimate of the “weight” on the process of the nuclear Zeeman reservoir of the species of interest, with the autocorrelation function indicating the degree of thermal contact between the electron non-Zeeman and nuclear Zeeman reservoirs. As expected, the normalized autocorrelation function of the TEMPOL ESR spectrum evaluated at the Larmor frequency of protons is smaller than that at the deuterium frequency: 0.30 (^1H) *vs.* 0.95 (^2H) at 1 K, and 0.33 (^1H) *vs.* 0.96 (^2H) at 1.5 K. However, the much larger Larmor frequency of ^1H compared to ^2H results in the product 5.1 being higher for the proton pool of about a factor 17 at 1 K and 18 at 1.5 K. Therefore, if thermal mixing were the dominant mechanism, this calculation would tell us that deuteration of the glassing matrix should lead to a more efficient ^6Li DNP, which is not observed here.

LOD-ESR measurements of TEMPOL revealed that at 7 T, 1.5/1 K the electronic spin-lattice relaxation time of the radical was approximately 50 ms and did not depend either on temper-

Chapter 5. Effects of glassing matrix deuteration on ^6Li dynamic nuclear polarization

Table 5.3 – Summary of the ESR and DNP properties of the FP and FD $^6\text{LiCl}$ and OX063 samples at 7 T, 1 K.

Sample	ESR parameters		DNP parameters		
	FWHM (MHz)	T_{1S} (s)	τ_p (s)	LS P (%)	LS T_{1I} (s)
FP $^6\text{LiCl}$	100 ± 4	1.27 ± 0.013	2200 ± 50	13.8 ± 0.7	252 ± 6
FD $^6\text{LiCl}$	110 ± 4	1.29 ± 0.013	5170 ± 170	13.7 ± 1.2	268 ± 27

ature or on matrix composition. With such a short electron T_{1S} the microwave radiation is likely only burning a hole in the ESR line. This is again in favor of the conclusion of thermal mixing not being the driving DNP process, as with a non-saturated ESR line the concept of spin temperature cannot be introduced to describe the electronic reservoirs. The fact that the electron spin-lattice relaxation time did not depend on temperature is in line with the expectation of having the electronic relaxation driven predominantly by the direct process.⁹⁹ While deuteration of the glassing matrix did not influence the electron T_{1S} , it narrowed the ESR spectrum. This effect cannot be solely explained with the decreased dipolar interaction deuterium substitution entails, as in a first approximation the dipolar interaction only accounts for few MHz of broadening.^{124;125}

With trityl OX063, the ^6Li polarization level was again independent of whether the solvent was protonated or deuterated, and deuteration was only observed to cause a slow-down of the polarization buildup. Again, this is a first indication that the DNP process is not solely driven by thermal mixing. The autocorrelation function of the ESR spectrum evaluated at the ^1H frequency is 0, while that of ^2H is 0.71. A protonated matrix would then be expected to make ^6Li DNP *via* thermal mixing more efficient, but again this is not what was found at 7 T, 1 K. The conclusion that thermal mixing is not the dominant DNP process under these conditions is further supported by the most recent models of DNP.^{60;61} As discussed in Sections 2.3 and 4.4, thermal mixing and cross effect can be described in terms of triple-spin flips where the energy for the transitions to take place is provided either by the electron non-Zeeman reservoir (TM), or by the electron Zeeman pool (CE). The key parameter that determines the relative strength of the two flows of energy is then the ratio of the maximum dipolar interaction between electron pairs, Δ_0 , to the nuclear Larmor frequency of the species of interest, ω_I . In particular, only if Δ_0 is greater than ω_I is thermal mixing expected to significantly contribute to the DNP process. In the case of trityls, whose larger size compared to TEMPOL limits the distance of electron pairs, Δ_0 is in the 40 MHz range, comparable to the ^6Li Larmor frequency at 7 T, so that the rate of the thermal mixing flow is expected to be equal to that of cross effect. One should note that this model does not account for the presence of radical clusters, which were shown to be beneficial to DNP *via* thermal mixing.¹⁰⁹

With both TEMPOL and trityl a slowdown of the ^6Li DNP dynamics was observed upon solvent deuteration. This may be due to the proximity of the ^6Li and ^2H resonance frequencies (43.90 MHz and 45.85 MHz, respectively, at 7 T) that may cause a competing effect in the polarization transfer process between the two nuclei, exacerbated by the higher concentration of deuterons compared to that of ^6Li . It is worth noting that at 1 K with TEMPOL partial deuteration of the solvent has very little impact on the DNP dynamics, and it is only when the matrix is fully-deuterated that the polarization buildup time considerably increases.

Surprisingly, doping the sample with 25 mM of trityl OX063 did not lead to DNP more efficient than with TEMPOL, as one would expect from what is observed on ^{13}C . This is likely related to the relatively long electronic spin-lattice relaxation time T_{1S} of the radical (~ 1.3 s). Theoretically, tuning the T_{1S} and spectral linewidth with a gadolinium complex should help improving the DNP performance. In the presence of leakage in the nuclear reservoir, i.e. nuclear relaxation sources other than the interaction with the radical, shortening the electron T_{1S} was indeed shown to be beneficial for DNP.^{126;90;91}

The investigated sample formulations presented favorable DNP properties. At 1 K with 58 mM of TEMPOL radical a ^6Li polarization level of 17.9 % was measured on the partially-deuterated sample, and similar performance was obtained on the fully-protonated one. The achieved polarization is almost double what has been reported in the literature.^{118;119;127;128} The value obtained with our sample formulation is fairly close to what can be obtained by means of cross-polarization ($^1\text{H} \rightarrow ^6\text{Li}$) at 6.7 T, 1.2 K.¹²⁸ Given the short electronic spin-lattice relaxation time T_{1S} the TEMPOL sample has, higher polarization levels should be attainable by modulating the microwave frequency.^{77;78;79}

Conclusions

The observed effect of glassing matrix deuteration on ^6Li DNP differs from previously reported measurements on ^{13}C . At 7 T, 1 K, with both narrow linewidth and broad linewidth radicals, the DNP process is more efficient when protonated solvents are used, while the presence of deuterons in the glassing matrix results in a slower DNP dynamics. Surprisingly, under these field and temperature conditions, TEMPOL outperforms trityl OX063 as a polarizing agent. At a slightly higher temperature of 1.5 K, the dependence of the TEMPOL samples DNP properties on the degree of solvent deuteration is markedly reduced. The observed behavior suggests that with both radicals ^6Li DNP is not taking place *via* thermal mixing alone, and that cross effect is most likely playing a role.

6 Probing renal pH and aminopeptidase N activity using hyperpolarized L-[1-¹³C]alaninamide

Adapted from:

Probing renal pH and aminopeptidase N activity using hyperpolarized L-[1-¹³C]alaninamide
Radaelli A, Hata R, Sando S, Bonny O, Comment A, Grütter R, Yoshihara HAI
Manuscript in preparation.

My contribution consisted in synthesizing alaninamide, performing experiments and analyzing data. HAIY derived the expression for the equilibrium constant of the carbamate formation reaction K_{eq} . The interpretation of the data has been done by myself in collaboration with the co-authors.

Abstract

L-[1- ^{13}C]alaninamide is efficiently hydrolyzed by aminopeptidase N (APN), an enzyme that plays a role in tumor angiogenesis. With an ammonium pK_a of 7.9, alaninamide also shows sensitivity to changes in physiological pH. The present study aimed at characterizing the *in vivo* renal uptake of alaninamide, particularly its sensitivity to APN activity and local variations in pH. Once infused, hyperpolarized alaninamide was observed to be readily hydrolyzed to alanine in the kidney, indicating APN activity. Three other major spectral peaks were also observed and assigned to three anatomical compartments of different pH. The disposition of alaninamide was further investigated by perturbing pH homeostasis with acetazolamide treatment, flow-sensitive *in vivo* ^{13}C NMR, and *ex vivo* NMR experiments with blood. These studies revealed that the three compartments represented both the intra- and extracellular blood pools and also one or more tubular compartments. In addition to APN and pH sensitivity, alaninamide was also found to probe dissolved CO_2 by the reaction of its free amine to form a carbamate. This study demonstrates the potential of multifunctional hyperpolarized ^{13}C probes to sense both enzyme activity and multiple physiological parameters simultaneously.

Introduction

Aminopeptidase N

Aminopeptidase N (APN)¹²⁹ is a membrane-bound enzyme abundantly found in the small-intestine and the kidney of mammals. APN catalyzes the hydrolysis of peptides and proteins releasing the N-terminal amino acid residue. It plays several physiological roles, and, because of its involvement in tumor angiogenesis, it has been recognized as a tumor biomarker.^{130;131} NMR is a good technique to monitor its enzymatic activity *in vivo*,¹³² given that the opacity of biological samples renders the use of fluorescent and luminescent probes challenging. Recently, Hata *et al.*¹³³ demonstrated that alaninamide, a derivative of alanine, presents high selectivity for APN. After being hyperpolarized *via* dissolution dynamic nuclear polarization, L-[1-¹³C]alaninamide was infused in a mouse kidney homogenate and production of alanine was observed only when APN was not inhibited. The efficiency of the compound as an APN probe, however, was not tested *in vivo*.

Role of the kidney in pH regulation

Together with blood and lungs, the kidney plays an important role in maintaining the acid-base balance in the body. In this regard, its main functions are that of excreting non-volatile acids and keeping the luminal bicarbonate concentration at a level suitable for buffering those acids before their excretion. Therefore, by modulating the amounts of secreted H⁺ and re-absorbed HCO₃⁻, the kidney also regulates their concentrations in blood. As a matter of fact, the vast majority of secreted protons is used for bicarbonate reabsorption. This process mainly takes place in the proximal convoluted tubule (with almost 90 % of bicarbonate being reabsorbed there) thanks to the presence of a Na⁺/H⁺ antiporter and that of the carbonic anhydrase (CA) enzyme. Carbonic anhydrase catalyzes the conversion of carbon dioxide to carbonic acid and bicarbonate and *vice versa*. In the kidney, CA is both located in the cytoplasm of epithelial cells of proximal tubules and bound to their apical membrane. Inhibitors of carbonic anhydrase are therefore diuretics that, by limiting the reabsorption of Na⁺ and HCO₃⁻, increase the tubular osmotic load, thus retaining water in the tubules. The limited bicarbonate reabsorption concomitantly causes a combined alkalization of urine and acidification of blood.

Secretion and reabsorption of a variety of ions along the nephron, bicarbonate above all, contributes to creating a pH gradient across the lumen.¹³⁴ Intracellular pH is instead hypothesized to be affected by the renal vascular architecture through CO₂ trapping in the medulla.¹³⁵

Measurement of renal pH

Several methods have been employed to probe renal pH. Among the more invasive ones are the use of pH microelectrodes and fluorescent probes. In the former case a measure of pH is directly obtained by positioning the electrode in the region of interest of the perfused organ; this technique was shown to be sensitive to the interstitial compartment only, as a perturbation of the intratubular pH was not reflected in the measured pH.¹³⁵ With fluorescent probes, the cells of perfused proximal tubules are loaded with a pH-sensitive dye, and their pH is obtained from the ratio of fluorescence at two suitable wavelengths.¹³⁶ MR techniques, on the other hand, have shown potential in providing less invasive measurements of pH following a pH-dependent change in the physical properties of an endogenous/exogenous agent. Three examples of such techniques involve the use of ³¹P, hyperpolarized ¹³C and gadolinium chelate contrast agents. ³¹P probes, such as inorganic phosphate, and hyperpolarized ¹³C agents, like zymonic acid, both rely on the change in chemical shift following protonation/deprotonation of a ionizable group. While the ³¹P signal inorganic phosphate mainly originates from the intracellular compartment¹³⁷, hyperpolarized zymonic acid is reportedly confined to the extracellular space.⁴² The pH-sensitivity of gadolinium chelate contrast agents, on the other hand, arises from a change in relaxivity following pH-dependent ¹H exchange with Gd³⁺-bound water. If the probe is not taken up by cells, as it is the case of for example GdDOTA-4Amp⁵⁻,¹³⁸ the pH of the renal intratubular space can be measured. With most of these techniques, a mean pH of the renal anatomical regions of cortex, medulla and calyx can be obtained. Thanks to the presence of an exchangeable proton in the amine group, the ¹³C chemical shift of alaninamide is expected to be pH dependent. Whether this pH dependence translates to a pH sensitivity *in vivo* will however depend on the pK_a of the molecule.

Carbamate formation in blood

Approximately 5% of the blood carbon dioxide content exists as dissolved CO₂. Transport of the molecule can then take place either as bicarbonate, or *via* a reaction of CO₂ with uncharged amino groups in proteins to form a carbamate¹³⁹. This process strongly depends on pH, as it depends on the balance between the concentration of non-protonated amines and that of dissolved CO₂. A widely studied example of carbamate formation in blood is that derived from the binding of CO₂ to hemoglobin. This reaction is selective for the reduced form of hemoglobin,¹⁴⁰ so that the process is thought to play a role in carbon dioxide excretion. Several techniques including ¹³C NMR^{141;142} have been used to probe carbamate formation. Apparent carbamate formation was also observed in a hyperpolarized H¹³CO₃⁻ experiments exploring the role of carbonic anhydrase in tumors.¹⁴³ There, a peak upfield with respect to bicarbonate was observed, but its origin was not investigated.

The present study aimed to characterize the behavior of hyperpolarized L-[1- ^{13}C]alaninamide *in vivo* in the rat kidney, determining whether it can be used as an APN and pH probe and assessing its distribution. For this purpose, multiple strategies were employed, including perturbation of renal pH, and localized and flow-sensitive MR methods.

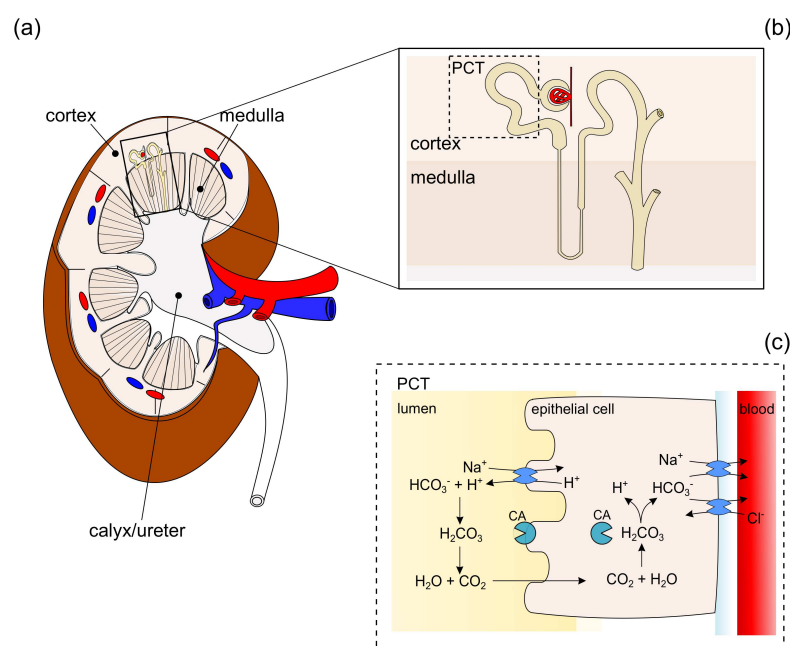


Figure 6.1 – (a) Anatomy of the kidney. (b) Structure of the nephron, the fundamental unit of the kidney. (c) Bicarbonate reabsorption in the proximal tubules is mediated by the carbonic anhydrase (CA) enzyme and makes use of secreted H^+ .

Methods

Chemicals

^{13}C -labeled alanine, ^{13}C urea and SOCl_2 were purchased from Sigma-Aldrich (Buchs, SG, CH), and unlabeled alaninamide from Bachem (Bubendorf, BL, CH). DL-[2- ^{13}C ,2- ^2H]alanine was produced by Cortecnet (Les Ulis, FR) starting from DL-[2- ^{13}C]alanine following a procedure described by Michelotti *et al.*¹⁴⁴ ^{13}C bicarbonate was purchased from CIL (Tewksbury, MA), and a 7 M solution of NH_3 in methanol from Acros Organics (Reinach, BL, CH). Finally, Dotarem was acquired from Guerbet (Roissy CdG Cedex, FR), and trityl OX063 radical from Albeda Research (Copenhagen, DK).

Alaninamide synthesis

All alaninamide · HCl salts were synthesized following a two-step procedure similar to the one described by Florini *et al.*¹⁴⁵ 1.05 equivalents of SOCl₂ were added to a solution of alanine in methanol (in a ratio of 2 mL of MeOH per 100 mg of alanine) that had been previously cooled down to approximately 0 °C in an ice bath. The reaction was left stirring at room temperature for 24 hours, and its progress was monitored *via* thin layer chromatography (TLC) - TLC plates: Silica gel 60 F₂₅₄; solvent: isobutanol/water/acetic acid in a 3:1:1 ratio; ninhydrin in MeOH solution for spotting. The solution was subsequently evaporated under vacuum at 37 °C by means of rotary evaporation, yielding alanine methyl ester · HCl. The purity of the reaction product was measured *via* ¹H NMR. Alanine methyl ester · HCl was then dissolved in an excess (about 10 mL for about 150 mg of ester) of a 7 M solution of NH₃ in MeOH, and left stirring at room temperature. The reaction was monitored *via* TLC and, once completed, the product was dried by rotary evaporation and recrystallized from methanol. The purity of the resulting alaninamide · HCl was verified *via* ¹H NMR.

Alaninamide titration

The alaninamide titration curve was determined by performing ¹³C NMR measurements on a set of 10 0.5 M L-Ala-NH₂ · HCl (enriched about 3 % at the ¹³C1 position) samples of pH ranging from 3.55 to 10.16. The pH of the samples, measured at 37 °C with a standard pH electrode, was adjusted by adding known volumes of H₂O and NaOH to the alaninamide salt. 15 mM of ¹³C urea was added to the solution as an internal reference, together with 0.3 mM of gadoteric acid as a relaxivity agent and D₂O (in an amount corresponding to 20 % of the final volume) for locking purposes. ¹³C NMR measurements were carried out at 37 °C on a 400 MHz spectrometer (Bruker Biospin, Fällanden, ZH) equipped with a standard BBFO_z coil. The acquisition parameters were set as follows: spectral width (sw) = 23980.8 Hz, acquisition time (at) = 1.37 s, number of scans (ns) = 64, dummy scans (ds) = 0, TR = 10 s, flip angle (FA) = 30°, continuous decoupling. The titration curve obtained from these measurements was then fitted to determine pK_a and chemical shift bounds in the low (δ_{A⁻}) and high (δ_{HA}) pH range using:

$$\delta_{obs} = \frac{\delta_{A^-} \cdot 10^{(pH-pK_a)} + \delta_{HA}}{1 + 10^{(pH-pK_a)}}, \quad (6.1)$$

δ_{obs} being the observed ¹³C chemical shift.

Hyperpolarization

The three alaninamide samples used in the hyperpolarized studies (L-[1-¹³C], D-[1-¹³C] and DL-[2-¹³C,2-²H]alaninamide) were prepared according to the following formulation. Alani-

namide · HCl was dissolved in 0.29 molar equivalents of a 6.7 M solution of NaOH in H₂O; 2.12 and 0.46 molar equivalents of H₂O and glycerol, respectively, were subsequently added. Finally, 25 mM of trityl OX063 radical was dissolved in the sample using a sonicating bath. The alaninamide concentration was estimated to be 4.4 M. An 8 M ¹³C urea solution in water:glycerol 50:50 (v/v) with 25 mM OX063 was also prepared to be hyperpolarized and co-injected with alaninamide in order to have a chemical shift reference *in vivo*. Frozen droplets of the preparations were placed into a polytetrafluoroethylene sample cup, in amounts varying according to the experiment to be performed:

- polarization measurements: 22.8 μ L of L-[1-¹³C]alaninamide
- *in vivo* and *ex vivo* MRS experiments: either 8 μ L of L-[1-¹³C] or D-[1-¹³C]alaninamide, or 10 μ L of DL-[2-¹³C]alaninamide, each with 1 μ L of ¹³C urea
- flow-suppressed MRS experiments: 24 μ L of L-[1-¹³C]alaninamide and 3 μ L of ¹³C urea
- 2D-chemical shift imaging (CSI) experiment: 60 μ L of L-[1-¹³C]alaninamide and 20 μ L of ¹³C urea.

The sample cup was then loaded in a custom-built 7 T polarizer⁷¹ operating at 1 K. The optimal microwave frequency and power for DNP at these conditions were determined to be 196.59 GHz and 50 mW, respectively. The sample was hyperpolarized for approximately two hours, after which it was rapidly dissolved in 5.5 mL of a 1:1 (v/v) phosphate buffer:saline solution (pH 7.4).

Polarization measurements

The L-[1-¹³C]alaninamide polarization level was measured post dissolution and transfer (~ 3 s) in a separator-infusion pump. The pump was equipped with ¹³C and ¹H single-loop coils and was located at the isocenter of a 9.4 T/31 cm horizontal bore magnet (Magnex Scientific, Oxford, UK) equipped with a VNMRs console (Varian, Palo Alto, CA). The ¹³C hyperpolarized signal was monitored by applying 5° flip angle hard pulses every 3 s. Once the signal had completely decayed, 5 μ L of a 0.5 M gadoteric acid solution was added. The thermal signal was then measured by averaging 1024 acquisitions with a repetition time of 5 s and the same rf-pulse parameters. The enhancement was calculated as the ratio between hyperpolarized and thermal signal. The experiments were repeated twice.

Animals

All animal experiments were conducted according to federal and local ethical guidelines, and the protocols were approved by the local regulatory body of the Canton de Vaud, Switzerland.

Chapter 6. Probing renal pH and aminopeptidase N activity using hyperpolarized L-[1-¹³C]alaninamide

Male Sprague Dawley rats (250-300 g) were anesthetized using 5% isoflurane in 50% oxygen, and maintained at 1-2% isoflurane for the remainder of the experiment. The hyperpolarized solution was administered through a catheter placed in the femoral vein. Cannulation of the two femoral arteries was performed to monitor blood pressure and to allow for blood sampling. Blood gases, pH and physiological parameters were measured shortly after each infusion using an EPOC blood analysis system (Siemens Healthcare GmbH, Erlangen, DE). The kidney pH of the rats was perturbed by administering IV, one hour prior to the hyperpolarized infusion, an aqueous solution of acetazolamide (ACZ) at a dose of 20 mg/kg. Control experiments where acetazolamide was replaced with saline were performed on three animals. In this particular case, three hyperpolarized infusions were delivered to each animal, and a PBS bolus was injected one hour prior to the second one at a dose of 1 μ L/g body weight. In both cases, following drug administration, urine was collected to determine its effect up to 20 min before the hyperpolarized experiment.

In vivo hyperpolarized ¹³C MRS/I

Experiments were performed on the 9.4 T/ 31 cm horizontal bore magnet described in Section 6.2.5. A 10-mm-diameter single loop ¹H and a pair of 10-mm-diameter ¹³C surface coils operating in quadrature mode were placed over the organ of interest. Anatomical images were acquired to ensure the correct positioning of the coil with respect to the probed tissue. Localized and unlocalized shimming on the water resonance were performed to improve the spectral linewidth. Following dissolution and transfer, 1.4 mL of the hyperpolarized solution was infused in the animal over \sim 9 s using a setup previously described.⁷¹

¹³C MRS

Kidney experiments

¹H-decoupled ¹³C FIDs (sw = 20 kHz, at = 0.204 s, WALTZ-16 decoupling modulation) were acquired over the left kidney by applying 30° BIR4 pulses approximately every 2.9 s after infusion of hyperpolarized L-[1-¹³C]alaninamide. The acquisition was respiration-gated and cardiac-triggered. The experiments were repeated at baseline conditions and after acetazolamide treatment on $n = 5$ animals. In all spectra, the chemical shift was referenced to ¹³C urea at 165.48 ppm.¹⁴⁶ The collected spectra were fitted with Bayes (Washington University, St. Louis) to determine amplitude and area-under-the-curve (AUC) ratios with respect to the total carbon signal of each peak. By replacing in Eq. 6.1 the measured chemical shift, pK_a and 1-¹³C upper and lower chemical shift bounds, a time-dependent pH value was derived for each alaninamide spectral compartment. A mean compartment pH value was then obtained by averaging over acquisitions within one experiment, and subsequently averaging

over experiments. The statistical difference between the pH values before and after acetazolamide treatment was assessed by using a paired Student's *t*-test with Bonferroni correction for multiple comparisons. A corrected *p*-value equal to or below 0.05 was considered statistically significant. In control experiments, pH values of the compartments were compared across infusions using a one-way ANOVA test.

All experimental values are expressed as mean \pm S.D., and in all tests significance was attributed according to: * $p < 0.05$, ** $p < 0.01$, and *** $p < 0.001$.

Besides pH, the ratio of carbamate (produced from alaninamide) to total carbon signal was also evaluated as a function of time and as an averaged value over consecutive acquisitions. Assuming an equilibrium state for carbamate formation and decomposition, the equilibrium constant K_{eq} of the carbamate formation reaction was derived from the acid dissociation constant of alaninamide, blood pH and CO₂ concentration:

$$\frac{[\text{carbamate}]}{[\text{alaninamide}]} = K_{eq} \cdot \frac{10^{-\text{p}K_a} [\text{CO}_2]}{10^{-\text{pH}} + 10^{-\text{p}K_a}}. \quad (6.2)$$

This equation was used to fit the carbamate-to-total carbon signal ratio measured in the second scan as a function of two independent values: alaninamide compartment 1 pH and blood pCO₂.

Finally, hyperpolarized D-[1-¹³C]alaninamide was administered to $n = 1$ animal, and its uptake was investigated following the same protocol described above.

Heart experiments

Hyperpolarized L-[1-¹³C]alaninamide was infused in one animal and its uptake was monitored at baseline conditions using the same acquisition parameters and post-processing work-flow as for the kidney. Additionally, a second experiment was carried out after the infusion of hyperpolarized DL-[2-¹³C,2-²H]alaninamide. In this case the repetition time between consecutive scans was set to 0.9 s, while all other parameters were kept the same as for the L-experiment.

¹³C flow-suppressed MRS

An interleaved pulse-acquire (excite: BIR4 pulse, FA = 30°)/ double spin-echo (excite: BIR4 pulse, FA = 30°; refocus: hyperbolic secant HS180 pulse, R = 16) sequence (Figure 6.2) was developed to detect the ¹³C signal without and with flow attenuation, respectively. Flow suppression was achieved by adding four pairs of bipolar gradient pulses along all three directions of space after the rf-pulses in the double spin-echo acquisitions.

Chapter 6. Probing renal pH and aminopeptidase N activity using hyperpolarized L-[1-¹³C]alaninamide

The bandwidth of the BIR4 and HS rf-pulses was tested on a ¹³C urea phantom positioned at a distance from the coil of 5 mm, which is comparable to the coil-to-kidney gap in the *in vivo* experiments. The expected effects of flow suppression and diffusion were simulated in Matlab (R2017a, Mathworks, Natick, MA) using a model described in Gordon *et al.*¹⁴⁷ Briefly, the signal attenuation caused by bipolar gradient pulses on moving spins (assuming the flow to be laminar) can be approximated by: $S(\Delta v) = S_0 \left\| \text{sinc} \left(\gamma m_1 \frac{\Delta v}{2} \right) \right\|$, with Δv the spread in intravoxel velocities and m_1 the gradient first moment. The phase dispersion induced on diffusing spins is instead described by $S(D) = \exp(-bD)$, D being the diffusion coefficient and b the gradient b -value. Using these two equations, one can estimate the relative signal loss as a function of the gradient parameters and velocity and diffusivity of the spins.

The gradient parameters were optimized in phantom experiments starting from the simulation results. The efficiency of flow suppression on moving ¹³C spins was tested using two phantoms: a syringe containing ethanol, and a tube filled with methanol running parallel to the direction of the \mathbf{B}_0 field through which the fluid was pushed by a syringe. The methanol velocity was varied between 1.3 and 18.5 mm/s. The optimal gradient parameters were found to be: peak gradient amplitude $G_{x,y,z} = 300$ mT/m ($G_{\text{TOT}} = 520$ mT/m), gradient duration $T = \delta + \xi = 3$ ms, ramp duration $\xi = 0.46$ ms. For such parameters, the b -value, given by:

$$b = n_G \gamma^2 G^2 \left(\frac{2\delta^3}{3} + \delta^2 \xi + \frac{\xi^3}{30} - \frac{\xi^2 \delta}{6} \right) \quad (6.3)$$

with n_G the number of gradient pairs, was 78.4 s/mm². Finally, the echo time TE was optimized to avoid eddy current artifacts.

Hyperpolarized experiments were performed on $n = 3$ animals. Each animal received three identical injections of hyperpolarized L-[1-¹³C]alaninamide. In order to minimize incomplete refocusing, the animal was positioned so that the kidney and the coil would be as close as possible. ¹H-decoupled ¹³C FIDs (sw= 20 kHz, at= 0.204 s, WALTZ-16 decoupling modulation) were collected approximately every 2.9 s using one of the following acquisition schemes: pulse-acquire interleaved with double spin-echo with bipolar gradients, as shown in Figure 6.2(a); the same pulse-acquire interleaved with the double spin-echo, but with the gradient levels set to 0, to assess the effect of dephasing caused by motion and T₂ relaxation during the echo time (TE) (Figure 6.2(b)); an acquisition with interleaved double spin-echo with and without gradients to discern the effect of the gradients from that of TE (Figure 6.2(c)). The order of the three acquisitions was randomized, and every acquisition was respiration-gated and cardiac-triggered. The spectra were fitted using Bayes and, because of the incomplete spectral resolution between alanine and alaninamide compartment 1, metabolite ratios were calculated with respect to the sum of the two.

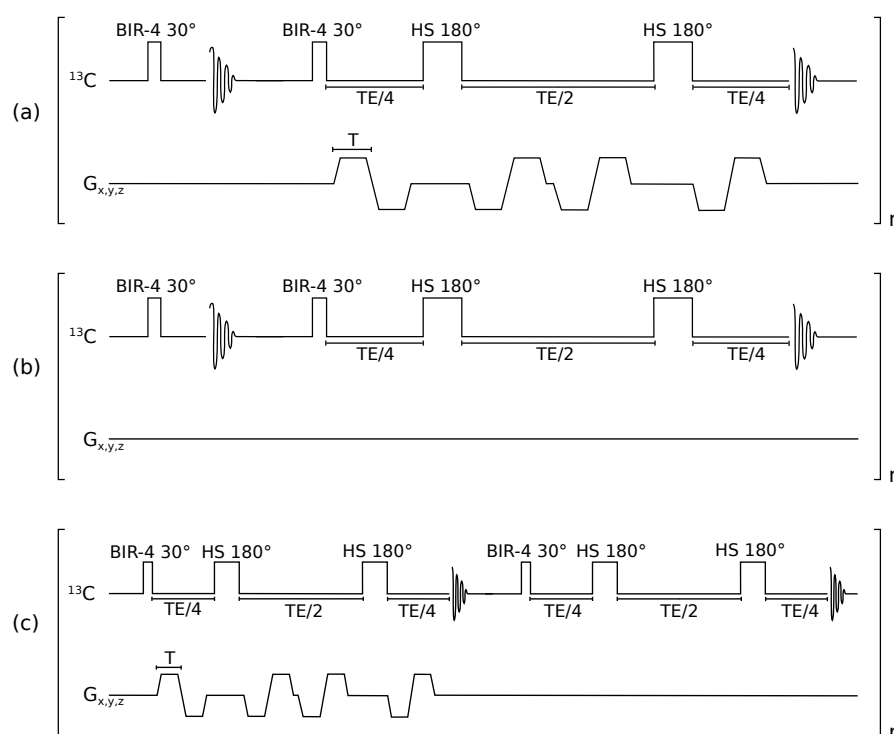


Figure 6.2 – Acquisition schemes implemented to discern the mobility of the alaninamide compartments. Four pairs of bipolar gradients ($b = 78.4 \text{ mm/s}^2$) are added in the double spin-echo acquisition to achieve flow suppression.

^{13}C chemical shift imaging

^{13}C imaging experiments were performed using a FID-CSI sequence. Preliminary testing of the sequence was done using hyperpolarized pyruvate, and the results are shown in Appendix D. After infusion of hyperpolarized alaninamide, the signal was acquired over the right kidney of the animal from a 5 mm-thick coronal slice with a field-of-view (FOV) of $30 \times 30 \text{ mm}^2$, 8×8 matrix (corresponding to an in-plane resolution of 3.75 mm) using a centric \mathbf{k} -space encoding pattern. Data acquisition was started 13 s after delivery of the hyperpolarized bolus, with the following parameters: 10° nominal FA, 3005 Hz spectral bandwidth, 512 points, 170.39 ms acquisition time, 172.18 ms repetition time. The total scan time was 11.9 s. Data were post-processed in SIVIC¹⁴⁸ and Matlab. The raw FIDs were Hamming-filtered, apodized with a 9 Hz exponential function, and zero-filled by a factor of 2 in both spectral and spatial dimensions prior to being Fourier-transformed. Metabolite maps were generated for the three alaninamide compartments, alanine and urea.

An anatomical ^1H reference image was acquired using a standard gradient spin-echo sequence (parameters: $30 \times 30 \text{ mm}^2$ FOV, 64×64 matrix, 2 mm thick coronal slice, $\text{TR}/\text{TE} = 37.63/2.03 \text{ ms}$, 60° nominal flip angle).

Chapter 6. Probing renal pH and aminopeptidase N activity using hyperpolarized L-[1-¹³C]alaninamide

Ex vivo hyperpolarized ¹³C MRS

0.5 mL of the hyperpolarized L-[1-¹³C]alaninamide was infused over ~ 9 s into a 10 mm NMR tube containing 2 mL of freshly collected rat blood with heparin added (10 U per mL of blood). The temperature was kept at 37 °C for the duration of the experiment using a temperature control unit and a water bath. The ¹³C signal was acquired using a three-turn ¹³C, single loop ¹H coil placed around the tube. ¹H-decoupled ¹³C FIDs (sw = 20 kHz, at = 1 s, WALTZ-16 decoupling modulation) were collected every 3 s by applying a 5° hard pulse. Because of the broad linewidth of the experiments, a good fit of the peaks could not be obtained, so the resonances were integrated after the FIDs were apodized with an exponential function of constant 8 Hz, and ratios to the total carbon signal were calculated. The pH was estimated from the chemical shift using the same procedure described in Section 6.2.7.

Carbamate characterization

Ex vivo ¹³C NMR

Two solutions, of 200 mM L-[1-¹³C]alaninamide · HCl and 605 mM ¹³C urea, respectively in D₂O were prepared. 30 μL aliquots of the former and 5 μL of the latter were added in a 5 mM NMR tube previously loaded with 520 μL of freshly-collected blood and 60 μL of D₂O. ¹³C NMR measurements were then performed at 37 °C on a 600 MHz vertical Bruker scanner equipped with a cryoprobe (CPBPBBO_z). The acquisition was started approximately 3 min after substrate addition with the following parameters: sw = 36231.88 Hz, at = 0.904 s, ns = 24, ds = 0, FA = 30°, TR = 30 s, inverse-gated decoupling.

The same sample was prepared with L-[3-¹³C]alaninamide · HCl. In this case, starting from 90 s and up to 2 min after substrate addition (comparable to the timescale of the *in vivo* experiment), a ¹³C NMR spectrum was acquired every 11 s (acquisition parameters: sw = 36231.88 Hz, at = 0.904 s, ns = 4, ds = 0, FA = 30°, TR = 1.8 s, inverse-gated decoupling). The number of scans was then increased to 100 for the following 4 acquisitions. After having apodized the FIDs with a 0.3 Hz exponential function, integrals of the peaks were calculated.

Carbamate formation

10 mM L-[1-¹³C]alaninamide · HCl, 100 mM NaH¹³CO₃⁻ and 5 mM ¹³C urea were added to D₂O. The pH of the solution was measured to be 8. Carbamate formation was then monitored *via* ¹³C NMR at 37 °C on the same 400 MHz scanner used for the alaninamide characterization. Acquisition parameters: sw = 36231.88 Hz, at = 0.904 s, ns = 80, ds = 0, FA = 30°, TR = 30 s, inverse gated decoupling. The same experiment was repeated with DL-[2-¹³C]alaninamide · HCl to confirm the carbons' assignment.

Results

Alaninamide characterization

Representative ^1H NMR spectra of L-[1- ^{13}C]alaninamide methyl ester \cdot HCl and L-[1- ^{13}C]alaninamide \cdot HCl are reported in Appendix B.

The dependence of the alaninamide ^{13}C chemical shift on pH caused by the protonation and deprotonation of the amine was investigated, and the result is shown in Figure 6.3 for the C1 carbon. At 37 °C the pK_a of alaninamide was 7.9, and the ^{13}C chemical shift dispersion of C1 8.4 ppm.

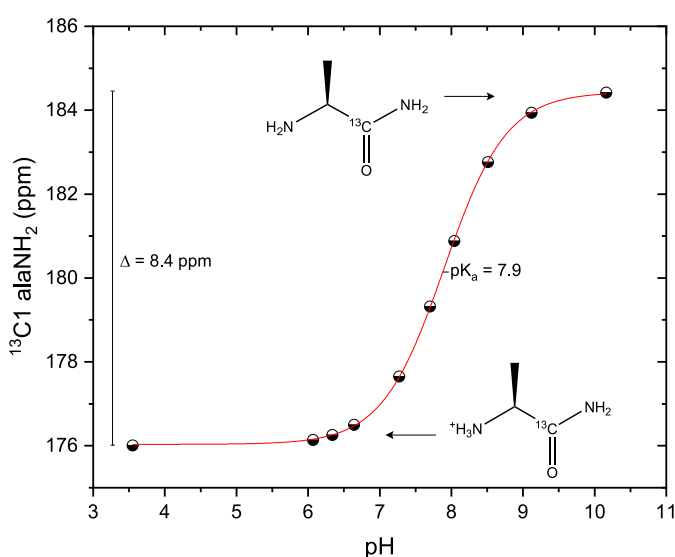


Figure 6.3 – L-[1- ^{13}C]alaninamide titration curve at 37 °C, 9.4 T.

The L-[1- ^{13}C]alaninamide polarization level in the scanner was measured to be 30.5 ± 3.0 %, and the liquid-state $T_{1\rho}$ in the dissolution medium 25.2 ± 0.1 s.

In vivo hyperpolarized ^{13}C MRS/I

^{13}C MRS

Kidney experiments

The spectral timecourse of hyperpolarized L-[1- ^{13}C]alaninamide in the kidney, shown in Figure 6.4, presented three interesting features. Firstly, the main alaninamide peak was split into three spectral components, whose weight relative to each other changed with time. These peaks were assigned to three compartments of different pH within the kidney. Using the information gathered from the titration curve, a mean pH value was evaluated for each com-

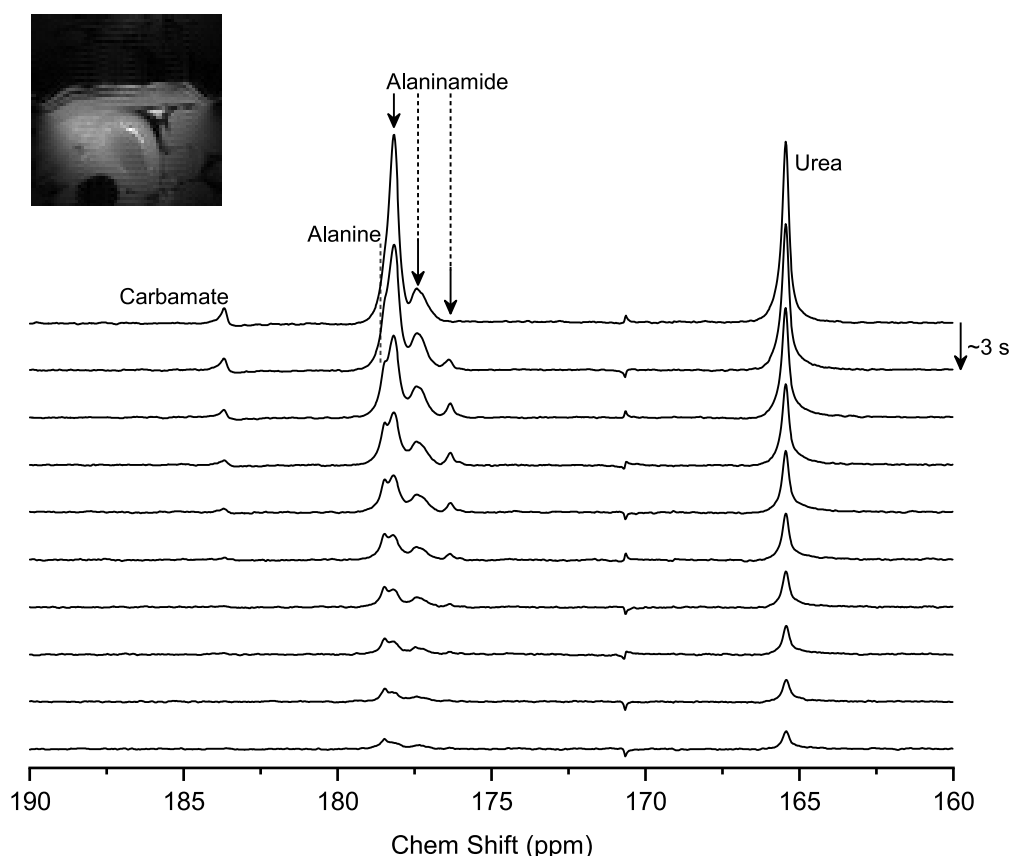


Figure 6.4 – Representative stack of spectra acquired in the rat kidney after a bolus injection of hyperpolarized L-[1-¹³C]alaninamide and ¹³C urea. The main alaninamide peak is observed to be split into three spectral compartments (at a chemical shift of 178.15 ppm, 177.42 ppm and 176.37 ppm, respectively) whose relative amplitudes change in time. Alanine and carbamate production is observed at 178.48 ppm and 183.67 ppm, respectively.

partment: 7.46 ± 0.02 for compartment 1, corresponding to 178.46 ppm; 7.21 ± 0.02 for compartment 2 at 177.21 ppm; and 6.58 ± 0.05 for compartment 3 at 176.42 ppm. Globally, the AUC ratio to the total carbon signal of compartments 1 and 2 was found to be higher than that of compartment 3. Secondly, alanine production was observed, with the building up of a shoulder peak at 178.48 ppm next to alaninamide compartment 1. Finally, a small peak was consistently detected at 183.67 ppm. This peak, that appeared from the first scan alongside the bolus, was later assigned to carbamate originating from the reaction of alaninamide with blood CO₂ (see Section 6.3.3 for details).

The kidney pH was then perturbed by administering acetazolamide to the rats prior to the hyperpolarized infusion. Measurements of urine and blood pH confirmed the expected effect of the drug, with acidification of blood and alkalization of urine. In particular, at the time of the hyperpolarized infusion, the pH in blood had decreased on average by 0.07 units down

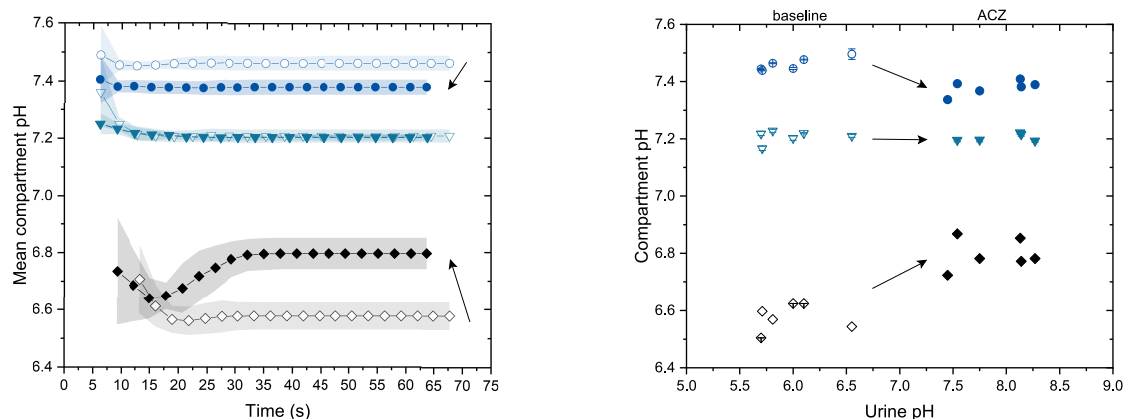


Figure 6.5 – Left: Time dependence of the pH values of the three alaninamide compartments before and after acetazolamide treatment. The curves were obtained by averaging the pH values measured across the different experiments, and are displayed with their standard deviation (shadowed area). Right: Compartments pH *vs* urine pH. Here each symbol represents an individual experiment. In both figures, empty symbols represent baseline condition, and full symbols post acetazolamide treatment. Different symbol shapes and colors are used to distinguish the three compartments.

to 7.29 ± 0.03 , whereas that of urine had increased from 5.98 ± 0.32 to 7.88 ± 0.35 . The blood and kidney pH perturbation was also reflected in the outcome of the hyperpolarized alaninamide experiment. The pH value of compartment 1 decreased to 7.38 ± 0.03 , while that of compartment 2 did not change, and that of compartment 3 increased to 6.80 ± 0.05 following a peculiar time dependence. Finally, the AUC ratio of compartment 1 and 3 increased following ACZ treatment, while that of compartment 2 slightly decreased. These results are shown in Figure 6.5.

Paired Student's *t*-tests with Bonferroni correction for multiple comparisons confirmed that the pH variation before and after treatment was significant for compartment 1 ($p = 0.0057$), 3 ($p = 0.00141$) and for blood ($p = 0.0006$) (Figure 6.6). On the other hand, only the AUC ratio of compartment 3 significantly increased following treatment ($p = 0.039$) (Figure 6.7). A strong linear correlation between blood pH and compartment 1 pH was observed (Pearson's $R = 0.93$). Blood pH measures made with the EPOC system (used for the *ex vivo* measurements) were compared to those done with a standard electrode pH probe (used for the titration calibration). On the same sample, the pH measurements with the two setups differed by approximately 0.1 pH units, matching the difference observed *in vivo* between compartment 1 and the blood pH.

Finally, no change in compartment pH and AUC was observed after saline infusion (data not shown).

Chapter 6. Probing renal pH and aminopeptidase N activity using hyperpolarized L-[1-¹³C]alaninamide

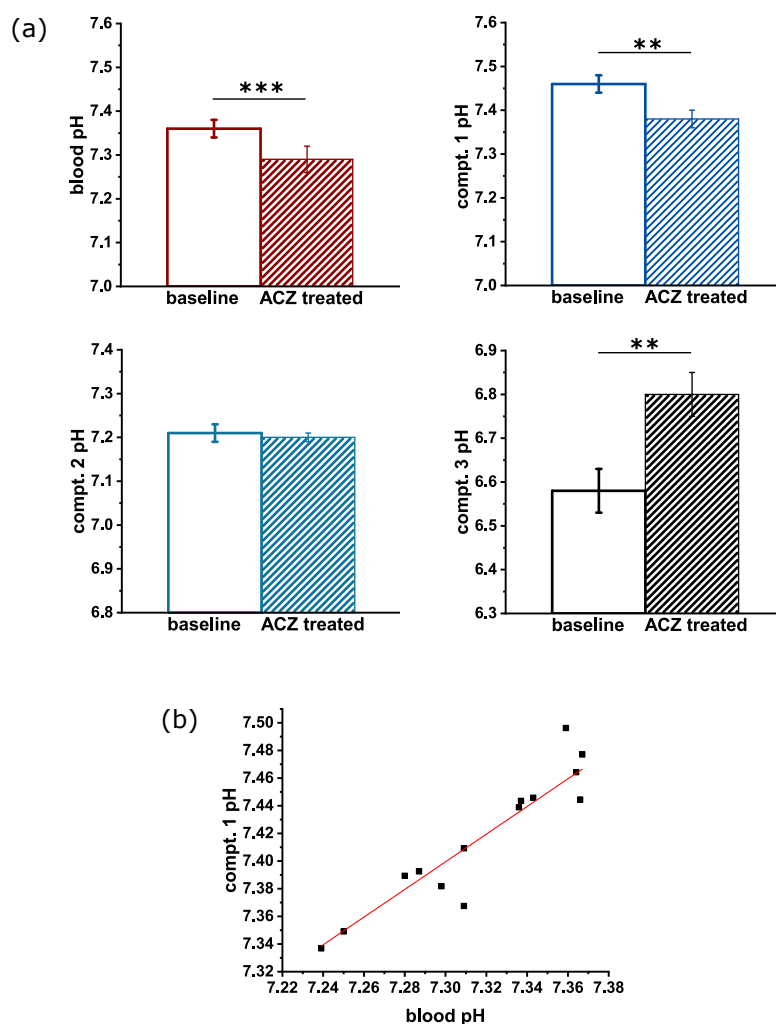


Figure 6.6 – (a) Mean blood and alaninamide compartments pH values \pm S.D. before and after acetazolamide treatment. The asterisks indicate the significance in the difference between the two states. (b) Linear correlation between blood and compartment 1 pH (Pearson's $R=0.93$).

As reference, a comparison between renal uptake and metabolism of the two alaninamide enantiomers is shown in Figure 6.8. Unlike L-alaninamide, production of alanine was not observed following a bolus of D-alaninamide.

Heart experiments

Experiments scanning the heart were performed to gain insights on the origin of the metabolite at 183.67 ppm, as well as obtain additional information on the compartmentalization of alaninamide. The heart's higher blood volume provides a way to distinguish the blood compartment *in vivo*.

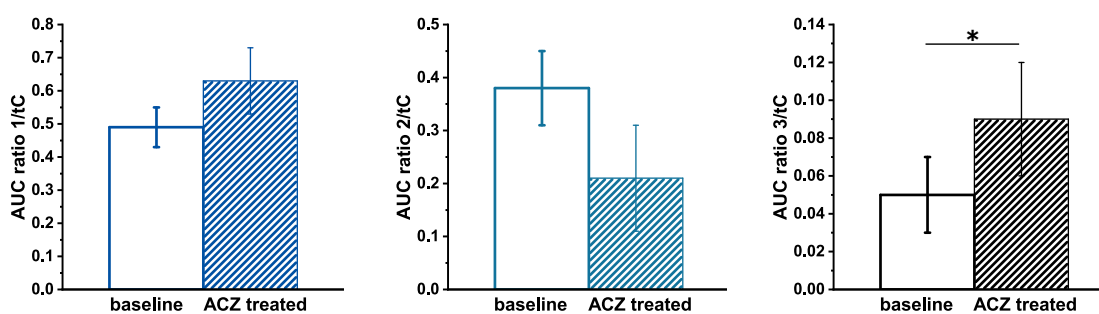


Figure 6.7 – Mean AUC ratios \pm S.D. before and after acetazolamide treatment of the three alaninamide compartments.

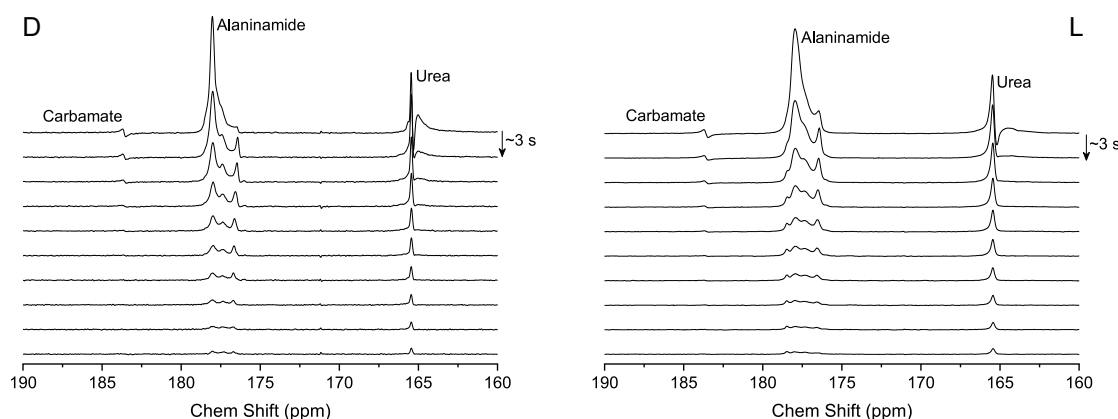


Figure 6.8 – Comparison of two representative stacks of spectra acquired in the rat kidney after a bolus injection of D- (left) and L-[1- ^{13}C]alaninamide (right). Both acquisitions were performed following acetazolamide treatment.

- L-[1- ^{13}C]alaninamide infusion

Only two alaninamide compartments were observed scanning the heart, as Figure 6.9 shows. Again, the pH of compartment 1 was found to correlate well with the blood pH measured with the EPOC system. Moreover, the kinetic profile of the ratio of compartment 2 to the total carbon signal was observed to be fairly similar to that measured in the kidney (Figure 6.10). Finally, the species at 183.67 ppm was also detected, and as for the kidney appeared directly from the first scan.

- DL-[2- ^{13}C ,2- ^2H]alaninamide

Hyperpolarized DL-[2- ^{13}C ,2- ^2H]alaninamide was infused and its uptake monitored in the heart to confirm the assignment of the species observed at 183.67 ppm with the 1- ^{13}C -labeled molecule. One of the initial hypotheses being that the species at 183.67 ppm is lactamide, the

Chapter 6. Probing renal pH and aminopeptidase N activity using hyperpolarized L-[1-¹³C]alaninamide

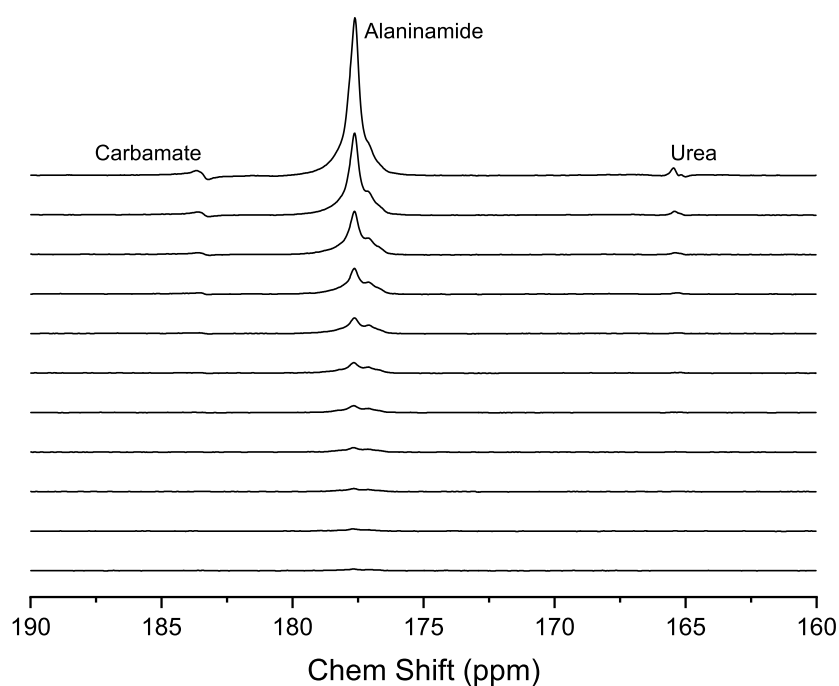


Figure 6.9 – Spectral timecourse of hyperpolarized L-[1-¹³C]alaninamide in the heart.

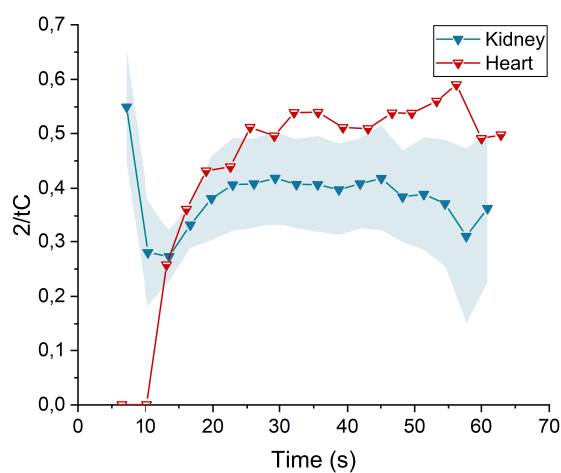


Figure 6.10 – Comparison of the kinetic profiles of the ratios of alaninamide compartment 2 to the total carbon signal in the kidney and heart. The shaded area represents the standard deviation of the curve.

timecourse of spectra acquired in the heart in Figure 6.11 is shown together with a ¹³C high-resolution spectrum of lactamide in D₂O. *In vivo*, with the main alaninamide peak at 51.66 ppm, a shoulder at 53.54 ppm was observed in all scans but the first one.

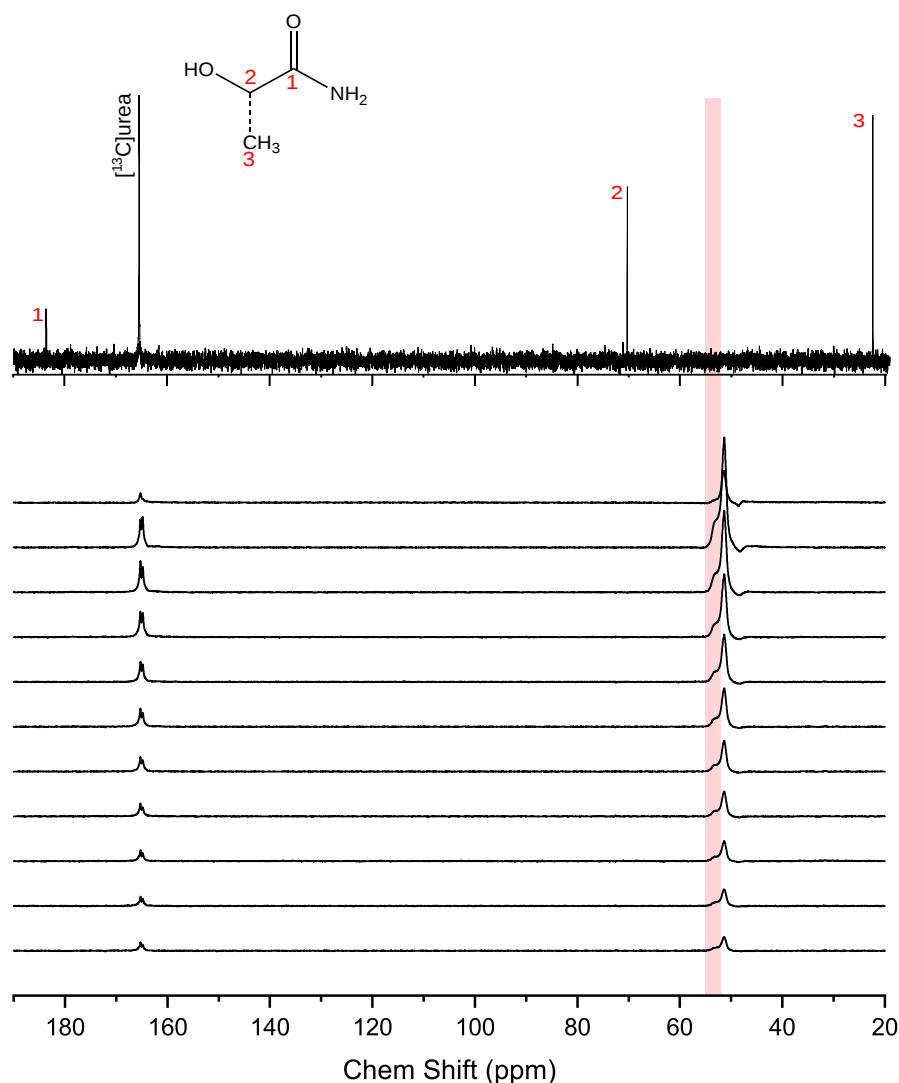


Figure 6.11 – Bottom: spectral timecourse of hyperpolarized DL-[2- ^{13}C ,2- ^2H]alaninamide in the heart. Top: ^{13}C spectrum of lactamide in D_2O acquired at 37 °C, 9.4 T. While the lactamide $^{13}\text{C}_1$ chemical shift exactly matches the one of the extra species observed *in vivo*, the $^{13}\text{C}_2$ chemical shifts of the two species are quite different.

^{13}C flow-suppressed MRS

Hyperpolarized experiments with flow suppression were performed to assess the mobility of the three alaninamide compartments.

Simulations provided an estimate of the signal level variation with gradient duration T and spin velocity v . As Figure 6.12(b) shows, the four pairs of gradient pulses are expected to almost completely dephase spins moving at velocities above 2.5 mm/s, leaving a low residual signal. Below 2.5 mm/s, the signal loss induced by the gradients is only partial and strongly

Chapter 6. Probing renal pH and aminopeptidase N activity using hyperpolarized L-[1-¹³C]alaninamide

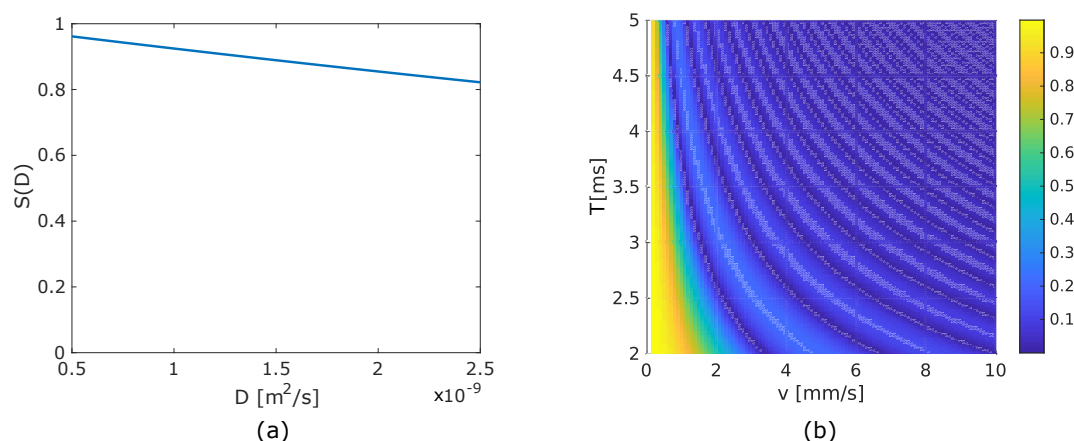


Figure 6.12 – (a) Expected diffusion signal loss following a train of four pairs of bipolar gradient lobes as a function of the diffusion coefficient D . (b) Heat map simulating the effect of the gradients on the signal of moving spins for different gradient durations T and flow velocities v .

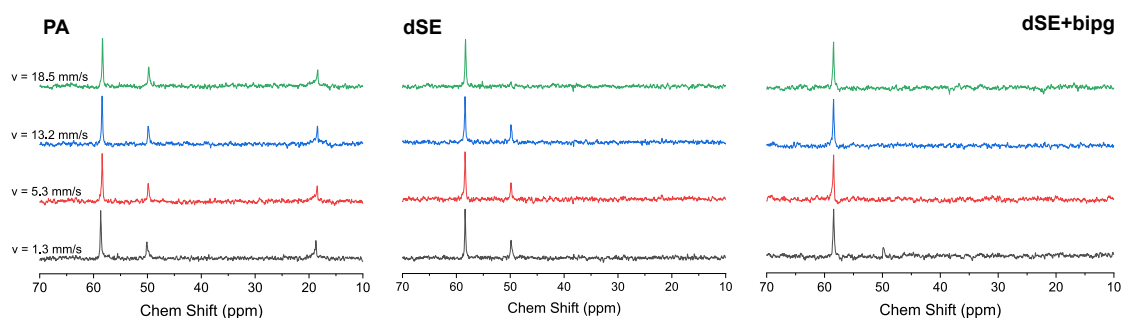


Figure 6.13 – Phantom experiments showing the effect of bipolar gradients (dSE+bipg) and that of the TE delay and refocusing pulses (dSE) on static (ethanol, 58.30 and 18.35 ppm) and moving (methanol, 49.75 ppm) ¹³C spins at multiple flow velocities. The upfield ethanol peak disappears in the double spin-echo acquisitions as its resonance frequency lies outside the bandwidth of the refocusing pulse.

dependent on T . A gradient duration of 3 ms was chosen as a compromise between an efficient vascular suppression and signal loss due to diffusion of static spins and T_2 relaxation. For such gradient width, a signal decrease up to almost 20 % for spins with a diffusion coefficient of $2.5 \cdot 10^{-9} \text{ m}^2/\text{s}$ can be expected (Figure 6.12(a)).

In vitro phantom studies confirmed the effect of bipolar gradient pairs and TE delay on ¹³C static and flowing spins at several velocities, as shown in Figure 6.13. Here, the ethanol peaks at 58.30 and 18.35 ppm represent the stationary phase, and the methanol signal at 49.75 ppm the moving one. In the double spin-echo with bipolar gradients acquisition, a reduction in methanol signal intensity was already observed at velocity of 1.3 mm/s. At all higher probed velocities, the methanol signal was completely suppressed. The α -carbon of ethanol was left

unaltered by the gradients, while the β - one disappeared in the double spin-echo acquisitions as its frequency lies outside the bandwidth of the refocusing pulse. With the gradient levels set to zero, the double spin-echo appeared to perform similarly to the pulse-acquire, with the difference that at $\nu = 18.5$ mm/s the TE delay was found to be sufficiently long for moving spins to completely dephase.

Having established the performance of acquisition scheme and parameters, flow suppression experiments were carried out *in vivo*. Figure 6.14 shows the trend of the metabolite ratios to the sum of compartment 1 and alanine over time for a representative experiment. The time-courses of metabolite ratios for the remaining two experiments are shown in Appendix B. A decrease in the ratios of compartments 1 and 2 was consistently observed in all three experiments when comparing pulse-acquire and double spin-echo acquisitions. This decrease was stronger when the bipolar gradients were turned on. Conversely, with compartment 3 no difference between acquisition schemes was observed, while alanine displayed the opposite behavior, as its ratio increased when the bipolar gradients were applied. When comparing the double spin-echo scans with and without gradient pairs, a clear and consistent trend over experiments was not observed.

¹³C chemical shift imaging

The hyperpolarized ¹³C CSI maps of alaninamide, alanine and urea are displayed in Figure 6.15. For all metabolites, the signal is clearly observed in the kidney. To improve the visualization of the distribution differences between alaninamide compartments, a map of the ratio between intensities of compartment 1 and 3 is shown in Figure 6.16. Here, it can be more easily seen that when compared against compartment 1, compartment 3 is more widely distributed in the calyx.

Carbamate characterization and alaninamide in blood cells

Ex vivo ¹³C NMR

In order to determine whether the alaninamide product at 183.67 ppm originated from there, alaninamide was mixed with blood and ¹³C NMR experiments were performed. The ¹³C spectrum of L-[1-¹³C]alaninamide is shown in Figure 6.17(a). On a timescale of a few minutes, alaninamide uptake in the intracellular compartment was observed, with the appearance of a second broader peak upfield with respect to the main alaninamide peak. The chemical shift separation between the two compartments was $\Delta\delta = 0.62$ ppm. Alanine and the product at 183.67 ppm were also detected. Figure 6.17(b) displays instead the ¹³C spectrum of L-[3-¹³C]alaninamide in blood. Here, 100 s following mixing, intracellular uptake of alaninamide

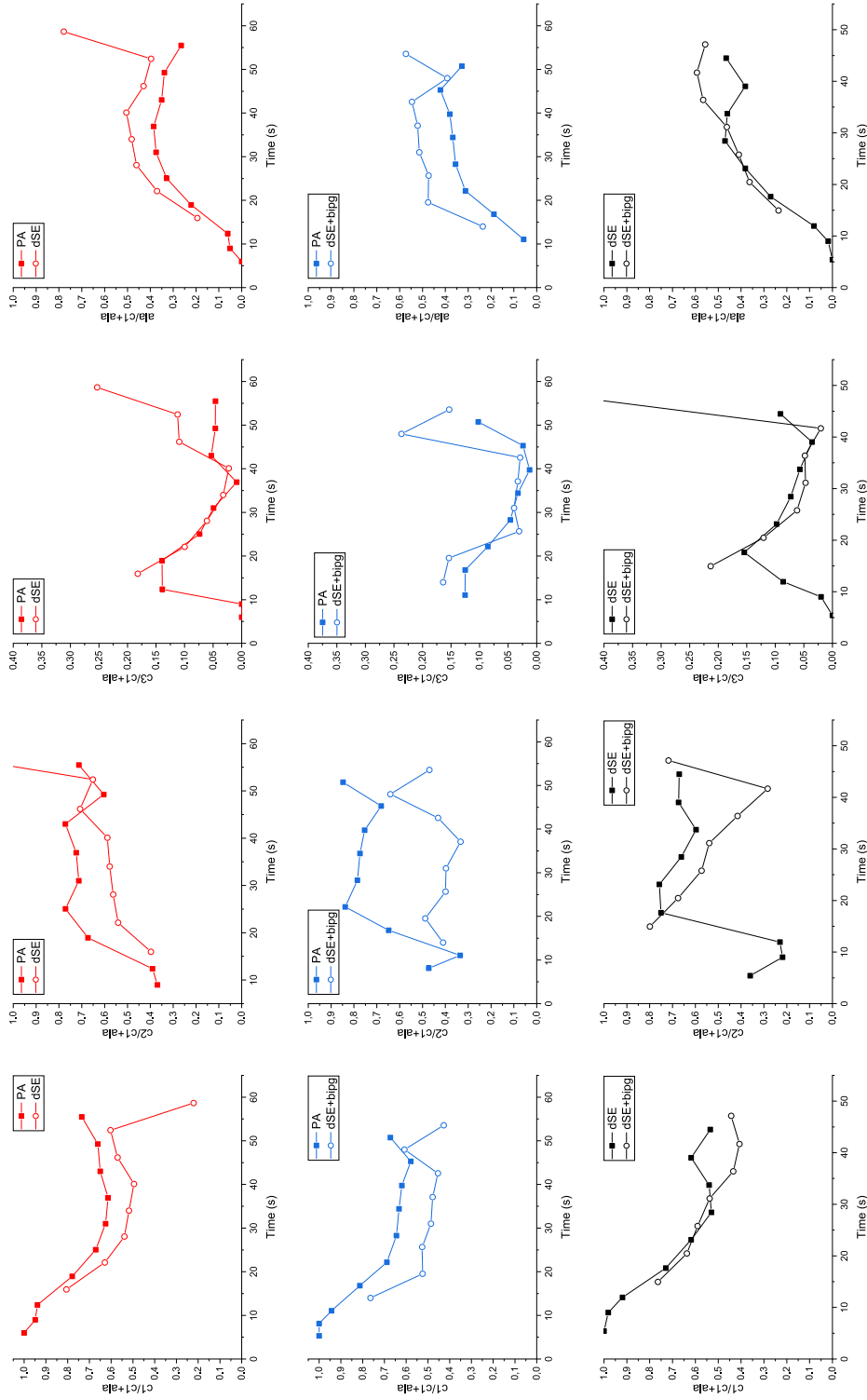


Figure 6.14 – Metabolite ratios with respect to the sum of the amplitudes of alanine and alaninamide compartment 1 for a representative experiment. The datasets are obtained from three consecutive acquisitions following infusion of hyperpolarized L-[1- ^{13}C]alaninamide. Red: interleaved pulse-acquire and double spin-echo with $G = 0$ mT/m. Blue: interleaved pulse-acquire and double spin-echo with $G = 520$ mT/m. Black: interleaved double spin-echo with and without bipolar gradients. The scatter of the last time points of compartments 2 and 3 is due to a very low signal level.

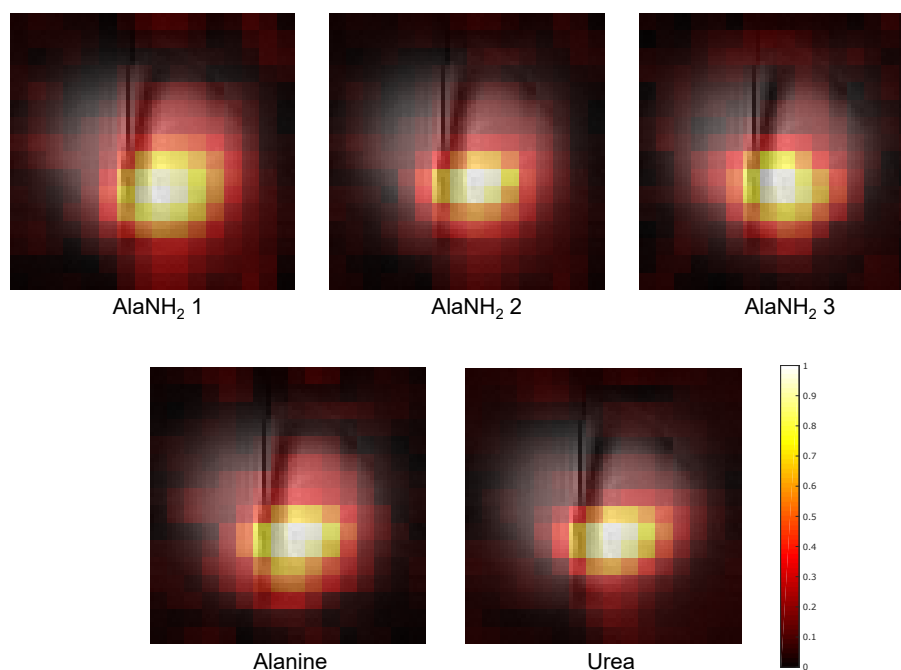


Figure 6.15 – ^{13}C metabolite maps acquired after a bolus injection of hyperpolarized L-[1- ^{13}C]alaninamide (colored) overlaid on the anatomical image of the kidney (greyscale). All ^{13}C maps are normalized to their maximum signal intensity.

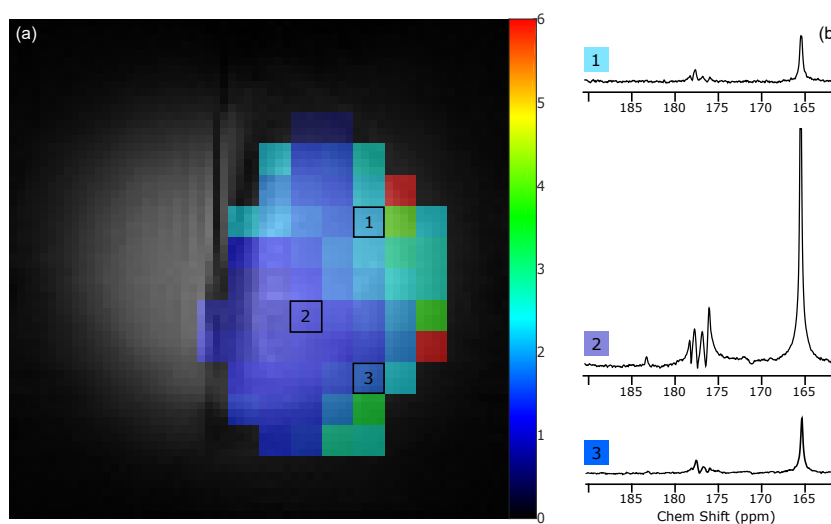


Figure 6.16 – (a) Map displaying the ratio between amplitudes of alaninamide compartments 1 and 3 (colored) overlaid on the kidney anatomical image (greyscale). The alaninamide map is masked outside the kidney to prevent artificially high ratio values in voxels with poor SNR. (b) ^{13}C spectra from the three highlighted voxels (post-processed), displayed in magnitude mode.

Chapter 6. Probing renal pH and aminopeptidase N activity using hyperpolarized L-[1-¹³C]alaninamide

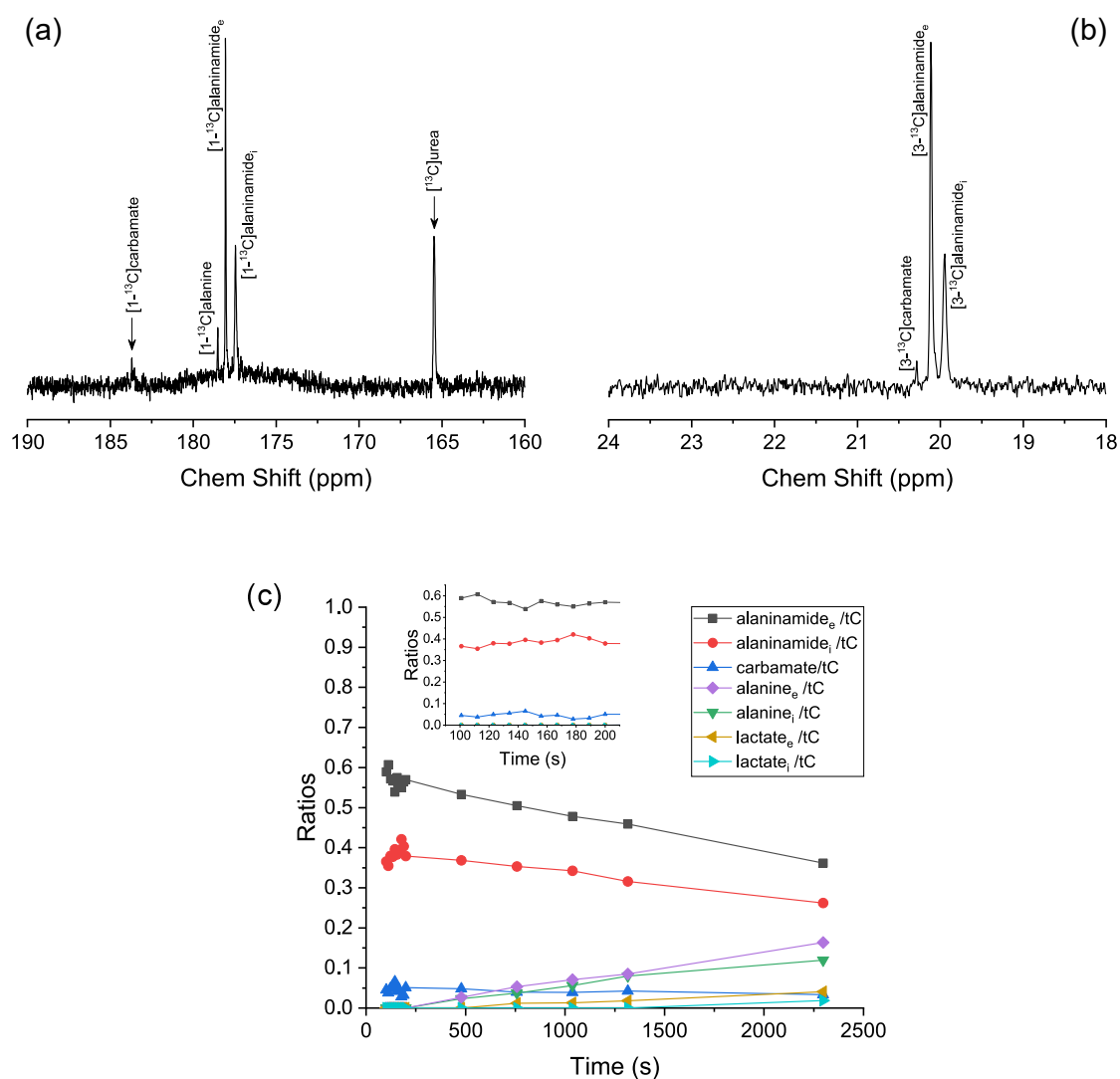


Figure 6.17 – (a) ¹³C NMR spectrum of L-[1-¹³C]alaninamide in blood acquired approximately 15 minutes after mixing. Two alaninamide peaks, assigned to the intra- and extracellular compartments, as well as alanine and carbamate are observed. (b) ¹³C NMR spectrum of L-[3-¹³C]alaninamide acquired about 101 s following mixing. Only two alaninamide compartments and carbamate are observed. (c) Time course of the metabolite ratios with respect to the total carbon signal after addition of L-[3-¹³C]alaninamide to blood. Lactate and alanine production is apparent only at later time points.

was still observed, and the chemical shift separation between intra- and extracellular compartments was 0.16 ppm. A third peak at 20.30 ppm was detected, and was assigned to the C3 resonance of the same species detected in the 1-¹³C experiment. This species, as shown in the following section, was identified with the carbamate adduct of alaninamide. At later time points, hydrolysis to alanine, also equilibrating between intra- and extracellular space, was seen together with further metabolism to lactate, as shown in Figure 6.17(c).

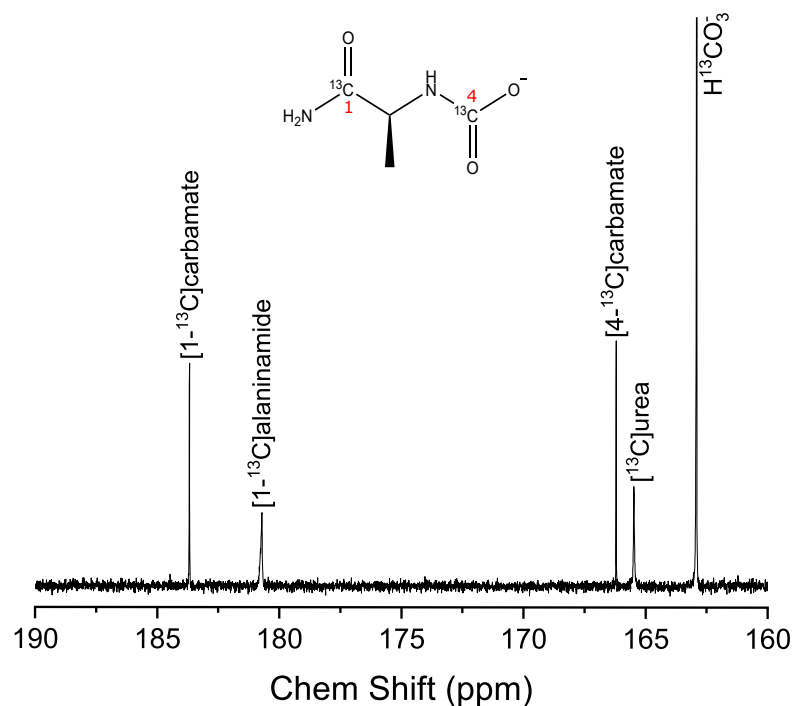


Figure 6.18 – ^{13}C spectrum of a mix of L-[1- ^{13}C]alaninamide, $\text{H}^{13}\text{CO}_3^-$ and ^{13}C urea at 9.4 T, 37 °C. Carbamate formation is observed, with the C1 and the carboxyamino (4) peaks appearing at 183.67 ppm and 166.21 ppm respectively.

Carbamate formation

L-[1- ^{13}C]alaninamide was mixed with a $\text{NaH}^{13}\text{CO}_3$ solution to determine whether the peak observed at 183.67 ppm *in vivo* and *ex vivo* in blood originated from the reaction between the two. The ^{13}C NMR spectrum of the reaction product is shown in Figure 6.18. Indeed, formation of (S)-(1-amino-1-oxopropan-2-yl)-1- ^{13}C carbamate- ^{13}C was observed, with the C1 and C4 peaks appearing at 183.67 ppm and 166.21 ppm, respectively.

Carbamate as a pCO_2 sensor

The *in vivo* carbamate-to-total carbon ratio was observed to be constant after the second scan from the bolus arrival (data not shown). A moderate correlation between carbamate-to-total carbon ratio and compartment 1 pH was found (Pearson's R 0.35), whereas no correlation with the pCO_2 level at the time of injection was observed. These results are shown in Figure 6.19. The apparent equilibrium constant regulating the carbamate formation was estimated to be 0.0042, but the fit did not reproduce well the experimental data (data not shown).

Chapter 6. Probing renal pH and aminopeptidase N activity using hyperpolarized L-[1-¹³C]alaninamide

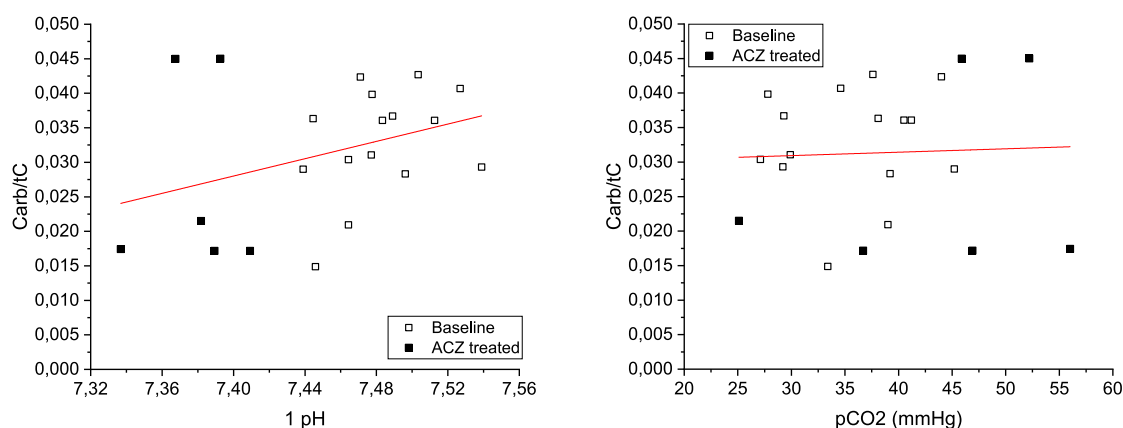


Figure 6.19 – Left: carbamate-to-total carbon ratio as a function of compartment 1 pH. A moderate correlation (Pearson's R= 0.35) between the two was observed. Right: carbamate-to-total carbon ratio as a function of pCO₂. No correlation was observed between the two variables.

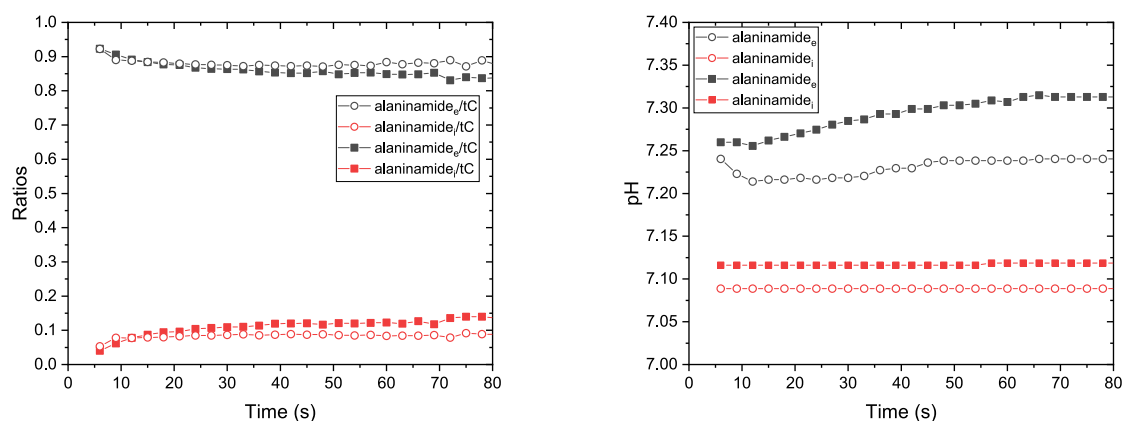


Figure 6.20 – Left: kinetics of the two alaninamide compartment ratios after infusion of the hyperpolarized substrate in blood. Right: pH time dependence of the two alaninamide compartments. Different symbol shapes are used for different experiments.

Ex vivo hyperpolarized ¹³C NMR

Blood experiments with hyperpolarized L-[1-¹³C]alaninamide, much like the *ex vivo* thermal experiments, revealed the presence of an intracellular alaninamide peak upfield in frequency with respect to the main alaninamide one. Calculation of the pH values of the peaks revealed that in the two experimental datasets the pH difference between compartments varied over time between 0.13 - 0.15 and 0.15 - 0.20 pH units, respectively. Approximately 10 % of the label was localized intracellularly.

Discussion

In the present study we report for the first time the uptake and metabolism of L-[1- ^{13}C]alaninamide in the rat kidney *in vivo*. Upon infusion, alaninamide undergoes different processes: in the kidney, it gets hydrolyzed, likely by aminopeptidase N, thus producing alanine; moreover, it shows a chemical shift sensitivity to pH that makes it a suitable probe of pH *in vivo*; finally, it reacts with blood carbon dioxide to generate its carbamate adduct.

Probe of APN activity

Hyperpolarized alaninamide in the rat kidney was hydrolyzed to alanine, just like in mouse kidney homogenate.¹³³ The reaction was likely catalyzed by APN, as conversion of the parent substrate to alanine was not observed in the heart, where the enzyme activity is known to be low.¹⁴⁹ Hydrolysis of alaninamide, possibly catalyzed by other enzymes, occurred in blood as well, as thermal experiments showed. Here, however, alanine was produced at a slower rate: its signal was detected starting from minutes after substrate addition, so at a much longer timescale than in hyperpolarized studies. APN being a membrane-bound ectoenzyme,¹²⁹ alanine production takes place in the proximal tubules. The metabolite is then expected to be almost completely reabsorbed by the kidney. Micropuncture studies of amino acid reabsorption across the kidney have indeed shown that 80 % of the load is reabsorbed in the proximal tubule, and less than 1 % of the filtered amino acids is excreted.^{150;151} The alanine signal, that flow suppression experiments showed to be less mobile than the alaninamide compartments, could not always be spectrally resolved from the blood pool signal (compartment 1) of the substrate, especially when blood pH approached 7.4. This overlap limits the use of hyperpolarized alaninamide as a probe for aminopeptidase N enzymatic activity *in vivo*.

pH sensitivity

A pH dependence of the ^{13}C alaninamide chemical shift following protonation/deprotonation of the amine group was observed. The pK_a of the molecule at 37 °C is sufficiently close to physiological pH for the compound to be sensitive to pH variations *in vivo*. One should note that the pK_a value measured here is lower than the one reported by Hundhammer *et al.*,¹⁵² this difference can be at least partially explained by the different temperatures at which the experiments were conducted. Upon bolus arrival in the kidney, three distinct alaninamide spectral peaks were observed and were attributed to three different pH compartments. The presence of regions of different pH is not surprising, as the reabsorption/secretion of bicarbonate and a number of other ions throughout the nephron is known to cause a pH gradient across the kidney.¹³⁴

Compartment assignment by ACZ treatment

To gain insights on the localization of the three alaninamide compartments, the pH in the kidney was perturbed by administering the rats an acute dose of acetazolamide. Acetazolamide is a carbonic anhydrase inhibitor that acts as a diuretic and whose net effect is that of acidifying blood pH and alkalizing urine pH.¹⁵³ Therefore, upon treatment, if the detected alaninamide peaks were stemming strictly from the tubular lumen, one would expect to see an increase in the compartments' pH. This is indeed what was found by Raghunand *et al.*¹³⁸ in mice chronically treated with ACZ by looking at the change in the relaxivity properties of a gadolinium chelate contrast agent that is not taken up by cells. Measures of interstitial pH using a standard electrode in the rat perfused kidney¹³⁵ showed instead a decrease of both cortex and medulla pH after a bolus injection of ACZ. Measures of renal intracellular pH by means of ³¹P MRS confirmed the same trend of decreasing pH_i after acute acetazolamide treatment, and showed a direct relationship between blood pH and pH_i.¹³⁷

The pH value of alaninamide compartment 1 significantly decreased after acetazolamide treatment, and was found to correlate with blood pH. The mismatch between the two values being explained by a mismatch in the values given by the two different pH electrodes used to perform the measurements, compartment 1 was assigned to the blood extracellular compartment. A contribution to this signal of the cortical fluid is also expected, given that the pH of filtrate follows that of plasma. The origin of the signal of compartments 2 and 3, on the other hand, could not be established. Compartment 2 is not sensitive to the pH perturbation induced by the acetazolamide, suggesting its localization is intracellular. Compartment 3, that in baseline conditions has a pH value close to the urine pH, cannot be assigned to the tubular-lumen in the calyx/ureter as its increase in pH following ACZ infusion does not match that of urine.

Flow-suppressed, CSI and *ex vivo* experiments were then performed to further probe alaninamide compartmentalization.

Assignment by flow-suppressed and localized experiments

Flow-suppressed experiments provided information, however qualitative, on the mobility of the compartments. The use of diffusion gradients embodied in the acquisition scheme was already proven useful in *in vivo* hyperpolarized studies aimed at suppressing the macrovascular signal^{147;154} or at determining the cellular uptake of metabolites.¹⁵⁵ Our flow-suppressed experiments were based on the same principles described in those studies. In particular, the gradients' *b*-value was tailored to obtain a good compromise between maximal suppression of the flowing spins and minimal diffusion signal loss. Even so, one should bear in mind that

the diffusing and intratubular contributions to the signal cannot be fully separated. Indeed, the intratubular velocity is estimated to range between 0.14 and 1.31 mm/s for tubules of 27 μm diameter,¹⁵⁶ so that for a spin moving at a velocity in the low edge of this range the effect of the gradients is similar to that on a diffusing spin. Moreover, a clear separation between microvascular and intratubular compartments is not possible, as again, the velocities of the spins in the two compartments are comparable.¹⁵⁷ Phantom experiments showed that the chosen sequence and set of gradient parameters and delays efficiently suppressed the signal of spins flowing parallel to the \mathbf{B}_0 field. *In vivo*, instead, no definite result could be obtained. The comparison of metabolite ratios in the pulse acquire and double spin-echo without and pulse acquire and double spin-echo with bipolar gradients showed a slight effect of the gradients on the signal level of compartments 1 and 2, both of which decreased, and no change in the signal level of compartment 3. However, these differences were no longer apparent when the two double spin-echo acquisitions were directly compared. Besides not having or not being able to detect differences in the underlying physical process, this could also be due to technical problems such as a non-ideal behavior of the refocusing pulses. Yet no apparent issue was observed in phantom tests and preliminary *in vivo* experiments with hyperpolarized pyruvate (Appendix C) suggested an overall good performance of the acquisition scheme. The differences between pulse acquire and double spin-echo could potentially also be accounted for by T_2 differences between compartments. One should also note that one of the main limitations in data analysis is that, since alanine could not always be resolved from alaninamide compartment 1, the metabolite ratios were calculated with respect to their sum. The two possibly being in regions moving at different speed makes the interpretation of the results even more difficult. This issue could potentially be resolved by performing the same experiments with hyperpolarized D-[1- ^{13}C]alaninamide, which shows the same pH-sensitivity but is not hydrolyzed to alanine.

The hyperpolarized ^{13}C CSI images provided information on the localization of the alaninamide signal. Unlike the spectroscopy experiments, images were acquired on the right kidney. The choice of the right side followed the observation of signal near the left kidney arising presumably from the blood pool of the spleen, which could potentially bias the quantification of alaninamide blood compartments in regions where the two organs overlap. This might have also biased the quantification of the AUC ratios in the MRS data. There, however, a lower relative contribution of the splenic signal is expected considering the homogeneous excitation provided by the BIR4 pulses and the lower blood flow per gram of tissue in the spleen¹⁵⁸ compared to the kidney.¹⁵⁹ Because of the \mathbf{B}_1 profile of the surface coil, 2D images were acquired on a coronal slice to achieve an rf-excitation as homogeneous as possible. The acquired spectra look somewhat different from those obtained from the unlocalized MRS because of the presence of a delay between excitation and acquisition that caused dephasing of the spins. The in-plane spatial resolution of the ^{13}C images (3.75 x 3.75 mm²) was only suffi-

Chapter 6. Probing renal pH and aminopeptidase N activity using hyperpolarized L-[1-¹³C]alaninamide

cient to determine that, when compared against compartment 1, alaninamide compartment 3 was more prominently distributed in the medulla/calyx. To achieve a higher resolution, sequences with faster **k**-space sampling schemes may be used.

Intracellular alaninamide

Evidence of intracellular uptake of alaninamide was already observed in thermal blood experiments with both [1-¹³C]alaninamide and [3-¹³C]alaninamide as substrate. The use of the 3-¹³C-labeled compound allowed the monitoring of time-dependent alaninamide uptake in blood cells thanks to the short $T_{1\rho}$ of the β carbon (~ 0.3 s at 14 T, 37 °C). Equilibration of the intra- and extracellular compartments of alaninamide was observed to take place within 1 min following substrate mixing. The means of transport of alaninamide into erythrocytes, whether through the same Na^+ -mediated transporters as for alanine^{160;161} or *via* passive diffusion as a free amine, were not determined. *Ex vivo* hyperpolarized blood experiments revealed the same intracellular uptake of the probe. The evidence gathered from the *ex vivo* experiment thus suggests that the signal of compartment 2 measured *in vivo* can be at least partially attributed to the intracellular blood compartment. This conclusion is supported by *in vivo* experiment of hyperpolarized L-[1-¹³C]alaninamide over the heart where, a second alaninamide peak assigned to the blood intracellular compartment and with kinetics comparable to those observed in the kidney is observed. Moreover, compartment 2 being insensitive to pH perturbation also points in this direction. A direct comparison between the relative weight of the intra- and extracellular compartment across the *ex vivo*, hyperpolarized and thermal, and *in vivo* experiments is not possible, as it would require experimental conditions, and in particular mixing and dilution, to be the same, which is not the case here. The fraction of intracellular blood signal that makes up for compartment 2 was thus not determined, and one cannot exclude that other anatomical compartments contribute to it.

Overall, when considering alaninamide as a pH probe, the generation of alanine *in vivo* may pose problems in quantifying the amplitude of the extracellular blood pool alaninamide signal, especially for blood pH values approaching 7.4. This issue may be avoided by using the D-enantiomer.

Conclusive evidence regarding the compartmentalization of hyperpolarized alaninamide in the rat kidney could not be obtained. Generally speaking, the probe behavior differs from that of other hyperpolarized pH probes that have been tested *in vivo*, namely ¹³C-labeled bicarbonate,¹⁶² its precursors,^{47;46} and [1,5-¹³C₂]zymonic acid.⁴² While both bicarbonate and zymonic acid are reported to be mainly sensitive to the extracellular space, alaninamide, at least in blood, probes the pH of both extra- and intracellular compartment. Whether it enters the renal intracellular space was however not determined. In this regard, clearance

experiments can help understanding how much and how fast the filtered alaninamide is excreted/reabsorbed.

A significant alteration in pH due to buffering effects upon infusion of the probe should not be expected, as the concentration of alaninamide in blood is much lower than that of bicarbonate (~ 4 mM for a $60 \mu\text{L}$ bolus - the highest level used, *vs* 21 - 26 mM of endogenous bicarbonate). Toxicity of the probe was investigated by Hata *et al.*:¹³³ in HeLa cells mild alaninamide toxicity was observed only at high concentrations ($\gtrsim 20$ mM).

Carbamate production

Production of the carbamate adduct of alaninamide was observed *in vivo* following the infusion of hyperpolarized L-[1- ^{13}C]alaninamide with a peak appearing at 183.67 ppm. The identification of the compound giving rise to such a signal started by noting that the resonance was already present in the first scan, suggesting its rapid production in the blood. Moreover, the amplitude of the peak normalized to the total carbon signal was generally observed to level off within the first two acquisitions after bolus arrival, which implies equilibration of the reaction producing it.¹⁶³ This reaction was also noted to not be stereoselective, as the same peak was observed following the infusion of the D-enantiomer. Both hyperpolarized and thermal *ex vivo* experiments revealed the compound was generated in blood. Knowing then that amino acids can react with CO_2 to generate their carbamate adduct¹⁶⁴ also in physiological conditions,¹⁶⁵ an NMR experiment was run on a sample containing a solution of alaninamide and bicarbonate and confirmed that this was the case for alaninamide as well. This conclusion was additionally corroborated by *in vivo* experiments with hyperpolarized DL-[2- ^{13}C ,2- ^2H]alaninamide, that also excluded the initial hypothesis of the species being lactamide. Here, deuteration of the molecule at the α position was required to increase the $T_{1\rho}$ of the corresponding carbon, otherwise too short for *in vivo* measurements (5.1 s for 1 M alaninamide in water at pH 7.4, 37 °C and 9.4 T). The 2- ^{13}C 2 signal of the carbamate adduct was found downfield with respect to alaninamide, at a chemical shift displacement in agreement with the one reported by Ciftja *et al.*¹⁶⁴ for the carbamate adduct of alanine. The possibility of using carbamate as a pCO_2 sensor was investigated by studying the relationship between carbamate fraction, alaninamide compartment 1 pH, and pCO_2 value measured at the time of the hyperpolarized infusion. For this analysis, the fit was performed on the carbamate-to-total carbon ratio as measured in the second scan following bolus arrival in order to compromise between a maximal contribution of alaninamide blood pool signal, and a carbamate-to-total carbon ratio as close as its equilibrium value as possible. A tentative value for the apparent equilibrium rate constant K_{eq} of the reaction generating carbamate was thus obtained. However, the experimental data were not well represented by the fitting function. Renal pCO_2 values may be different from those in the blood and this may account

Chapter 6. Probing renal pH and aminopeptidase N activity using hyperpolarized L-[1-¹³C]alaninamide

for the apparent absence of a strong correlation between blood pCO₂ and carbamate signal. Indeed, tubular pCO₂ values in rats are ~ 26 mmHg higher than in systemic blood¹⁶⁶ and decrease following CA inhibition.

As Eq. 6.2.7 shows, the amount of carbamate produced following alaninamide infusion is directly related to the concentration of free amine in the blood. Because of their lower pK_a when compared to that of alaninamide, molecules like glycineamide, serineamide and diamino-propionic acid¹⁵² are expected to be more sensitive probes of blood CO₂ content. A test experiment with hyperpolarized [1-¹³C]glycineamide is shown in Appendix B, and, as expected, reveals a significantly higher carbamate-to-total carbon ratio. The ability to measure and image local pCO₂ levels using a hyperpolarized probe with optimized sensitivity could represent a significant advance in molecular imaging.

Conclusions

The *in vivo* uptake of hyperpolarized L-[1-¹³C]alaninamide was investigated, with a particular regard to sensitivity of the probe to aminopeptidase N activity, pH and blood CO₂.

Hydrolysis of alaninamide to alanine in a timescale comparable to that of the hyperpolarized experiment was observed in the kidney only. While this points to APN being the enzyme that catalyzes the reaction, the spectral overlap between alanine and alaninamide limits the use of alaninamide as a probe for APN activity.

Renal pH sensitivity, arising from protonation/deprotonation of the amine group and a pK_a value of 7.9, was observed with the appearance of three alaninamide compartments of average pH 7.46, 7.21 and 6.58, respectively. While compartment 1 at pH 7.46 could be assigned to the extracellular blood pool signal, the origin of the other two compartments could not be readily determined. To gain further insights on the matter, *ex vivo* and *in vivo* experiments involving pH perturbation with acetazolamide, flow-suppressed and localized acquisitions were performed. Post acetazolamide treatment experiments ruled out compartment 3 being urine, as the increase in urine pH induced by the drug did not match that of compartment 3. 2D-CSI experiments showed on the other hand that, when compared to compartment 1, compartment 3 appeared to be predominantly localized in the medulla/calyx. Blood experiments revealed that alaninamide enters the intracellular compartment in a relatively short timescale. Owing to matching chemical shifts and insensitivity to pH perturbations, a contribution of the blood intracellular space to compartment 2 was therefore hypothesized. Finally, flow suppression experiments did not yield any definite evidence. Unlike other hyperpolarized pH probes, alaninamide is found, at least in blood, in both extra- and intracellular space. Whether uptake of the probe in cells of other tissues also takes place is yet to be determined.

Finally, alaninamide was observed to react with blood CO_2 forming a carbamate adduct. The reaction was observed to equilibrate in the timescale of the hyperpolarized experiment. While a correlation between carbamate fraction and compartment 1 pH was found, it varied substantially between experiments and may reflect local differences in pCO_2 *vs.* systemic levels.

7 *In vivo* detection of D-amino acid oxidase with hyperpolarized D-[1-¹³C]alanine

Adapted from:

In vivo detection of D-amino acid oxidase with hyperpolarized D-[1-¹³C]alanine

Radaelli A, Grütter R, Yoshihara HAI, NMR in Biomed 2020, 33, 7:e4303.

DOI: <https://doi.org/10.1002/nbm.4303>

My contribution consisted in performing experiments and data analysis. The interpretation of the data and the manuscript writing have been done by myself in collaboration with the co-authors.

Abstract

D-amino acid oxidase (DAO) is a peroxisomal enzyme that catalyzes the oxidative deamination of several neutral and basic D-amino acids to their corresponding α -keto acid. In most mammalian species studied, high DAO activity is found in the kidney, liver, brain and polymorphonuclear (PMN) leukocytes, and its main function is to maintain low circulating D-amino acids levels. DAO expression and activity have been associated with acute and chronic kidney diseases and to several pathologies related to N-methyl-D-aspartate (NMDA) receptor hypo/hyper-function; however, its precise role is not completely understood. In the present study we show that DAO activity can be detected *in vivo* in the rat kidney using hyperpolarized D-[1- ^{13}C]alanine. Following a bolus of hyperpolarized D-alanine, accumulation of pyruvate, lactate and bicarbonate was observed only when DAO activity was not inhibited. The measured lactate-to-D-alanine ratio was comparable to the values measured when the L-enantiomer was injected. Metabolites downstream of DAO were not observed when scanning the liver and brain. The conversion of hyperpolarized D-[1- ^{13}C]alanine to lactate and pyruvate was detected in blood *ex vivo*, and lactate and bicarbonate were detected scanning the blood pool in the heart *in vivo*; however the bicarbonate-to-D-alanine ratio was significantly lower compared to the kidney. These results demonstrate that the specific metabolism of both enantiomers of hyperpolarized [1- ^{13}C]alanine in the kidney and in the blood can be distinguished, underscoring the potential of D-[1- ^{13}C]alanine as a probe of D-amino acids metabolism.

Introduction

While being less abundant than L-amino acids, D-amino acids are widespread in nature and take part in normal mammalian metabolism. Aside from D-serine and D-aspartate, which humans can synthesize endogenously, most D-amino acids are taken up through diet, and their levels are regulated by D-amino acid oxidase (DAO) and D-aspartate oxidase.¹⁶⁷ DAO, a peroxisomal flavoenzyme, catalyzes the conversion of basic and neutral D-amino acids into the corresponding α -keto acids in two steps. First, the D-amino acid is oxidized to an imino acid, and the flavin adenine dinucleotide (FAD) coenzyme is concomitantly reduced. The imino acid then undergoes non-enzymatic hydrolysis to yield the α -keto acid and ammonia. In mammals, DAO is most abundant in the kidneys, where it is expressed in the epithelial cells of the S2 and S3 segments of the proximal tubules. DAO is also found in hepatocytes, in the central nervous system (CNS) and in polymorphonuclear (PMN) leukocytes. The physiological and pathological roles of D-amino acids and D-amino acid oxidase in these tissues is not completely understood. DAO has been shown to play a detoxifying role in the kidneys, as it helps maintain low D-amino acids levels.¹⁶⁸ Since it controls D-serine levels, DAO activity in the CNS has been associated with conditions affecting N-methyl-D-aspartate (NMDA) receptor signaling/dysfunction, including schizophrenia,¹⁶⁹ amyotrophic lateral sclerosis^{170;171} and Alzheimer's disease.¹⁷² DAO in leukocytes plays a bactericidal role against certain bacteria *in vitro*,^{173;174} but *in vivo* this effect remains controversial.¹⁷⁵ DAO activity is difficult to detect directly *in vivo* using substrates labeled with radioisotopes, as the products can be rapidly converted to a variety of other metabolites whose chemical identities are distinguishable only by invasive methods.¹⁷⁶ Chromatographic separation methods and mass spectrometry of stable-isotope labeled D-amino acid tracers have been used to measure the downstream metabolites of DAO in plasma and urine.^{177;178}

The aim of the present study was to assess the feasibility of exploiting the high sensitivity given by dynamic nuclear polarization to detect DAO activity *in vivo* using hyperpolarized D-[1-¹³C]alanine.

Methods

Hyperpolarization

Samples of D- or L-[1-¹³C]alanine (Sigma-Aldrich, Buchs, SG, Switzerland) were dissolved in 1 molar equivalent of a 10 M solution of NaOH in D₂O. Glycerol, corresponding to 10% of the final volume, and 25 mM of OX063 trityl radical (Albeda Research, Copenhagen, DK) were then added. The final alanine concentration was estimated to be approximately 5 M. The enantiomeric purity of the two sample preparations was determined by synthesizing di-

Chapter 7. *In vivo* detection of D-amino acid oxidase with hyperpolarized D-[1-¹³C]alanine

astereoisomer derivatives following a procedure described by Katritzky *et al.*¹⁷⁹ The fraction of each stereoisomer was then measured by conventional ¹H NMR. Details of the experimental procedure and results are shown in Appendix E. For the *in vivo* experiments, either 25 μ L or 50 μ L aliquots of the preparation were rapidly frozen and placed into a polytetrafluoroethylene sample cup, together with frozen droplets of HCl to ensure pH neutralization upon dissolution.¹⁸⁰ For the *in vitro* experiments, the sample cup was loaded with 17.7 μ L aliquots of the preparation and HCl. The samples were polarized in a custom-built 7 T polarizer⁷¹ at 1 K by shining microwave radiation at 196.58 GHz, 50 mW in power. The polarization buildup was monitored for approximately two hours, after which the samples were dissolved in 5.5 mL of a hot phosphate buffer solution in D₂O (pH 7.4) and rapidly transferred (3 s) to a separator-infusion pump located in the animal scanner.

Concentration measurements

The alanine concentration in the injected solution was measured by means of high-resolution ¹³C NMR using [1-¹³C]glycine as an internal standard. After each hyperpolarized experiment, 580 μ L aliquots of the dissolved samples were collected, and to each 20 μ L of a 1 M [1-¹³C]glycine, 2 mM gadoteric acid solution in D₂O was added. ¹³C NMR spectra were then acquired on a 400 MHz vertical scanner (Bruker Biospin) equipped with a standard BBFO_z coil (acquisition parameters: $\text{sw} = 7812.5$ Hz, $\text{at} = 4.2$ s, $\text{ns} = 16$, $\text{TR} = 90$ s, 30° FA, inverse gated decoupling). The concentration of alanine was calculated by comparing the integral of the alanine peak with that of glycine.

Animals

All animal experiments were conducted according to federal and local ethical guidelines, and the protocols were approved by the local regulatory body of the Canton de Vaud, Switzerland. Thirteen male Wistar rats (250-300 g) were initially anaesthetized using 5% isoflurane in 50% oxygen, and were maintained at 1-2% isoflurane for the remainder of the experiment. Cannulation of the femoral vein was performed to administer the hyperpolarized solution and the DAO inhibitor. Catheters were also placed in each femoral artery to monitor blood pressure and to allow for blood sampling. Blood gases, pH and physiological parameters were measured shortly after each infusion. To inhibit DAO activity, a dose of 10 mg/kg of a 27 mM neutralized solution of 4H-furo[3,2-b]pyrrole-5-carboxylic acid (SUN)¹⁸¹ in PBS was injected intravenously in the rat 20 minutes prior to the hyperpolarized [1-¹³C]alanine infusion.

¹³C MRS acquisition and data analysis

All experiments were performed on a 9.4 T/ 31 cm horizontal bore magnet (MagneX Scientific, Oxford, UK) with a VNMRs console (Varian, Palo Alto, CA).

***In vivo* experiments:** 1.4 mL of the hyperpolarized solution was infused in the animal over ~ 9 s. The ¹³C signal acquisition was performed by placing a 10-mm-diameter single loop ¹H and a pair of 10-mm-diameter ¹³C surface coils in quadrature mode over the left kidney, liver or heart of the animal. The same experiments were repeated in the brain by placing a quadrature ¹H and three-turn ¹³C surface coil ($\phi = 10$ mm for both channels) on top of the rat head. ¹H-decoupled ¹³C FIDs (sw = 20 kHz, at = 0.204 s, WALTZ-16 decoupling modulation) were acquired approximately every 2.9 s by applying 30° BIR4 pulses. The acquisition was respiration-gated and cardiac-triggered. A non-hyperpolarized background scan was acquired after each hyperpolarized experiment to assess the contribution of natural-abundance ¹³C fat to the spectrum.

***In vitro* experiments:** 0.5 mL of the hyperpolarized solution was infused over ~ 9 s into a 10 mm NMR tube containing 2 mL of freshly collected rat blood with heparin added (10 U per mL of blood). The temperature was kept at 37° C for the duration of the experiment. The ¹³C signal was acquired using a three-turn ¹³C, single loop ¹H coil placed around the tube. ¹H-decoupled ¹³C FIDs (sw = 20 kHz, at = 1 s, WALTZ-16 decoupling modulation) were acquired every 3 s by applying a 5° hard pulse.

For each infusion, the acquired FIDs were summed and the resulting spectrum was fitted with Bayes (Washington University, St. Louis, MO) to determine the peak amplitudes. Metabolite signals are expressed as the ratio to the substrate signal and their values are presented as mean \pm S.D. An unpaired Student's *t*-test was used to assess the significance of the difference in lactate SNR and in bicarbonate-to-D-alanine ratio between heart and kidney.

Results

The liquid-state polarization level of D-alanine was directly measured in the scanner at $22.3 \pm 3.3\%$ ($n = 5$), and the *in vitro* liquid-state $T_{1\rho}$ in buffered D₂O was 41 ± 2 s.

The alanine concentration in the injected solution was measured to be 26 ± 7 mM (D-ala) and 16 ± 6 mM (L-ala) for the 25 μ L samples, and 46 ± 9 mM (D-ala) and 52 ± 5 mM (L-ala) for the 50 μ L samples.

Upon injection of hyperpolarized D-[1-¹³C]alanine, two metabolite peaks were observed in the rat kidney at 185.1 ppm and 162.9 ppm, with the parent compound at 178.48 ppm¹⁴⁶ (Figure 7.1a). The chemical shifts of the two metabolites corresponded to those of lactate

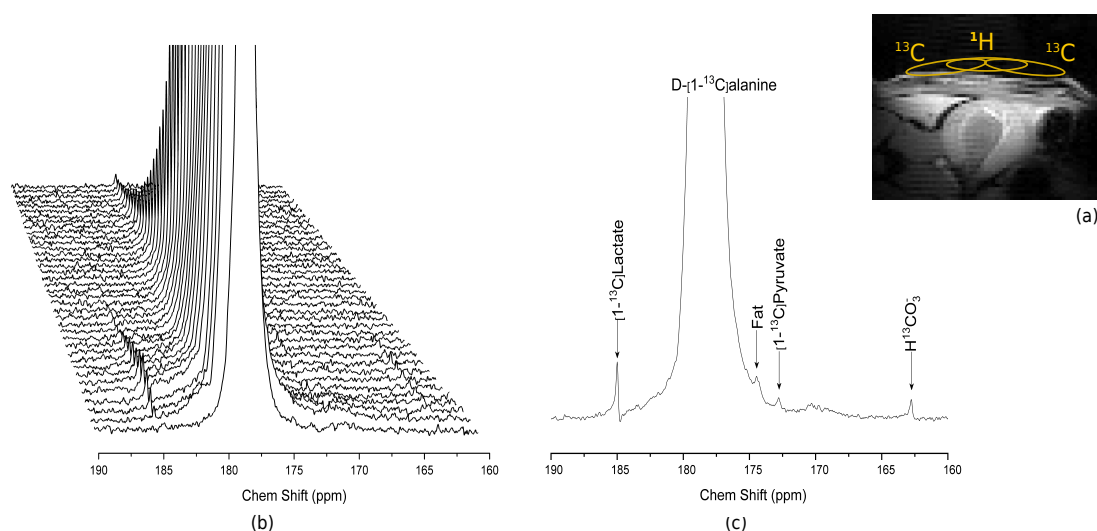


Figure 7.1 – (a) Anatomical image of the kidney with the location of the coil sketched on top. (b) Time course of the acquired spectra after the injection of 43.5 mM hyperpolarized D-[1-¹³C]alanine: buildup of [1-¹³C]lactate at 185.1 ppm and H¹³CO₃⁻ at 162.9 ppm can be observed in the individual spectra. (c) Sum of the acquired FIDs. Lactate, bicarbonate and traces of pyruvate become more apparent.

C1 and of bicarbonate, respectively. Despite being a metabolic intermediate, pyruvate could not be directly observed in the individual scans, but a small pyruvate peak became visible in five experiments out of nine when adding all the acquired spectra (Figure 7.1c). A shoulder peak next to alanine was also noted; however this resonance appeared in the baseline spectra acquired without any hyperpolarized probe present, and, therefore, was attributed to the natural-abundance ¹³C signal of lipids. No significant increase in the lactate SNR was observed when the bolus concentration was doubled. The lactate-to-D-alanine ratio was systematically evaluated and found to be 0.27 ± 0.17 % ($n = 4$) with the 25 μ L sample, and 0.23 ± 0.05 % ($n = 5$) with the 50 μ L sample. At this concentration, the bicarbonate-to-D-alanine ratio could also be consistently calculated and was found to be 0.080 ± 0.035 %. D-alanine metabolism could not be detected following the inhibition of the DAO enzyme ($n = 3$, Figure 7.2).

Control experiments performed by infusing hyperpolarized L-[1-¹³C]alanine revealed a similar metabolic profile. Comparable amounts of lactate, pyruvate and bicarbonate to those obtained after D-alanine infusion were detected. Accordingly, the lactate-to-L-alanine ratio was calculated to be 0.46 ± 0.31 % ($n = 3$) after the low dose injection, and 0.33 ± 0.16 % ($n = 4$) after the high dose. The high variability of these measurements was ascribed to the low SNR of the lactate peak. No significant difference in lactate-to-L-alanine ratio was observed when DAO was inhibited (0.46 ± 0.31 % before *vs.* 0.46 ± 0.13 % after inhibition, both experiments repeated three times). Figure 7.3 summarizes the metabolic ratios for the two

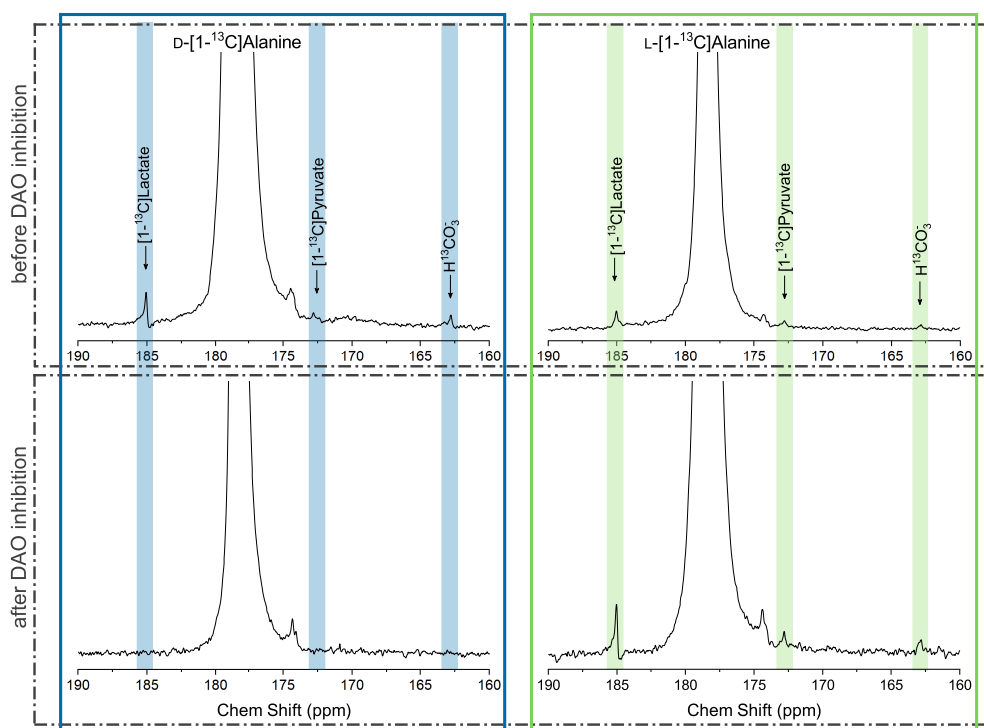


Figure 7.2 – Representative sums of the spectra acquired on the kidney after injecting $[1-^{13}\text{C}]$ alanine before and after DAO inhibition. No metabolism of the D enantiomer was observed once the enzymatic activity was inhibited, while that of L-alanine was unaffected by the DAO inhibitor. (Zoom factor 30x).

enantiomers at the two investigated concentrations. A similar apparent $[1-^{13}\text{C}]$ alanine decay rate, T_{1app} , comprising the real T_{1I} , the substrate metabolic uptake and the magnetization reduction due the rf-pulses, was observed for both D- and L-alanine.

D-alanine metabolism was not detected in the liver, and in the brain no metabolic products of either enantiomer were observed (data not shown).

To assess whether DAO activity in blood cells could contribute to the hyperpolarized D-alanine metabolism observed when scanning the kidneys, *in vitro* experiments were performed with rat blood. Upon addition of hyperpolarized D- $[1-^{13}\text{C}]$ alanine, formation of pyruvate and lactate was consistently observed (Figure 7.4, $n = 4$, lactate-to-D-alanine = 0.12 ± 0.06 %). To determine whether blood metabolism could be detected *in vivo* as well, the heart was scanned in rats infused with hyperpolarized D- $[1-^{13}\text{C}]$ alanine. In these experiments, lactate and bicarbonate could still be identified; a baseline distortion next to the lactate peak combined with its low SNR prevented however the reliable quantification of the lactate-to-alanine ratio. Table 7.1 displays the alanine and lactate SNR (calculated from the sum of the spectra) over the different tissues. A significantly higher lactate SNR ($p = 0.006$) was observed

Chapter 7. *In vivo* detection of D-amino acid oxidase with hyperpolarized D-[1-¹³C]alanine

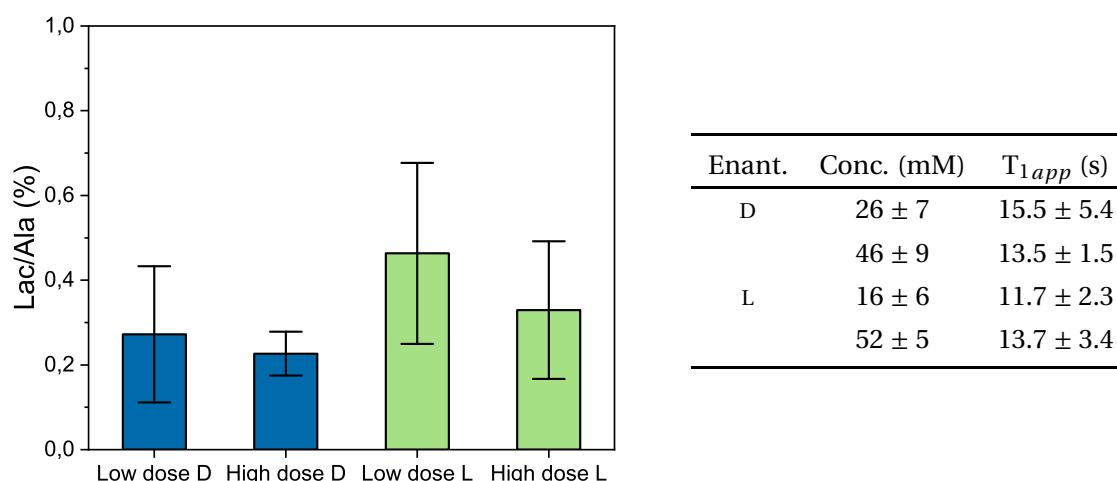


Figure 7.3 – Lactate to alanine metabolic ratios (in %) calculated from the sum of the FIDs acquired on the kidney for the two alanine enantiomers at the two investigated dosage levels. The table summarizes the concentration of the infused hyperpolarized alanine (1.4 mL) at the two dosage levels and the apparent rate of signal decay.

Table 7.1 – D-alanine and lactate SNR calculated on the sum of the FIDs. Despite a 1.5-fold increase in alanine SNR in the heart compared to the kidney, the lactate SNR is three times lower. In the liver, where the alanine SNR is comparable to that of the kidney, no lactate was observed.

Dose	SNR	Kidney	Heart (blood)	Liver	Brain
25 µL	Ala	3364 ± 842	-	2106 ± 747	898 ± 273
	Lac	11 ± 5	-	-	-
50 µL	Ala	4703 ± 967	6230 ± 1793	-	-
	Lac	16 ± 5	5 ± 2 **	-	-

** $p = 0.006$

in the kidney when compared to the heart. The bicarbonate-to-D-alanine ratio, on the other hand, could be calculated (bicarbonate-to-D-alanine = 0.030 ± 0.015), and was found to be significantly lower than that in the kidney ($p = 0.029$, Figure 7.6).

Similar results were observed when studying the metabolism of L-[1-¹³C]alanine *in vitro* in blood (lactate-to-alanine = 0.10 ± 0.01 %, $n = 2$), and *in vivo* in the heart (lactate-to-alanine = 0.63 ± 0.16 %, $n = 2$).

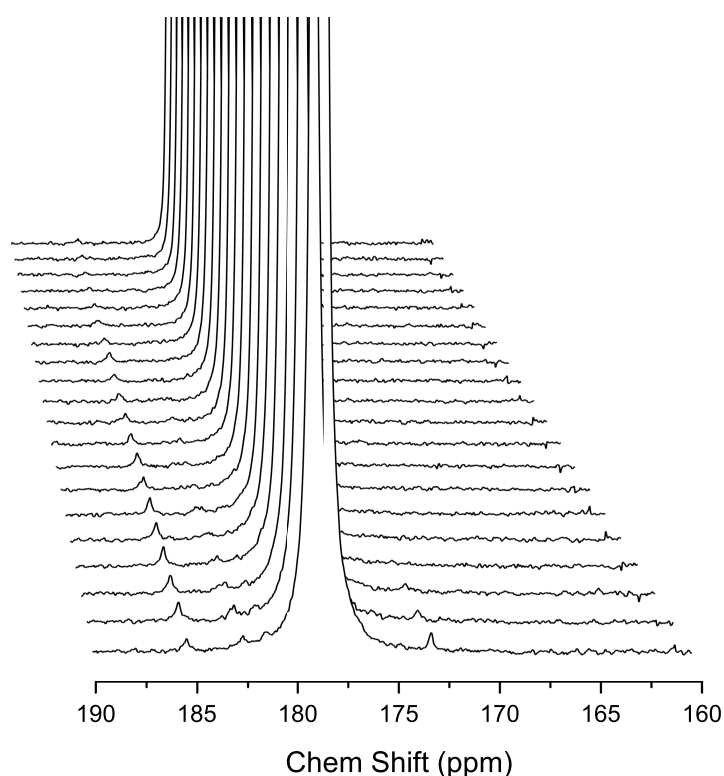


Figure 7.4 – Time course of the acquired spectra after the injection of 0.5 mL of hyperpolarized D-[1-¹³C]alanine in 2 mL of blood: buildup of [1-¹³C]lactate at 185.1 ppm and [1-¹³C]pyruvate at 172.9 ppm are observed in the individual spectra.

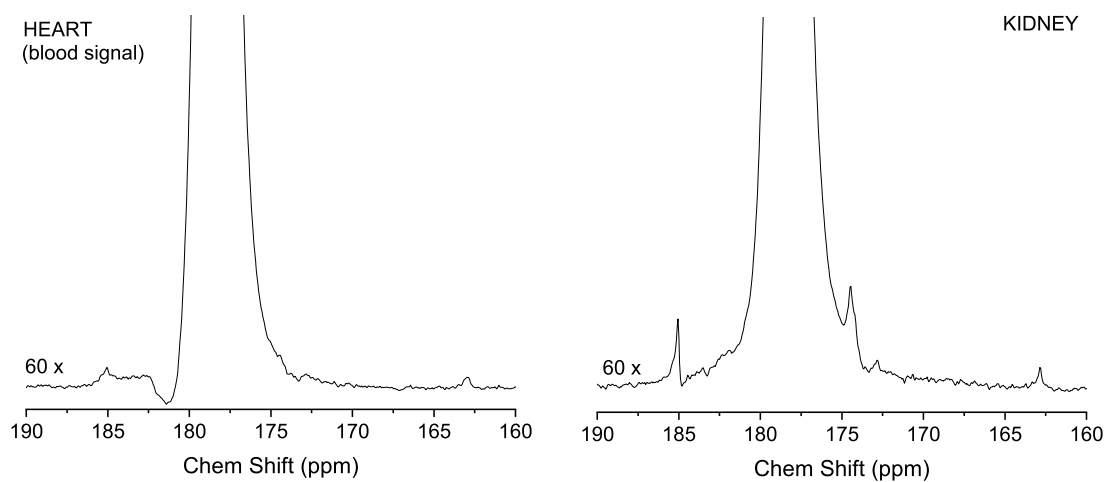


Figure 7.5 – Sum of the spectra over all experiments acquired scanning the kidney (left) and the heart (right) after injecting D-[1-¹³C]alanine. The vertical scale was adjusted to have a zoom factor of 60x with respect to the total alanine signal.

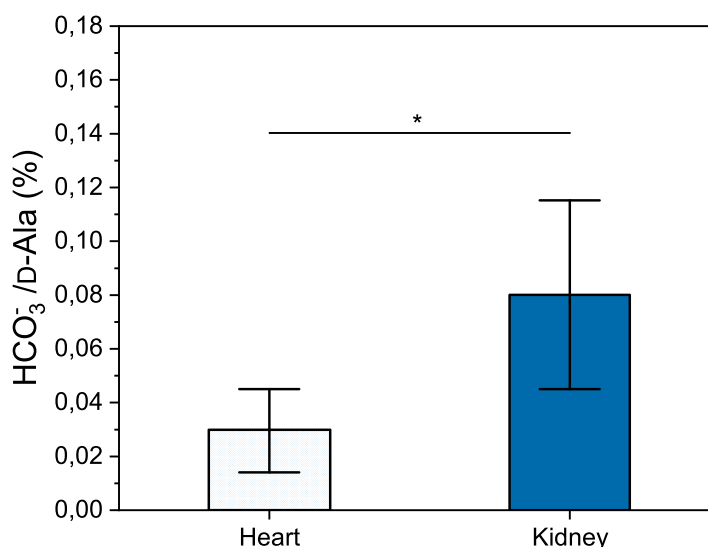
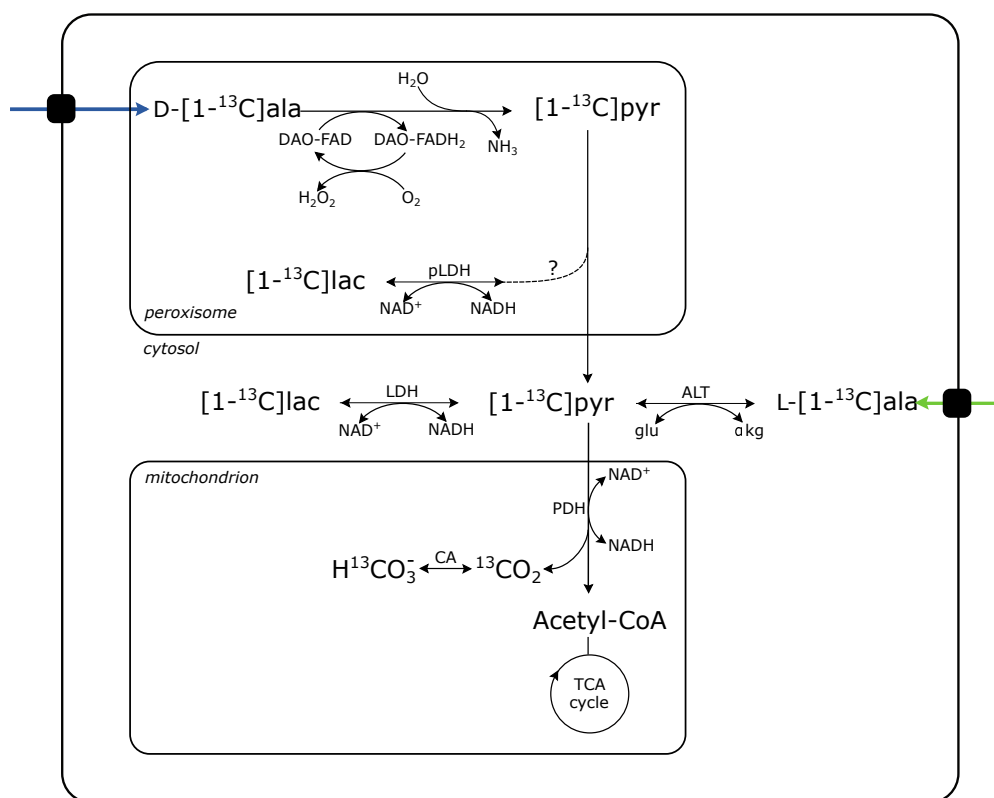


Figure 7.6 – Average bicarbonate-to-D-alanine ratios \pm S.D. measured scanning the heart and kidney. The difference between the two groups was found to be statistically significant (unpaired *t*-test, $p = 0.029$).

Discussion

The present study shows for the first time that D-amino acid oxidase activity can be detected *in vivo*, with a consistently observed conversion of hyperpolarized D-[1-¹³C]alanine to pyruvate, lactate and bicarbonate. A first indication that these products are indeed metabolites of D-alanine lies in their characteristic time course, as they did not appear in the first scan along with the parent compound, but their intensities increased over time (Figure 7.1a). The more conclusive evidence that pyruvate, lactate and bicarbonate result from D-alanine oxidation by DAO is given by the fact that they all readily disappeared when DAO activity was inhibited. The production of pyruvate labeled in the C1 position can be expected, as it results from DAO's oxidation of D-alanine into the corresponding imino acid and its subsequent hydrolysis. [1-¹³C]lactate and ¹³CO₂, the latter in rapid equilibrium with bicarbonate through carbonic anhydrase, can be generated from pyruvate by lactate dehydrogenase (LDH) and pyruvate dehydrogenase (PDH), respectively. These reactions can take place in the cytosol (LDH) and mitochondrion (PDH), where these enzymes are known to be expressed, provided that pyruvate passes through the peroxisomal membrane. Evidence of the presence of peroxisomal LDH in hepatocytes, where it contributes to maintaining redox balance within the organelle,^{182;183} also opens the possibility of [1-¹³C]lactate production *via* LDH directly in peroxisomes, which remains to be confirmed. Finally, some of the 1-¹³C label of pyruvate is also expected to be converted into C1 L-alanine *via* alanine aminotransferase (ALT), although its signal would be obscured by the D-alanine substrate. The proposed metabolic pathway for D-[1-¹³C]alanine is depicted in Figure 7.7.

Figure 7.7 – D- and L-[1-¹³C]alanine metabolic routes.

Conversely, in the L-alanine experiments conversion of the parent substrate into pyruvate is catalyzed by ALT. Similarly, pyruvate is then either reduced to lactate or oxidized to CO₂ and acetyl-CoA. When compared to previously reported experiments with hyperpolarized L-alanine in the liver,³⁹ the production of pyruvate and lactate appears to be approximately two-fold lower in the kidney. This would point to differences in uptake and/or to a lower renal ALT activity, with the latter likely playing a role given the 40-fold lower ALT activity per unit mass in the kidney *vs.* liver,¹⁸⁴ as well as to the different vascular content of the tissues.

The metabolites of both alanine enantiomers are produced intracellularly: in the kidney, after filtration, both L- and D-alanine are transported into the proximal tubule epithelial cells by the same carrier-mediated process.^{185;186} While the first step of the L-alanine metabolism takes place directly in the cytosol, D-alanine has to pass through the peroxisomal membrane before being metabolized. When comparing the apparent ALT and DAO fluxes, together with the potentially rate-limiting transport steps one should also take into account the different endogenous pool sizes of the two alanine enantiomers. A larger endogenous substrate pool, as is the case for L-alanine, entails a lower ¹³C isotopic enrichment of the metabolite pool. These differences in transport, along with the different compartments and isotopic enrichments of the two enantiomer pools render the comparison between ALT and DAO fluxes

Chapter 7. *In vivo* detection of D-amino acid oxidase with hyperpolarized D-[1-¹³C]alanine

difficult. Therefore, while the lactate-to-L- and lactate-to-D-alanine ratios are comparable in magnitude, this result requires higher ALT activity than that of DAO. Indeed, ALT activity in the rat nephron has been reported to be approximately 25-fold higher than DAO, with a similar expression pattern of both enzymes along the nephron.¹⁸⁷

The two different D-alanine concentrations yielded very similar lactate-to-D-alanine ratios. This would indicate that, when doubling the bolus dose, saturation of transporters and enzymes involved in lactate production does not occur, since in this case one would expect the same amount of lactate being generated from a significantly higher alanine signal, and thus an overall lower lactate-to-D-alanine ratio. The same conclusion can be drawn for the L-enantiomer.

When the same experiments were repeated in the liver, no D-alanine metabolism was observed, indicating that D-alanine uptake and/or DAO activity was not sufficiently high. This would be in line with the reported two-fold lower DAO activity levels in the rat liver compared to the kidney.¹⁸⁸ By contrast, *in vivo* observation of hepatic DAO using conventional ¹³C MRS was reported in the form of glucose accumulation over 1 hour after infusion of D-[1-¹³C]alanine.¹⁸⁹ No other metabolic intermediate was detected, however, and one must take into consideration the different precursor dosage and acquisition timescale when comparing the hyperpolarized ¹³C experiments with conventional ¹³C MRS.

In the brain, neither DAO nor ALT products of hyperpolarized D-/L-[1-¹³C]alanine were detected, probably due to the lower levels of enzymatic activity^{190;191} together with the slow uptake of alanine in the brain, which does not have a high affinity for the transport systems compared to competing amino acids.¹⁹² A preferential uptake of the D-isomer has, however, been reported.¹⁹³ One should note that the experiments did not preferentially target the cerebellum, where DAO is more abundant.¹⁶⁹

In the blood, DAO metabolism of D-alanine was also detected as pyruvate and lactate production. PMN leukocytes are noted to have high levels of DAO activity, rivaling those in the kidney (per mg protein in tissue homogenate).¹⁷³ To verify whether PMN DAO activity can be observed *in vivo*, thus determining if it contributes to the metabolite signal measured in the kidney, the rat heart was scanned after infusion of D-alanine. DAO activity is negligible in the heart,^{194;195;196} therefore any metabolic products can be attributed to DAO in blood cells. The detection of lactate and bicarbonate in the heart indicates that a fraction of the metabolism observed in the kidney originates from the blood. How significant this fraction is could not however be determined: the kidney DAO metabolism appears to be higher than that measured scanning the heart, as the lactate SNR and the bicarbonate-to-D-alanine ratio are significantly lower in the latter. Moreover, the fact that in the liver the alanine SNR is comparable to that in the kidney but no metabolites were detected would point to pyruvate,

lactate and bicarbonate being products of renal metabolism. The blood contribution to the lactate signal measured *in vivo* in the kidney may be isolated by saturating the pyruvate signal before the MRS acquisition: in this case one would expect to detect only the inflowing lactate. The low SNR of the two metabolites, however, makes this experiment challenging.

Finally, that L-alanine metabolism was seen in blood experiments indicates that the blood may contribute as well to the L-alanine metabolite signals detected when scanning the kidney.

Potential toxicological effects of the injection of a bolus of D-alanine were not evaluated in the present work. However, previous reports on rats^{197;198} and humans¹⁹⁹ show that D-alanine must be administered at much higher levels than those used here for deleterious effects to be seen.

With metabolic products being consistently observed, hyperpolarized D-[1-¹³C]alanine can be employed to rapidly assess DAO activity *in vitro* and *in vivo*. When compared to other molecular imaging techniques that exploit D-amino acids, the main one being PET with D-[methyl-¹¹C]methionine as a contrast agent for bacterial infection,²⁰⁰ hyperpolarized D-alanine shows greater specificity for detecting DAO activity.

Conclusions

D-amino acid oxidase activity can be detected *in vivo* in the rat kidney and *in vitro* in blood following an injection of hyperpolarized D-[1-¹³C]alanine from the production of pyruvate, lactate and bicarbonate when DAO activity is not inhibited. Peroxisomal metabolism can be monitored in real time using this method.

8 Conclusions and outlook

This thesis work describes mechanisms and biomedical applications of dDNP. The effect of sample composition on the DNP process was studied on two test systems, and the uptake and metabolism of two novel ^{13}C -labeled probes was characterized in the rat kidney.

DNP *via* pure thermal mixing and solid effect was observed for the first time on ^{13}C at 6.7 T, 1.1 K using SA-BDPA as a polarizing agent (**Chapter 4**). This was only possible because the ESR line of the radical was smaller than the ^{13}C Larmor frequency at 7 T. SA-BDPA also showed potential as a polarizing agent to be routinely used in *in vivo* studies. ^{13}C polarization levels above 40 % were consistently measured on ^{13}C urea doped with 120 mM of the radical, close to what can be obtained doping the sample with trityl. With *in vivo* applications in mind, a radical concentration calibration should be performed to determine the optimal radical content. It could also be worth investigating the behavior and stability of the radical with acidic or positively charged substrates. Finally, a setup making use of an anion exchange resin could be designed to rapidly filter out the radical post-dissolution.

The effects of solvent deuteration and radical choice (trityl *vs* TEMPOL) were studied on ^6Li DNP (**Chapter 5**). This study showed that at high field solvent deuteration did not affect the DNP properties in a predictable fashion, as the observed behavior was not explained with the thermodynamic model of thermal mixing. In some way this is consistent with what reported for ^{13}C , although the polarization dependence on solvent deuteration was different. Given that a rationale for the experimental observations was not found, further studies are required to fully understand the system's behavior. The dynamics and interplay of the different nuclear pools can be probed by performing multinuclear experiments both with and without microwave radiation. ^6Li DNP at lower fields (i.e. 3.35 and 5 T) could also be investigated to compare the observed trends with those of ^{13}C . Moreover, one could think of repeating the same experiments using ^6LiF as a substrate, where proton atoms could be envisaged to have the same effect on ^{19}F DNP as deuterons did for ^6Li , given the proximity in resonance

frequency of the two sets of species. On a final note, the measured ^6Li polarization was found to be significantly higher than what had been previously reported in the literature, and, if necessary, could potentially be further increased by carefully optimizing the sample composition and experimental conditions, for example by adding a gadolinium complex to the trityl sample or by modulating the microwave frequency when polarizing the TEMPOL sample.

The renal metabolism of hyperpolarized L-[1- ^{13}C]alaninamide was investigated in **Chapter 6**. L-[1- ^{13}C]alaninamide was shown to have interesting properties, being sensitive to aminopeptidase N activity, blood CO_2 content and local pH. In the kidney, at least three compartments of different pH could be probed. *Ex vivo* and localized *in vivo* studies allowed the assignment of the predominant compartment to the extracellular blood and cortical fluid pools and to identify a sizable contribution of the intracellular blood pool to the second largest compartment. The localization of the third smaller compartment could not however be determined. Further insights could be obtained by probing the absorbed and excreted fraction of alaninamide. Compared to the other hyperpolarized pH probes tested *in vivo*, alaninamide could potentially provide more information as it is sensitive to both the intracellular and extracellular compartments. However, to validate its use as a pH probe, the substrate distribution should be more thoroughly understood and the extent of intracellular uptake occurring in other tissues besides blood studied. For this purpose, tumor models may be better test systems than the kidney is as one would expect the pH compartments the probe is sensitive to to be well defined. To conclude, the sensitivity of alaninamide to pH, pCO_2 and the extra-intracellular environment may be optimized with analogues with enhanced sensitivity and specificity for specific parameters and compartments.

Finally, in **Chapter 7** the possibility of probing the metabolism of D-amino acids was explored. D-amino acid oxidase activity was observed *in vivo* after infusion of hyperpolarized D-alanine with the appearance of lactate, pyruvate and bicarbonate signals in the spectra. Metabolite ratios were comparable to those observed after the infusion of the L-enantiomer. This study represent an additional example of how intracellular metabolic pathways other than the major energy pathways can be probed with hyperpolarized ^{13}C . The technique could be used to study DAO activity in disease models characterized by an impairment of the metabolic activity of the enzyme. The low sensitivity of the method, however, would pose challenges for an accurate quantification.

The results discussed herein could only be obtained thanks to an optimal experimental setup and conditions. Performing the DNP experiments at high magnetic field was essential for observing ^{13}C DNP *via* solid effect with SA-BDPA, as the separation between the solid effect and thermal mixing lobes is directly proportional to \mathbf{B}_0 . The polarizer high field was also instrumental for obtaining the high ^{13}C polarization that was the starting point of *in vivo* studies. Here, and in particular for hyperpolarized D-alanine, having good sensitivity played a key

role for the detection of D-amino acid oxidase activity. Moreover, both *in vivo* experiments show the importance of determining the compartmentalization of the ^{13}C -label for data interpretation, the lack of which is at times a limitation of DNP.



Appendix

A ^{13}C dynamic nuclear polarization using SA-BDPA at 6.7 T and 1.1 K: co- existence of pure thermal mixing and well-resolved solid effect

Radical concentration measurements

SA-BDPA being synthesized in-house, the real SA-BDPA concentration was checked by means of ESR measurements. BDPA was used as calibration standard. A stock solution of 180 mM BDPA (Sigma-Aldrich, Buchs, SG, Switzerland) in polyethylene glycol (PEG) 400 was prepared, and appropriately diluted with PEG 400 to obtain three more solutions of 120, 60 and 30 mM BDPA, respectively. X-band ESR measurements were performed on a MiniScope MS 400 spectrometer (Magnettech GmbH, Germany) at 77 K. The acquisition parameters were set to: 20 mT range, 20 s sweep time, 0.2 mT modulation, 0.1 mW microwave power. For each BDPA concentration, four ESR spectra were acquired on up to 4 different 7 μL frozen pellets of solution. This procedure was repeated on three different sets of samples. The second integral of each ESR spectrum was calculated. A calibration curve was then drawn by linearly fitting the experimental data mean at each concentration to a linear curve; the error on each point was the corresponding standard deviation. The same experiments were then performed on four separate 7 μL droplets of the 120 mM SA-BDPA sample. The second integral of the ESR signal was compared against the calibration curve, and the actual SA-BDPA concentration was calculated.

The linear fit of the experimental points (Figure A.1) yielded a slope of: 153.9 ± 7.0 ($R^2 = 99.2$). The SA-BDPA concentration was then estimated by comparing the second integral of the ESR signal against this curve, and was found to be 100 ± 14 mM for the nominal 120 mM sample.

Derivation of the cut-off frequency Δ_0

Let us consider a system of N_S randomly distributed unpaired electron spins $S = 1/2$ in an amorphous solid. We assume the interaction between the electron spins to be purely dipolar.

**Appendix A. ^{13}C dynamic nuclear polarization using SA-BDPA at 6.7 T and 1.1 K:
coexistence of pure thermal mixing and well-resolved solid effect**

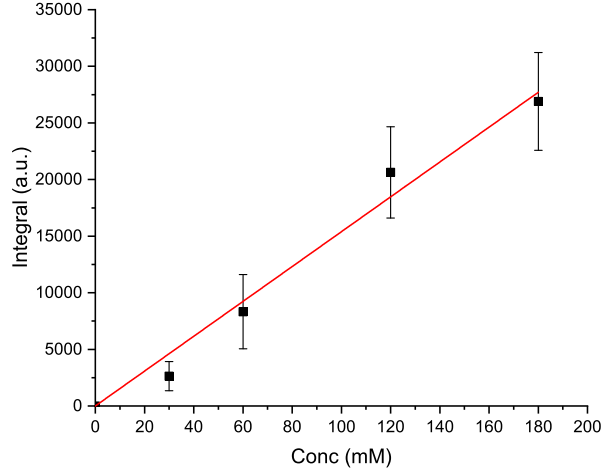


Figure A.1 – BDPA calibration curve.

The secular part of the dipolar Hamiltonian is responsible for the ESR line homogeneous broadening. This contribution can be calculated as the square root of the second moment. In the limit of zero polarization the second moment is:

$$M_2^0 = \frac{1}{4} \sum_{i \neq j}^{N_s} \left(D_{zz}^{ij} \right)^2$$

where $D_{zz}^{ij} = \frac{\mu_0}{4\pi} \frac{\hbar \gamma_S^2}{r_{ij}^3} (1 - 3 \cos^2 \theta_{ij})$ represents the interaction between the spin pair S_i and S_j separated by $\mathbf{r}_{ij} = (r_{ij}, \theta_{ij}, \phi_{ij})$. Since the unpaired electron spins are localized on a molecule of finite size, there exists a minimum distance r_0 between them corresponding to the maximum value of D_{zz}^{ij} . Averaged over its angular dependence this maximum value is equal to:

$$D_0 = \sqrt{\overline{\left(D_{zz}^{ij} \right)^2}} = \frac{1}{\sqrt{4\pi}} \frac{\mu_0}{4\pi} \frac{\hbar \gamma_S^2}{r_0^3} \left[\int_0^{2\pi} d\phi \int_0^\pi d\theta (1 - 3 \cos^2 \theta) \right]^{\frac{1}{2}}.$$

By means of the variable change $\cos \theta = x$ we obtain:

$$D_0 = \sqrt{\overline{\left(D_{zz}^{ij} \right)^2}} = \frac{\sqrt{2\pi}}{\sqrt{4\pi}} \frac{\mu_0}{4\pi} \frac{\hbar \gamma_S^2}{r_0^3} \left[\int_0^1 dx (1 - x^2) \right]^{\frac{1}{2}}.$$

The integral in dx evaluates to 8/5. Therefore we obtain:

$$D_0 = \frac{1}{\sqrt{2}} \frac{\mu_0}{4\pi} \frac{\hbar \gamma_S^2}{r_0^3} \sqrt{\frac{8}{5}} = \sqrt{\frac{4}{5}} \frac{\mu_0}{4\pi} \frac{\hbar \gamma_S^2}{r_0^3}.$$

Finally, dividing this equation by 2π we obtain it in frequency units:

$$\Delta_0 = \sqrt{\frac{1}{5}} \frac{\mu_0}{4\pi^2} \frac{\hbar \gamma_S^2}{r_0^3}.$$

The latter represents the cut-off frequency of the system.

B Probing renal pH and aminopeptidase N activity using hyperpolarized L-[1-¹³C]alaninamide

Alaninamide characterization

¹H NMR spectra of L-[1-¹³C]alaninamide methyl ester · HCl and L-[1-¹³C]alaninamide · HCl

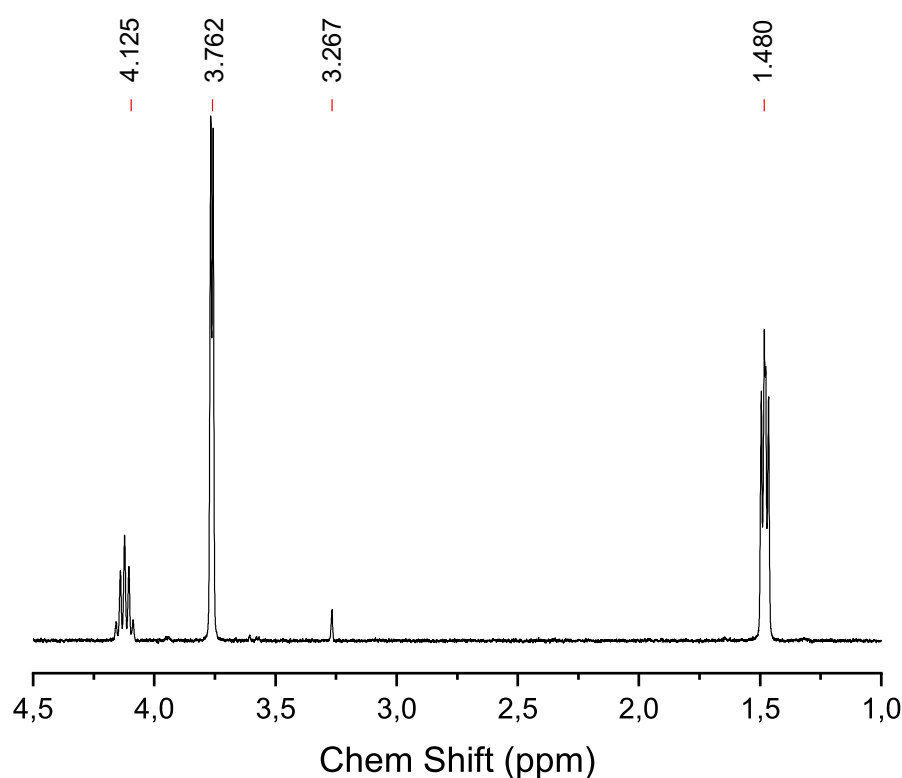


Figure B.1 – ¹H NMR spectrum of L-[1-¹³C]alaninamide methylester · HCl in D₂O at 9.4 T. The methyl ester doublet is at 3.762 ppm. Traces of methanol are observed at 3.267 ppm.

Appendix B. Probing renal pH and aminopeptidase N activity using hyperpolarized L-[1-¹³C]alaninamide

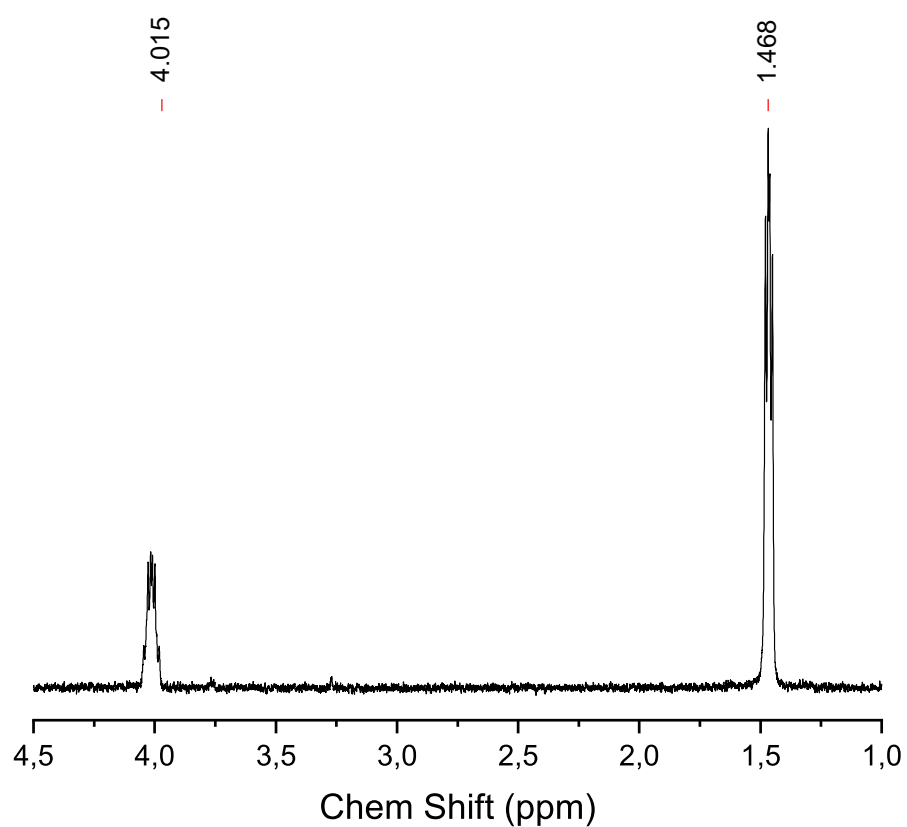
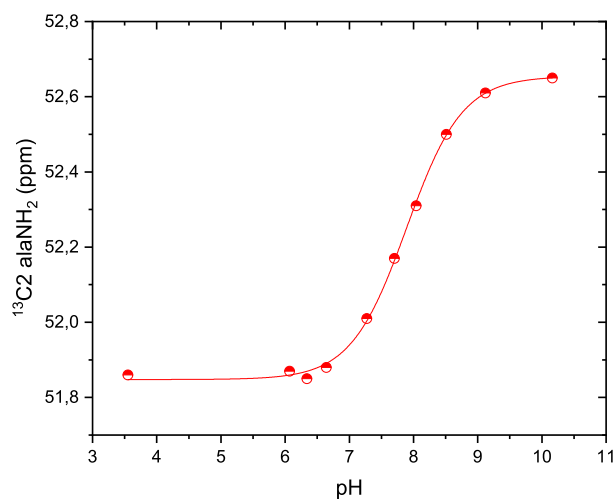
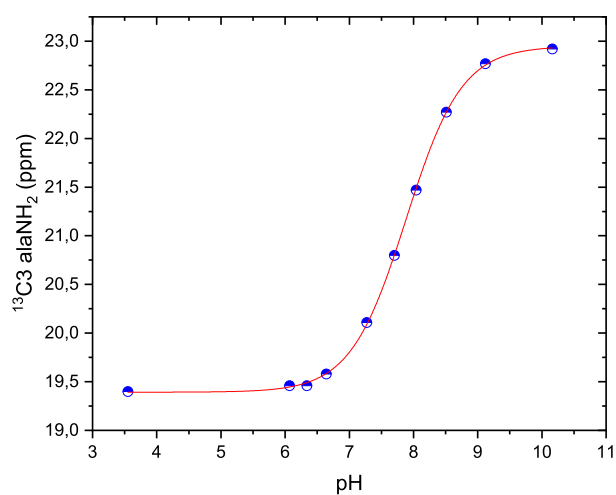


Figure B.2 – ¹H NMR spectrum of L-[1-¹³C]alaninamide · HCl in D₂O at 9.4 T. The α and β protons of alaninamide are clearly visible, along with some trace amounts of the methylester peak.

Supplemental titration curves

Figure B.3 – Titration curve of the α carbon of alaninamide (37 °C, 9.4 T).Figure B.4 – Titration curve of the β carbon of alaninamide (37 °C, 9.4 T).

Flow suppression data

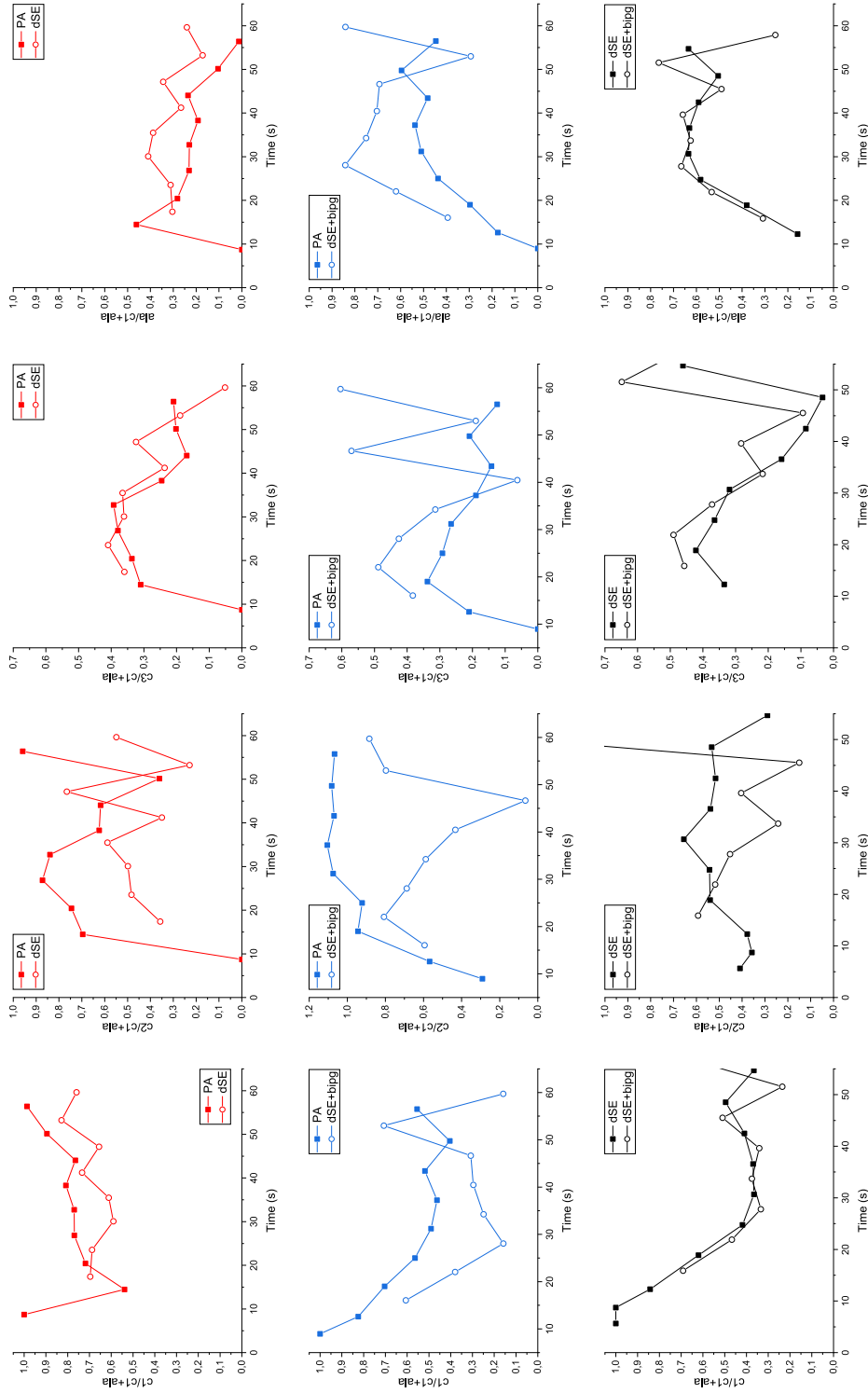


Figure B.5 – Metabolite ratios with respect to the sum of the amplitudes of alanine and alaninamide compartment 1 for a representative experiment. The datasets are obtained from three consecutive acquisitions following infusion of hyperpolarized L-[1-¹³C]alaninamide. Red: interleaved pulse-acquire and double spin-echo with $G = 0$ mT/m. Blue: interleaved pulse-acquire and double spin-echo with $G = 520$ mT/m. Black: interleaved double spin-echo with and without bipolar gradients. The scatter of the last time points of compartments 2 and 3 is due to a very low signal level.

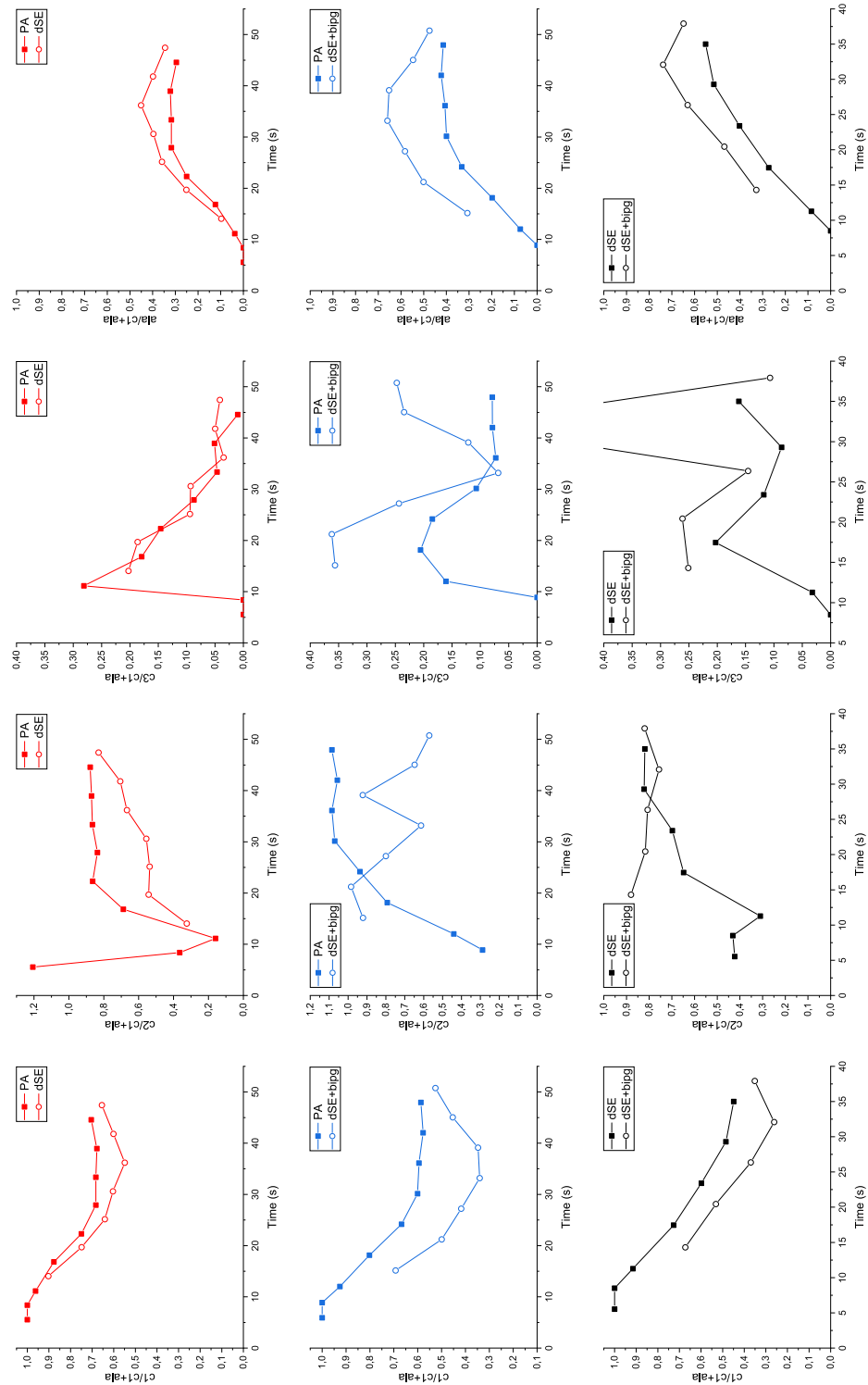


Figure B.6 – Metabolite ratios with respect to the sum of the amplitudes of alanine and alaninamide compartment 1 for a representative experiment. The datasets are obtained from three consecutive acquisitions following infusion of hyperpolarized L-[1-¹³C]alaninamide. Red: interleaved pulse-acquire and double spin-echo with $G = 0$ mT/m. Blue: interleaved pulse-acquire and double spin-echo with $G = 520$ mT/m. Black: interleaved double spin-echo with and without bipolar gradients. The scatter of the last time points of compartments 2 and 3 is due to a very low signal level.

Hyperpolarized [1-¹³C]glycinamide in the heart

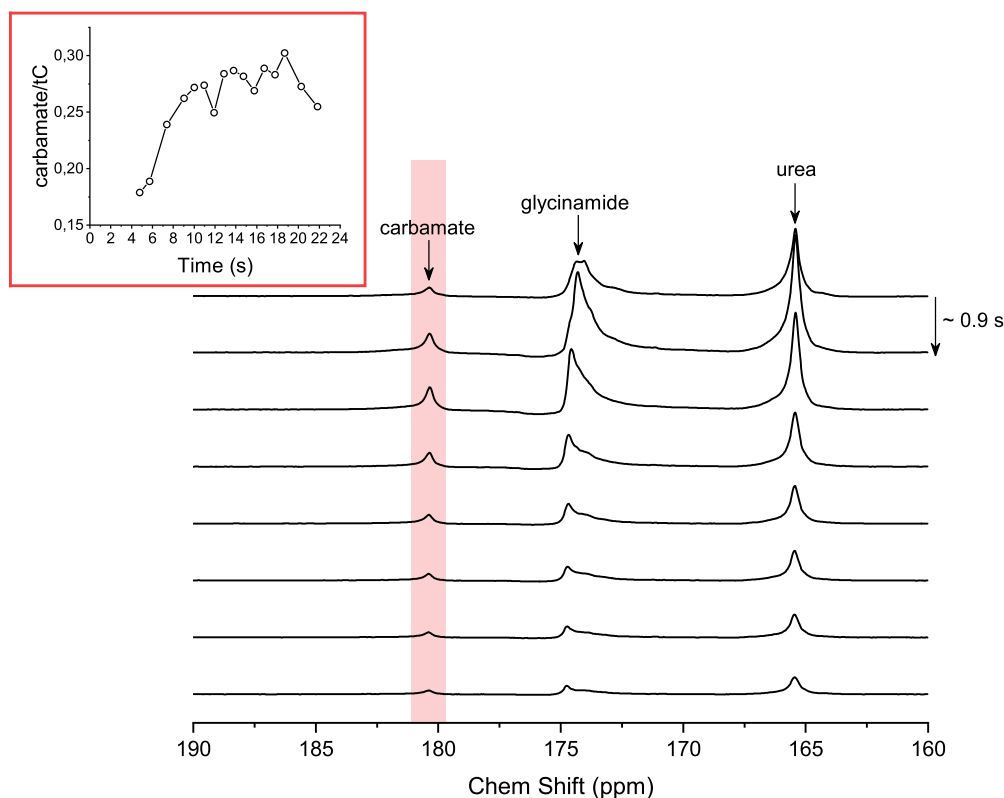


Figure B.7 – Timecourse of hyperpolarized [1-¹³C]glycinamide in the rat heart. Production of the carbamate adduct at 180.37 ppm, and, to some extent, a pH dependence of the glycinamide peak, is observed. The timecourse of the carbamate-to-total carbon ratio is shown in the inset.

A representative experiment with hyperpolarized [1-¹³C]glycinamide was performed by applying a similar protocol to the one developed for alaninamide. Briefly, 10 μ L of [1-¹³C]glycinamide and 1 μ L ¹³C urea solutions doped with 25 mM OX063 were hyperpolarized at 7 T, 1 K for about 2 h. The sample was then rapidly dissolved and transferred to a 9.4 T animal scanner, where it was injected through the tail vein of a Wistar rat over 9 s. ¹H-decoupled ¹³C FIDs were acquired on the heart by using a single-loop ¹H, quadrature ¹³C coil by applying 30° BIR4 pulses every ~0.9 s. For more details the reader is referred to Section 6.2.

Formation of the carbamate adduct is observed with glycinamide as well, with a peak appearing at 180.37 ppm. At equilibrium, a carbamate-to-total carbon ratio of 0.28 was measured, about a factor 10 greater than that obtained with alaninamide. This would agree with the lower glycinamide pK_a and the absence of steric effects and suggests that glycinamide would make a more sensitive probe for blood CO₂.

C Flow suppression experiments with hyperpolarized [1-¹³C]pyruvate: proof of concept

The *in vivo* performance of the flow-suppression scheme was initially tested on the rat kidney using hyperpolarized [1-¹³C]pyruvate as substrate, as the localization of the enzymes that catalyze its conversion to downstream metabolites is well known.

The experiments were performed by hyperpolarizing 10 μ L [1-¹³C]pyruvic acid doped with 21 mM trityl OX063 at 7 T, 1 K. 1 molar equivalent of frozen pellets of NaOH was added to the sample cup to ensure neutralization upon dissolution. 1.4 mL of the dissolved solution was then injected into the rat's femoral vein over 9 s. The same acquisition scheme used for alanine involving interleaved pulse-acquire, double spin-echo and double spin-echo with bipolar gradients was adopted (for further details see 6.2.7), and the hyperpolarized signal was measured on the left kidney. The experiment was repeated on three animals.

Upon infusion of hyperpolarized pyruvate, metabolic conversion to lactate C1 at 185.1 ppm, alanine C1 at 178.48 ppm and aspartate C1, C4 at 176.9 and 180.2 ppm, respectively was observed. Traces of malate C1, C4 were also detected at 183.58 and 182.51 ppm, respectively. A representative timecourse of the acquired spectra for an interleaved pulse-acquire and double spin-echo with gradients ON is shown in Figure C.1.

Figure C.2, C.3 and C.4 show the metabolite ratios of lactate-, alanine- and pyruvate hydrate-to-pyruvate as a function of time for the different acquisition schemes, each figure representing one experiment. Both lactate-to-pyruvate and alanine-to-pyruvate ratios were found to be consistently higher when comparing double spin-echo with gradients ON/OFF, indicating that the two metabolites have a lower mobility than pyruvate. This would be in agreement with them being primarily located intracellularly. Higher ratios were also observed when comparing pulse-acquire with double spin-echo with both gradients ON and OFF. In addition to mobility/diffusion during the TE delay, this could also be due to differences in T_2 between metabolites²⁰¹. As a reference, the pyruvate hydrate-to-pyruvate ratio is also re-

Appendix C. Flow suppression experiments with hyperpolarized [1-¹³C]pyruvate: proof of concept

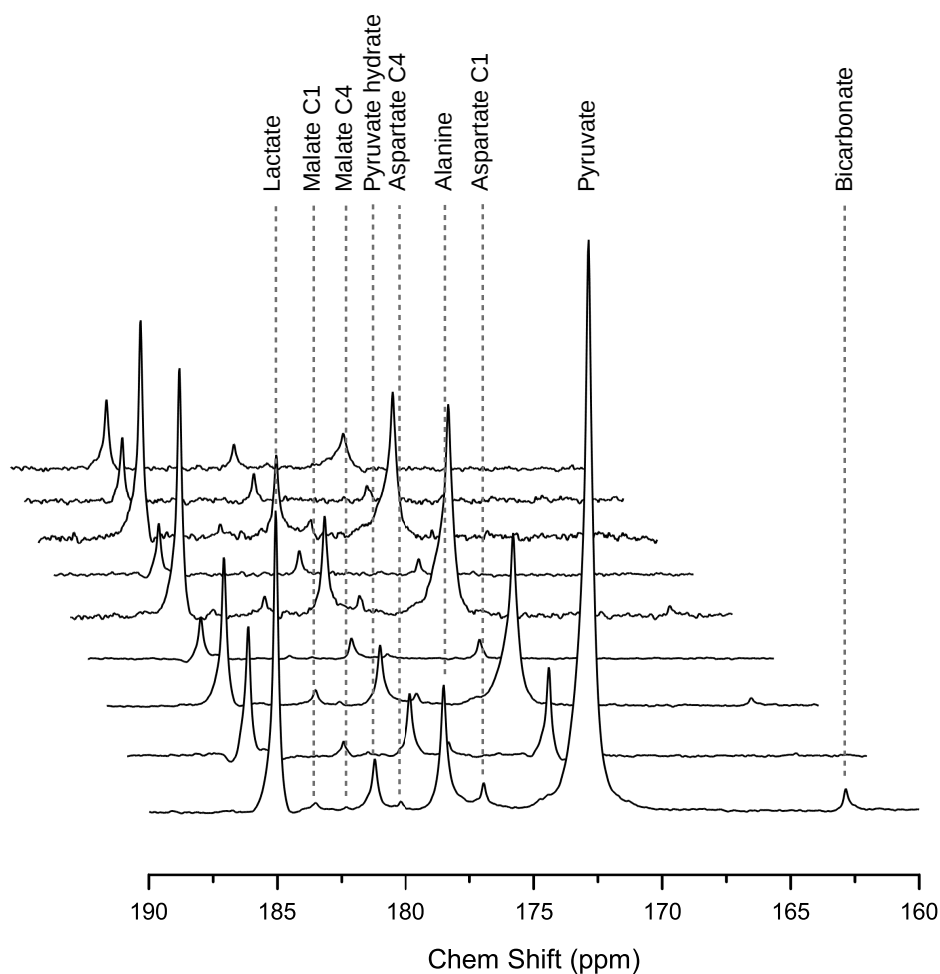


Figure C.1 – Representative stack of spectra acquired after a bolus injection of hyperpolarized [1-¹³C]pyruvate over the left kidney. Acquisition scheme: pulse-acquire interleaved with double spin-echo, gradients ON.

ported. The two compounds are expected to be in the same compartment, and therefore be affected in a similar fashion by the bipolar gradients. This is indeed what was observed: when comparing the double spin-echo with gradients ON/OFF, no differences in the pyruvate hydrate-to-pyruvate ratio were observed over time.

These results overall suggest that the implemented acquisition scheme can be successfully employed to selectively suppress the signal of flowing spins.

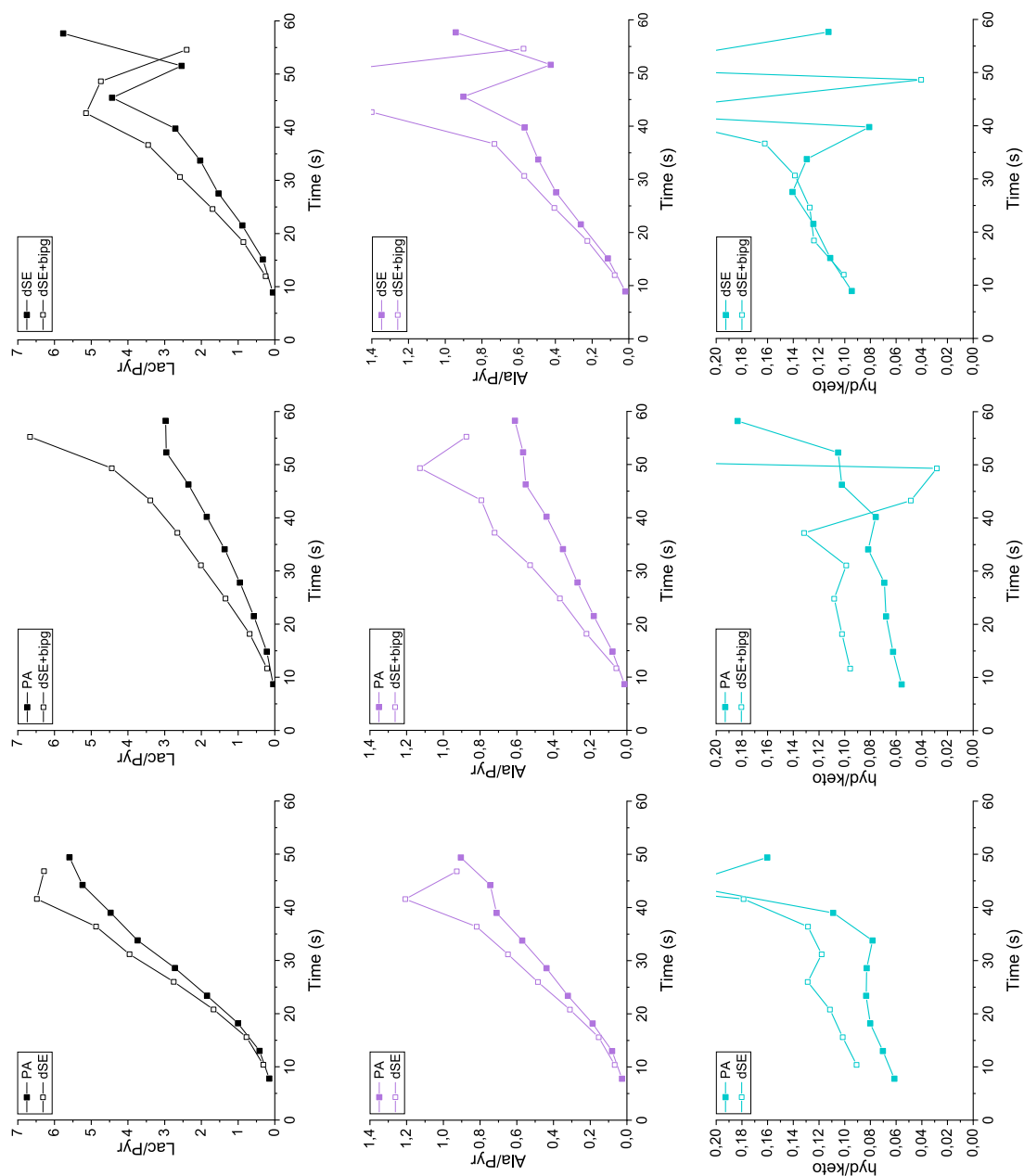


Figure C.2 – Metabolite ratios with respect to pyruvate for a representative experiment. The datasets are obtained from three consecutive acquisitions following infusion of hyperpolarized L-[1-¹³C]pyruvate. Black: lactate-to-pyruvate ratio. Purple: alanine-to-pyruvate ratio. Blue: pyruvate hydrate-to-keto ratio. The scatter of the later time points is due to the low signal level.

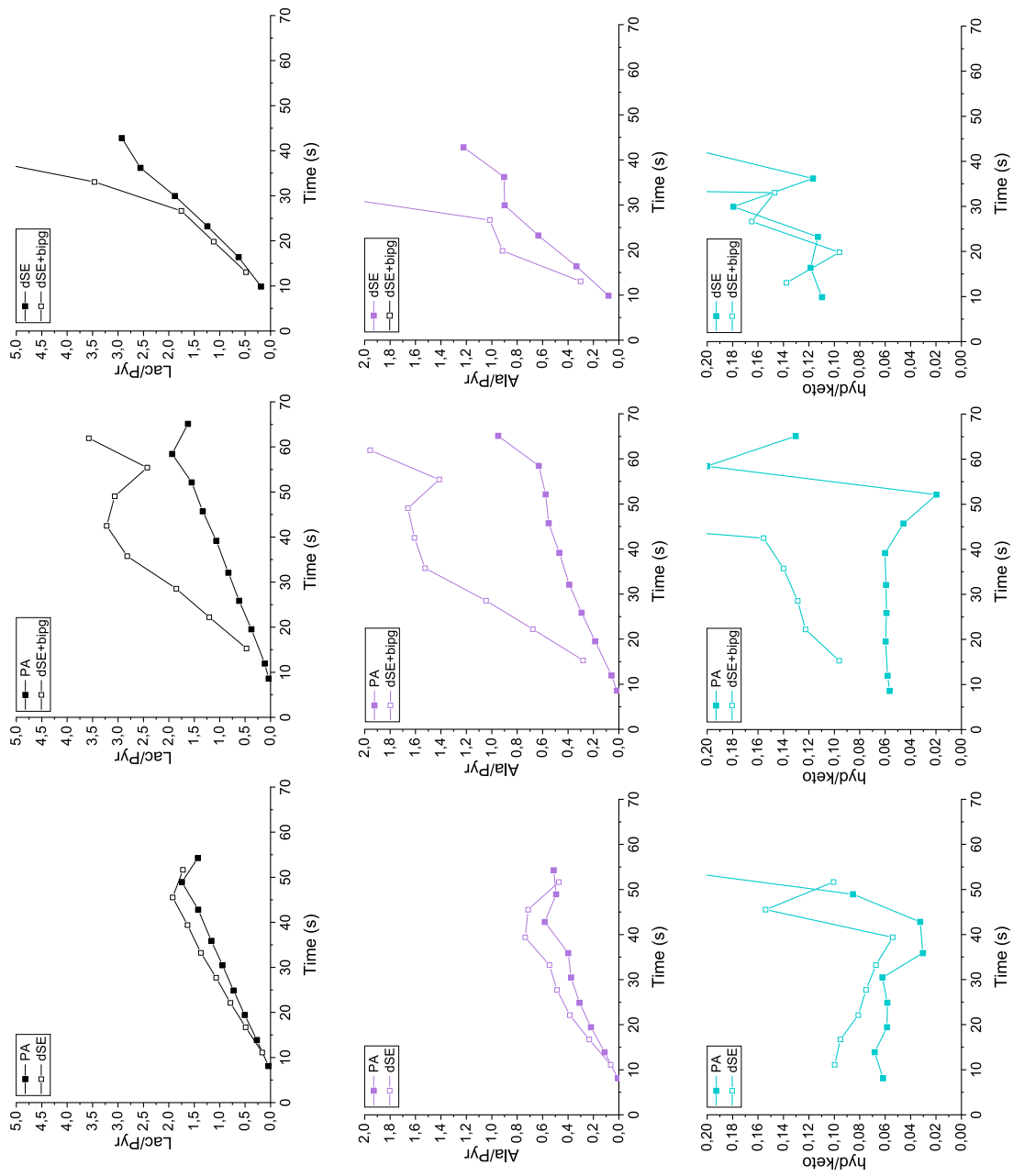


Figure C.3 – Metabolite ratios with respect to pyruvate for a representative experiment. The datasets are obtained from three consecutive acquisitions following infusion of hyperpolarized L-[1-¹³C]pyruvate. Black: lactate-to-pyruvate ratio. Purple: alanine-to-pyruvate ratio. Blue: pyruvate hydrate-to-keto ratio. The scatter of the later time points is due to the low signal level.

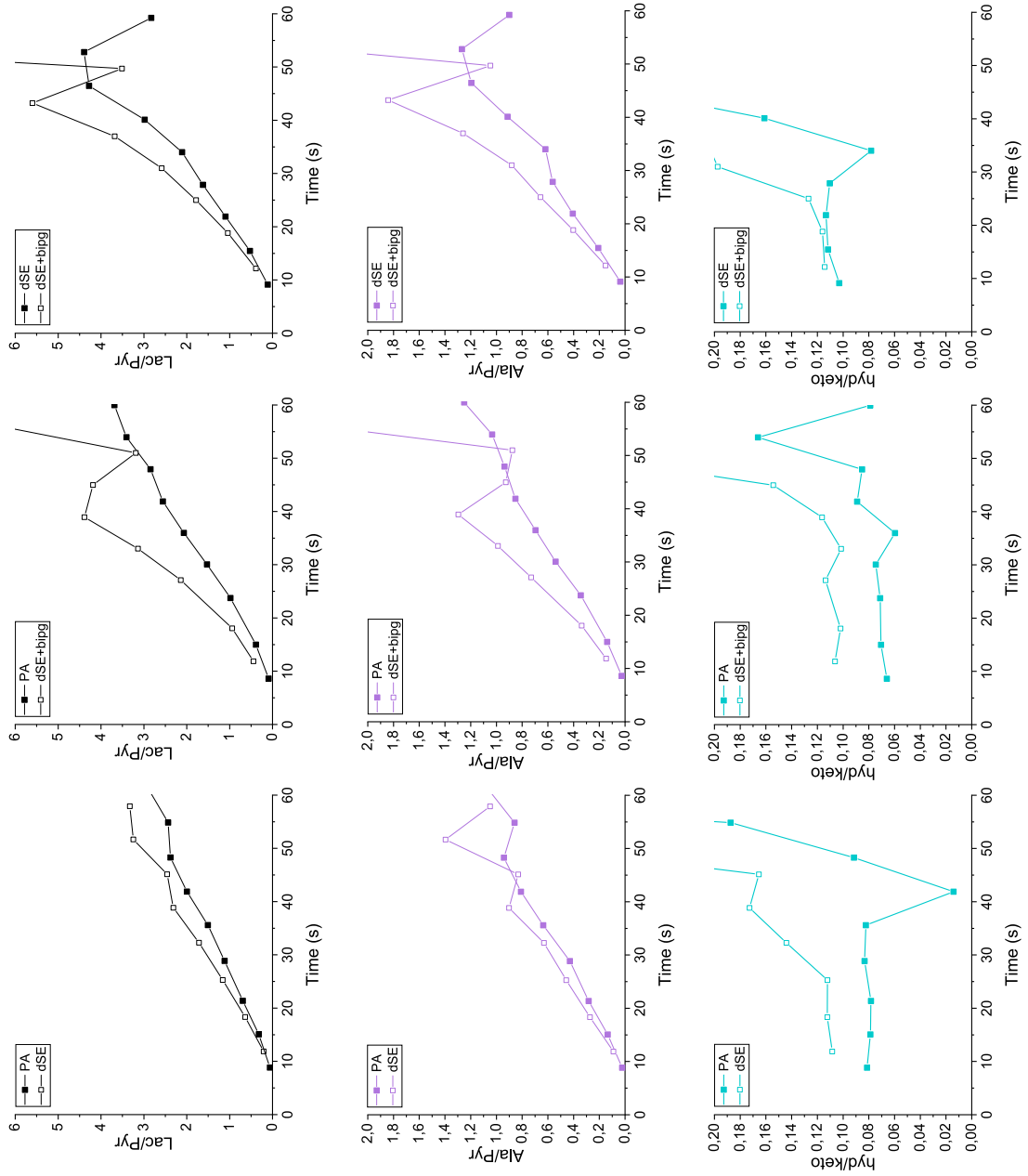


Figure C.4 – Metabolite ratios with respect to pyruvate for a representative experiment. The datasets are obtained from three consecutive acquisitions following infusion of hyperpolarized L-[1-¹³C]pyruvate. Black: lactate-to-pyruvate ratio. Purple: alanine-to-pyruvate ratio. Blue: pyruvate hydrate-to-keto ratio. The scatter of the later time points is due to the low signal level.

D Comparison of hyperpolarized ^{13}C 2D-CSI images over the left and right kidney

The 2D-CSI sequence was tested *in vivo* over the rat kidney upon infusion of hyperpolarized pyruvate.

30 μL of $[1-^{13}\text{C}]$ pyruvic acid doped with 21 mM trityl OX063 were hyperpolarized at 7 T, 1 K. 1 molar equivalent of frozen pellets NaOH was added to the sample cup to ensure neutralization upon dissolution. After dissolution, 1.4 mL of the hyperpolarized solution were injected through the rat's femoral vein over 9 s. The 2D-CSI sequence was run using the same protocol and parameters as described in Section 6.2.7, with the one difference being the nominal flip angle set to 18° . The same experiment was performed over the left and right kidney of the animal.

On the left side, a consistent contribution of the spleen to the total pyruvate and lactate signal was observed. This was likely due to the proximity of the organ to the coil. Alanine was instead mostly localized in the kidney. On the right side, on the other hand, the pyruvate signal originated from the kidney. The lactate signal was not perfectly centered on the kidney (nor was that of alanine, where the mismatch was more pronounced), and signal from the side of the liver side was observed. The hypothesis of the liver contributing to the signal was further supported by the fact that in this region the intensity of the lactate and alanine peaks was roughly equal, which is usually observed in spectroscopic data collected in this organ.

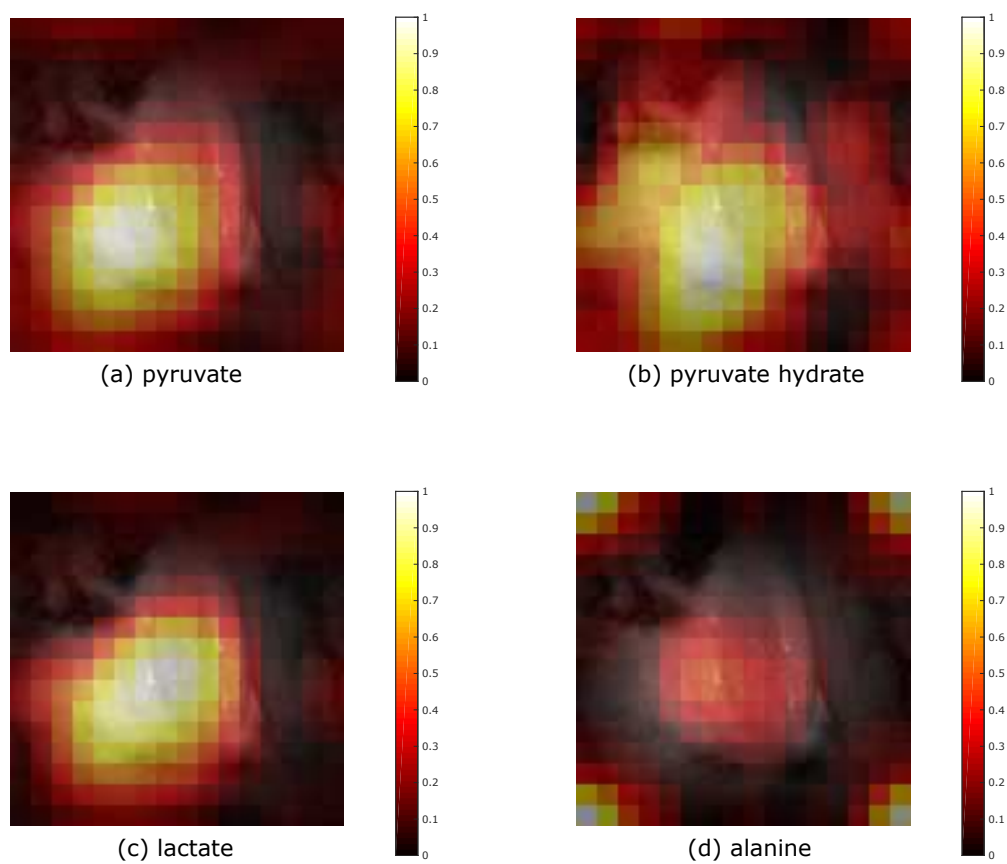


Figure D.1 – Metabolite maps acquired after a bolus injection of hyperpolarized $[1-^{13}\text{C}]$ pyruvate over the left kidney of the animal.

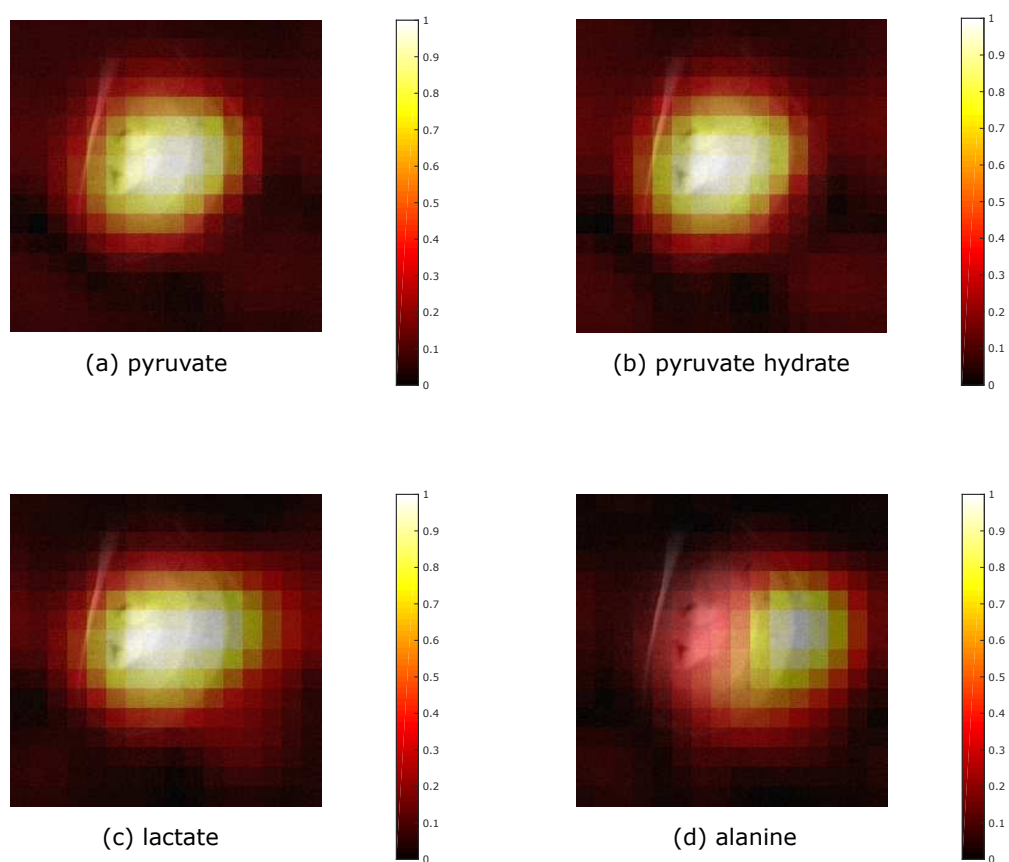


Figure D.2 – Metabolite maps acquired after a bolus injection of hyperpolarized $[1-^{13}\text{C}]$ pyruvate over the right kidney of the animal.

E *In vivo* detection of D-amino acid oxidase with hyperpolarized D-[1-¹³C]alanine

Chiral purity of the D- and L-alanine sample preparations

(*S,R*)-1-benzotriazol-1-yl-3,3,3-trifluoro-2-methoxy-2-phenylpropan-1-one (Mosher-Bt) was synthesized following the procedure described by Katritzky *et al.*¹⁷⁹ 15 μ L of either the D or the L sample preparations used in the hyperpolarized experiments were dissolved in 1.5 mL of an acetonitrile:H₂O solution (2:1 v/v). 15 mg of the Mosher-Bt reagent were added to the solution, together with 17.9 μ L of N,N-diisopropylethylamine. The reaction was left stirring at room temperature for 48 h, then the solvent was evaporated. The residue was dissolved in ethyl acetate (15 mL), washed with HCl (7.6 M, 3 mL) and dried with MgSO₄. Filtration through celite and rotary evaporation yielded the crude reaction product containing some residual 1*H*-benzotriazole.

¹H and ¹⁹F NMR spectra of the reactions products dissolved in CDCl₃ were acquired on a Bruker 400 MHz vertical scanner equipped with a standard BBFO_z coil. ¹H NMR spectra of the Mosher amides of D- and L-alanine are displayed in Figure E.1 and E.2 respectively. The chiral purity of the sample preparations was then evaluated by calculating the ratio between the integrals of the methoxy peaks of the *S,R* and *S,S* diastereomers in the ¹H spectrum.

The enantiomeric purity of the D- and L-[1-¹³C]alanine sample preparations was determined to be greater than 99 % in both cases (Figure E.1,E.2).

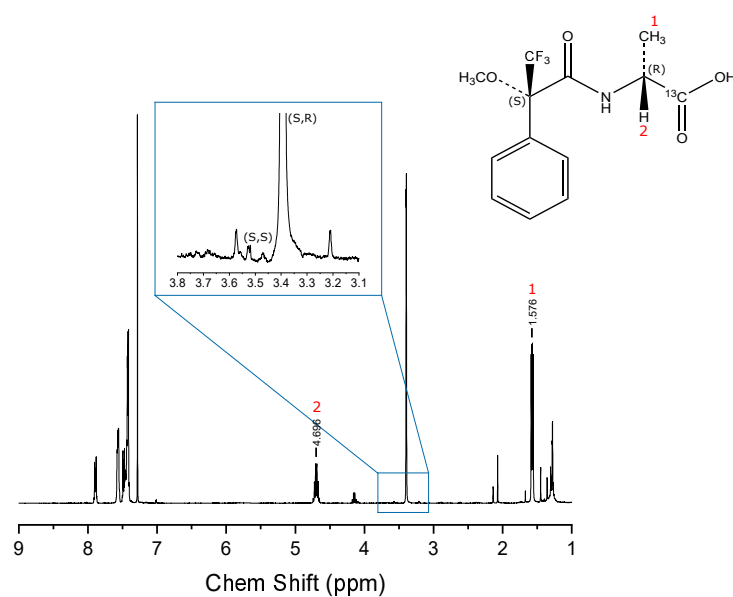


Figure E.1 – ^1H NMR spectrum of ((S)-3,3,3-trifluoro-2-methoxy-2-phenylpropanoyl)-D-alanine-1- ^{13}C . In the inset, the region around 3.5 ppm, where the methoxy protons of the compound resonate, is magnified and the peaks corresponding to the two diastereomers can be observed.

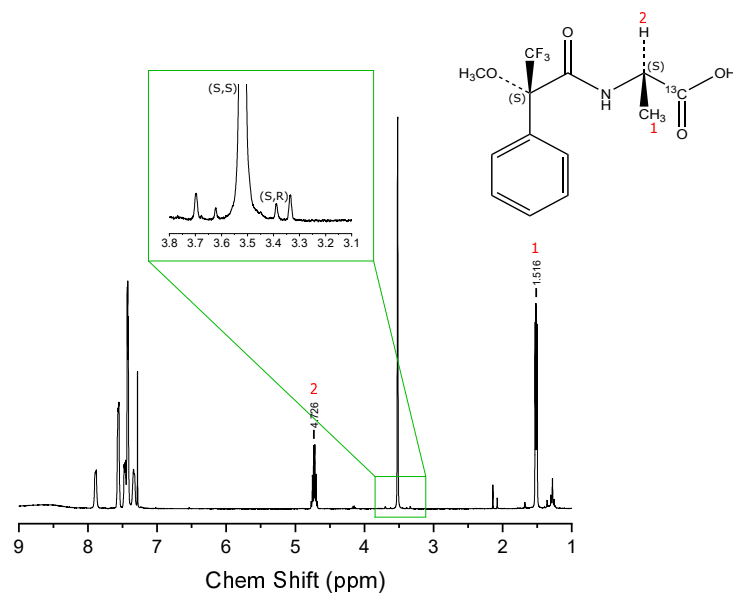


Figure E.2 – ^1H NMR spectrum of ((S)-3,3,3-trifluoro-2-methoxy-2-phenylpropanoyl)-L-alanine-1- ^{13}C . In the inset, the region around 3.5 ppm, where the methoxy protons of the compound resonate, is magnified and the peaks corresponding to the two diastereomers can be observed.

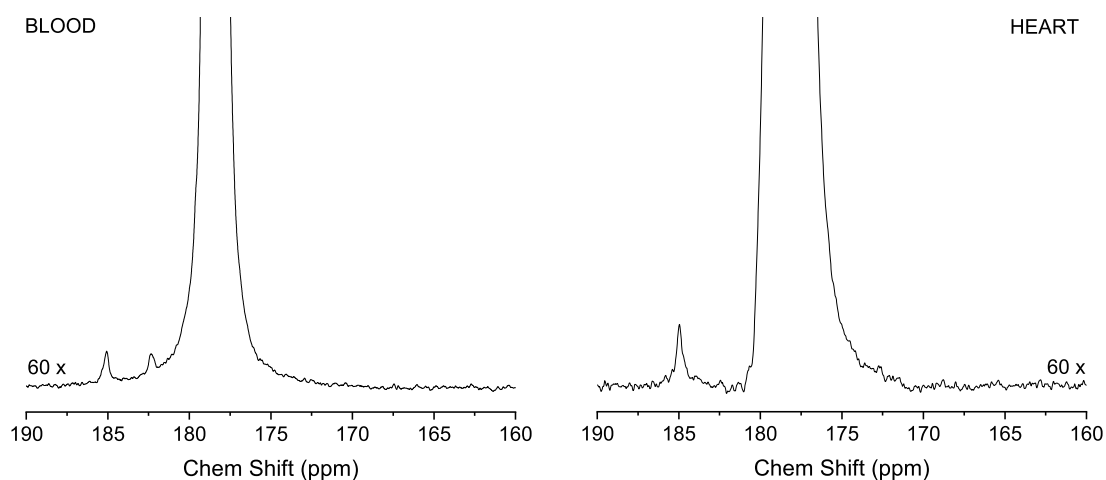
***In vivo* and *in vitro* experiments**

Figure E.3 – Left: sum of the spectra acquired after a bolus injection of L-[1- ^{13}C]alanine in blood. Lactate C1 is visible at 185.10 ppm, whereas the peak at 182.38 ppm could not be identified. Right: sum of the spectra acquired *in vivo* over the rat heart following a bolus injection of L-[1- ^{13}C]alanine. Again, lactate was the only observed metabolite.

References

- [1] Ardenkjaer-Larsen JH, Fridlund B, Gram A, et al. Increase in signal-to-noise ratio of >10,000 times in liquid-state NMR. 100:10158, 2003.
- [2] Brewer W and Kopp M. Brute-force nuclear orientation. *Hyperfine Interact*, 2(2):299–305, 1976.
- [3] Walker TG. Fundamentals of spin-exchange optical pumping. In *Journal of Physics: Conference Series*, volume 294, page 012001. IOP Publishing, 2011.
- [4] Duckett SB and Mewis RE. Application of parahydrogen induced polarization techniques in NMR spectroscopy and imaging. *Acc Chem Res*, 45(8):1247–1257, 2012.
- [5] Adams RW, Aguilar JA, Atkinson KD, et al. Reversible interactions with para-hydrogen enhance NMR sensitivity by polarization transfer. *Science*, 323(5922):1708–1711, 2009.
- [6] Overhauser AW. Polarization of nuclei in metals. 91:476, 1953.
- [7] Carver TR and Slichter CP. Polarization of nuclei in metals. 91:212, 1953.
- [8] Jeffries CD. Polarization of nuclei by resonance saturation in paramagnetic crystals. 106:164, 1957.
- [9] Abragam A and Proctor GW. Une nouvelle méthode de polarisation dynamique des noyaux atomiques dans les solides, 1958.
- [10] Borghini M. Nuclear spin relaxation and dynamic polarization versus electron spin relaxation. 26:242, 1968.
- [11] Comment A and Merritt ME. Hyperpolarized magnetic resonance as a sensitive detector of metabolic function. *Biochemistry*, 53(47):7333–7357, 2014.
- [12] Golman K, Lerche M, Pehrson R, et al. Metabolic imaging by hyperpolarized ^{13}C magnetic resonance imaging for in vivo tumor diagnosis. *Cancer Res*, 66(22):10855–10860, 2006.
- [13] Nelson SJ, Kurhanewicz J, Vigneron DB, et al. Metabolic imaging of patients with prostate cancer using hyperpolarized $[1-^{13}\text{C}]$ pyruvate. *Sci Transl Med*, 5(198):198ra108, 2013.

References

- [14] *The Rate of Hyperpolarized [1-13C]pyruvate to [1-13C]lactate conversion distinguishes high-grade prostate cancer from low-grade prostate cancer and normal peripheral zone tissue in patients.* Proc. 26th International Conference on Magnetic Resonance in Medicine (Paris, France), 2018.
- [15] Golman K, Petersson JS, Magnusson P, et al. Cardiac metabolism measured noninvasively by hyperpolarized ¹³C MRI. *Magn Reson Med*, 59(5):1005, 2008.
- [16] Schroeder MA, Lau AZ, Chen AP, et al. Hyperpolarized ¹³C magnetic resonance reveals early- and late-onset changes to in vivo pyruvate metabolism in the failing heart. *Eur J Heart Fail*, 15(2):130, 2013.
- [17] Guglielmetti C, Najac C, Didonna A, Van der Linden A, Ronen SM, and Chaumeil MM. Hyperpolarized ¹³C MR metabolic imaging can detect neuroinflammation in vivo in a multiple sclerosis murine model. *Proc Natl Acad Sci U S A*, 114(33):E6982–E6991, 2017.
- [18] Guglielmetti C, Chou A, Krukowski K, et al. In vivo metabolic imaging of traumatic brain injury. *Sci Rep*, 7(1):1–10, 2017.
- [19] DeVience SJ, Lu X, Proctor J, et al. Metabolic imaging of energy metabolism in traumatic brain injury using hyperpolarized [1-¹³C]pyruvate. *Sci Rep*, 7(1):1–7, 2017.
- [20] Xu Y, Ringgaard S, Mariager CØ, et al. Hyperpolarized ¹³C magnetic resonance imaging can detect metabolic changes characteristic of penumbra in ischemic stroke. *Tomography*, 3(2):67, 2017.
- [21] Miller JJ, Grist JT, Serres S, et al. ¹³C pyruvate transport across the blood-brain barrier in preclinical hyperpolarised MRI. *Sci Rep*, 8(1):1–15, 2018.
- [22] Marjańska M, Shestov AA, Deelchand DK, Kittelson E, and Henry PG. Brain metabolism under different anesthetic conditions using hyperpolarized [1-¹³C]pyruvate and [2-¹³C]pyruvate. *NMR Biomed*, 31(12):e4012, 2018.
- [23] Ardenkjaer-Larsen JH. Introduction to dissolution DNP: overview, instrumentation, and human applications. *eMagRes*, pages 63–78, 2007.
- [24] Marjańska M, Iltis I, Shestov AA, et al. In vivo ¹³C spectroscopy in the rat brain using hyperpolarized [1-¹³C]pyruvate and [2-¹³C]pyruvate. *J Magn Reson*, 206(2):210–218, 2010.
- [25] Chen AP, Kurhanewicz J, Bok R, et al. Feasibility of using hyperpolarized [1-¹³C]lactate as a substrate for in vivo metabolic ¹³C MRSI studies. *Mag Reson Imaging*, 26(6):721–726, 2008.
- [26] Gallagher FA, Kettunen MI, Day SE, et al. Magnetic resonance imaging of pH in vivo using hyperpolarized ¹³C-labelled bicarbonate. 453:940, 2008.
- [27] Gallagher FA, Kettunen MI, Hu DE, et al. Production of hyperpolarized [1,4-¹³C₂]malate from [1,4-¹³C₂]fumarate is a marker of cell necrosis and treatment response in tumors. *Proc Natl Acad Sci U S A*, pages pnas–0911447106, 2009.

-
- [28] Clatworthy MR, Kettunen MI, Hu DE, et al. Magnetic resonance imaging with hyperpolarized [1,4- $^{13}\text{C}_2$]fumarate allows detection of early renal acute tubular necrosis. *Proc Natl Acad Sci U S A*, 109(33):13374, 2012.
- [29] Marco-Rius I, Cao P, von Morze C, et al. Multiband spectral-spatial RF excitation for hyperpolarized [2- ^{13}C]dihydroxyacetone ^{13}C -MR metabolism studies. *Mag Reson Med*, 77(4):1419–1428, 2017.
- [30] Keshari KR, Wilson DM, Chen AP, et al. Hyperpolarized [2- ^{13}C]fructose: a hemiketal DNP substrate for in vivo metabolic imaging. *J Am Chem Soc*, 131(48):17591–17596, 2009.
- [31] Canape C, Catanzaro G, Terreno E, Karlsson M, Lerche MH, and Jensen PR. Probing treatment response of glutaminolytic prostate cancer cells to natural drugs with hyperpolarized [5- ^{13}C]glutamine. *Mag Reson Med*, 73(6):2296–2305, 2015.
- [32] Hurd RE, Yen YF, Mayer D, et al. Metabolic imaging in the anesthetized rat brain using hyperpolarized [1- ^{13}C]pyruvate and [1- ^{13}C]ethyl pyruvate. *Mag Reson Med*, 63(5):1137–1143, 2010.
- [33] Mishkovsky M, Anderson B, Karlsson M, et al. Measuring glucose cerebral metabolism in the healthy mouse using hyperpolarized ^{13}C magnetic resonance. *Sci Rep*, 7(1):11719, 2017.
- [34] Bastiaansen J, Cheng T, Gruetter R, and Comment A. In vivo real time cardiac metabolism using hyperpolarized acetate. *Proc Intl Soc Mag Reson Med 2020*, 20(CONF):4324, 2012.
- [35] von Morze C, Larson PEZ, Hu S, et al. Imaging of blood flow using hyperpolarized [^{13}C]urea in preclinical cancer models. *J Magn Reson Imaging*, 33(3):692, 2011.
- [36] Grant AK, Vinogradov E, Wang X, Lenkinski RE, and Alsop DC. Perfusion imaging with a freely diffusible hyperpolarized contrast agent. *Mag Reson Med*, 66(3):746, 2011.
- [37] Butt SA, Sogaard LV, Magnusson PO, et al. Imaging cerebral 2-ketoisocaproate metabolism with hyperpolarized ^{13}C magnetic resonance spectroscopic imaging. *J Cereb Blood Flow Metab*, 32(8):1508–1514, 2012.
- [38] Bohndiek SE, Kettunen MI, Hu DE, et al. Hyperpolarized [1- ^{13}C]ascorbic and dehydroascorbic acid: vitamin C as a probe for imaging redox status in vivo. *J Am Chem Soc*, 133(30):11795–11801, 2011.
- [39] Park JM, Khemtong C, Liu SC, Hurd RE, and Spielman DM. In vivo assessment of intracellular redox state in rat liver using hyperpolarized [1- ^{13}C]alanine. *Mag Reson Med*, 77(5):1741–1748, 2017.
- [40] Park JM, Wu M, Datta K, et al. Hyperpolarized sodium [1- ^{13}C]glycerate as a probe for assessing glycolysis in vivo. *J Am Chem Soc*, 139(19):6629–6634, 2017.
- [41] Miller J, Ball DR, Lau AZ, and Tyler DJ. Hyperpolarized ketone body metabolism in the rat heart. *NMR Biomed*, 31(6):e3912, 2018.

References

- [42] Düwel S, Hundshammer C, Gersch M, et al. Imaging of pH in vivo using hyperpolarized ^{13}C -labelled zymonic acid. *Nature*, 8(1):1–9, 2017.
- [43] Yoshihara HAI, Bastiaansen JAM, Karlsson M, Lerche MH, Comment A, and Schwitter J. Detection of myocardial medium-chain fatty acid oxidation and tricarboxylic acid cycle activity with hyperpolarized $[1-^{13}\text{C}]$ octanoate. *NMR Biomed*, 33(3):e4243, 2020.
- [44] Nishihara T, Yoshihara HAI, Nonaka H, et al. Direct monitoring of γ -glutamyl transpeptidase activity in vivo using a hyperpolarized ^{13}C -labeled molecular probe. *Angew Chem Int Ed Engl*, 55(36):10626–10629, 2016.
- [45] Rodrigues TB, Serrao EM, Kennedy BWC, Hu DE, Kettunen MI, and Brindle KM. Magnetic resonance imaging of tumor glycolysis using hyperpolarized ^{13}C -labeled glucose. *Nat Med*, 20(1):93–97, 2014.
- [46] Korenchan DE, Flavell RR, Baligand C, et al. Dynamic nuclear polarization of biocompatible ^{13}C -enriched carbonates for in vivo pH imaging. *J Chem Soc Chem Commun*, 52(14):3030–3033, 2016.
- [47] Maptue N, Jiang W, Harrison C, et al. Esterase-catalyzed production of hyperpolarized ^{13}C -enriched carbon dioxide in tissues for measuring pH. *ACS Sens*, 3(11):2232–2236, 2018.
- [48] Hundshammer C, Düwel S, Köcher SS, et al. Deuteration of hyperpolarized ^{13}C -labeled zymonic acid enables sensitivity-enhanced dynamic MRI of pH. *Chemphyschem*, 18(18):2421–2421, 2017.
- [49] Schroeder MA, Cochlin LE, Heather LC, Clarke K, Radda GK, and Tyler DJ. In vivo assessment of pyruvate dehydrogenase flux in the heart using hyperpolarized carbon-13 magnetic resonance. *Proc Natl Acad Sci U S A*, 105(33):12051, 2008.
- [50] Lingwood MD, Siaw TA, Sailasuta N, et al. Hyperpolarized water as an MR imaging contrast agent: feasibility of in vivo imaging in a rat model. *Radiology*, 265(2):418–425, 2012.
- [51] Ardenkjaer-Larsen JH, Laustsen C, Bowen S, and Rizi R. Hyperpolarized H_2O MR angiography. *Mag Reson Med*, 71(1):50–56, 2014.
- [52] Wolber J, Ellner F, Fridlund B, et al. Generating highly polarized nuclear spins in solution using dynamic nuclear polarization. *Nucl Instrum Methods Phys Res A*, 526(1-2):173–181, 2004.
- [53] Colombo SS, Filibian M, Carretta P, Rosso A, and Tedoldi F. Relevance of electron spin dissipative processes to dynamic nuclear polarization via thermal mixing. *Phys Chem Chem Phys*, 16(2):753–764, 2014.
- [54] Guarin D, Marhabaie S, Rosso A, et al. Characterizing thermal mixing dynamic nuclear polarization via cross-talk between spin reservoirs. *J Phys Chem Lett*, 8(22):5531–5536, 2017.

-
- [55] Kundu K, Feintuch A, and Vega S. Theoretical aspects of the cross effect enhancement of nuclear polarization under static dynamic nuclear polarization conditions. *J Phys Chem Lett*, 10(8):1769–1778, 2019.
- [56] Wenckebach WTh. Spectral diffusion and dynamic nuclear polarization: Beyond the high temperature approximation. 284:104, 2017.
- [57] Wenckebach WTh. Dynamic nuclear polarization via thermal mixing: Beyond the high temperature approximation. 277:68, 2017.
- [58] Hovav Y, Feintuch A, and Vega S. Theoretical aspects of dynamic nuclear polarization in the solid state—spin temperature and thermal mixing. *Physical Chemistry Chemical Physics*, 15(1):188–203, 2013.
- [59] Karabanov A, Kwiatkowski G, Perotto CU, et al. Dynamic nuclear polarisation by thermal mixing: quantum theory and macroscopic simulations. *Phys Chem Chem Phys*, 18(43):30093–30104, 2016.
- [60] Wenckebach WTh. Dynamic nuclear polarization via the cross effect and thermal mixing: A. the role of triple spin flips. *J Magn Reson*, 299:124–134, 2019.
- [61] Wenckebach WTh. Dynamic nuclear polarization via the cross effect and thermal mixing: B. energy transport. *J of Magn Reson*, 299:151–167, 2019.
- [62] Abragam A and Goldman M. Principles of dynamic nuclear polarization. 41:397, 1978.
- [63] Provotorov BN. 41:1582, 1961.
- [64] Borghini M. Spin-temperature model of nuclear dynamic polarization using free radicals. *Phys Rev Lett*, 20(9):419, 1968.
- [65] Wenckebach WTh, Van den Heuvel GM, Hoogstraate H, Swanenburg TJB, and Poullis NJ. Experimental proof of the strong coupling between the electron spin-spin reservoir and a nuclear spin system in dilute paramagnetic crystals. 22:581, 1969.
- [66] Cox SFJ, Bouffard V, and Goldman M. The coupling of two nuclear Zeeman reservoirs by the electronic spin-spin reservoir. 6:L100, 1973.
- [67] Kurdzesau F, van den Brandt B, Comment A, et al. Dynamic nuclear polarization of small labelled molecules in frozen water–alcohol solutions. *J Phys D Appl Phys*, 41(15):155506, 2008.
- [68] Capozzi A. *Methods to hyperpolarize nuclear spins via dissolution and sublimation DNP at high magnetic field*. PhD thesis, École polytechnique fédérale de Lausanne, 2016.
- [69] Ardenkjaer-Larsen JH, Bowen S, Petersen JR, et al. Cryogen-free dissolution dynamic nuclear polarization polarizer operating at 3.35 T, 6.7 T and 10.1 T. 81(3):2184–2194, 2019.
- [70] Comment A, Van Den Brandt B, Uffmann K, et al. Principles of operation of a DNP pre-polarizer coupled to a MRI rodent scanner. *Appl Magn Reson*, 34(3-4):313–319, 2008.

References

- [71] Comment A, van den Brandt B, Uffmann K, et al. Design and performance of a DNP prepolarizer coupled to a rodent MRI scanner. *Concepts Magn Reson Part B Magn Reson Eng*, 31(4):255–269, 2007.
- [72] Baudin M, Vuichoud B, Bornet A, Bodenhausen G, and Jannin S. A cryogen-consumption-free system for dynamic nuclear polarization at 9.4 T. 294:115, 2018.
- [73] Kiswandhi A, Niedbalski P, Parish C, Wang Q, and Lumata L. Assembly and performance of a 6.4 T cryogen-free dynamic nuclear polarization system. *Magn Reson Chem*, 55(9):846, 2017.
- [74] Cheng T, Gaunt AP, Marco-Rius I, et al. A multisample 7 T dynamic nuclear polarization polarizer for preclinical hyperpolarized MR. *NMR Biomed*, 33(5):e4264, 2020.
- [75] Ardenkjaer-Larsen JH, Leach AM, Clarke N, Urbahn J, Anderson D, and Skloss TW. Dynamic nuclear polarization polarizer for sterile use intent. *NMR Biomed*, 24:927, 2011.
- [76] Malinowski RM, Lipsø KW, Lerche MH, and Ardenkjær-Larsen JH. Dissolution dynamic nuclear polarization capability study with fluid path. *J Magn Reson*, 272:141, 2016.
- [77] Adeva B, Arik E, Ahmad S, et al. Large enhancement of deuteron polarization with frequency modulated microwaves. *Nucl Instrum Methods Phys Res A*, 372(3):339–343, April 1996.
- [78] Hovav Y, Feintuch A, Vega S, and Goldfarb D. Dynamic nuclear polarization using frequency modulation at 3.34 T. *J Magn Reson*, 238:94–105, 2014.
- [79] Bornet A, Milani J, Vuichoud B, Linde AJP, Bodenhausen G, and Jannin S. Microwave frequency modulation to enhance dissolution dynamic nuclear polarization. *Chem Phys Lett*, 602:63–67, 2014.
- [80] Granwehr J, Leggett J, and Köckenberger W. A low-cost implementation of EPR detection in a dissolution DNP setup. *J Magn Reson*, 187(2):266–276, 2007.
- [81] Capozzi A, Karlsson M, Petersen JR, Lerche MH, and Ardenkjaer-Larsen JH. Liquid-state ^{13}C polarization of 30% through photoinduced nonpersistent radicals. *J Phys Chem C*, 122(13):7432–7443, 2018.
- [82] Farrar CT, Hall DA, Gerfen GJ, Inati SJ, and Griffin RG. Mechanism of dynamic nuclear polarization in high magnetic fields. *J Chem Phys*, 114(11):4922–4933, 2001.
- [83] Yoshihara HAI, Can E, Karlsson M, Lerche MH, Schwitter J, and Comment A. High-field dissolution dynamic nuclear polarization of $[1-^{13}\text{C}]$ pyruvic acid. 18:12409, 2016.
- [84] Lumata L, Ratnakar SJ, Jindal A, et al. BDPA: an efficient polarizing agent for fast dissolution dynamic nuclear polarization NMR spectroscopy. *Chemistry*, 17(39):10825–10827, 2011.
- [85] Miéville P, Ahuja P, Sarkar R, et al. Scavenging free radicals to preserve enhancement and extend relaxation times in NMR using dynamic nuclear polarization. *Angew Chem Int Ed Engl*, 49(35):6182–6185, 2010.

- [86] Eichhorn TR, Takado Y, Salameh N, et al. Hyperpolarization without persistent radicals for in vivo real-time metabolic imaging. *Proc Natl Acad Sci U S A*, page 201314928, 2013.
- [87] Capozzi A, Cheng T, Boero G, Roussel C, and Comment A. Thermal annihilation of photo-induced radicals following dynamic nuclear polarization to produce transportable frozen hyperpolarized ^{13}C -substrates. *Nature Comm.*, 8:15757, 2017.
- [88] Lumata L, Merritt ME, and Kovacs Z. Influence of deuteration in the glassing matrix on ^{13}C dynamic nuclear polarization. *Phys Chem Chem Phys*, 15(19):7032–7035, 2013.
- [89] Kiswandhi A, Lama B, Niedbalski P, Goderya M, Long J, and Lumata L. The effect of glassing solvent deuteration and Gd^{3+} doping on ^{13}C DNP at 5 T. *RSC Adv*, 6(45):38855–38860, 2016.
- [90] Lumata L, Merritt ME, Malloy CR, Sherry AD, and Kovacs Z. Impact of Gd^{3+} on DNP of $[1-^{13}\text{C}]$ pyruvate doped with trityl OX063, BDPA, or 4-oxo-TEMPO. *J Phys Chem A*, 116(21):5129–5138, 2012.
- [91] Capozzi A, Patel S, Wenckebach WTh, Karlsson M, Lerche MH, and Ardenkjær-Larsen JH. Gadolinium effect at high-magnetic-field DNP: 70% ^{13}C polarization of $[\text{U}-^{13}\text{C}]$ glucose using trityl. *J Phys Chem Lett*, 10(12):3420–3425, 2019.
- [92] Karlsson M, Jensen PR, Duus JØ, Meier S, and Lerche MH. Development of dissolution DNP-MR substrates for metabolic research. *Appl Magn Reson*, 43:223, 2012.
- [93] Katsikis S, , Marin-Montesinos I, Pons M, Ludwig C, and Günther UL. Improved stability and spectral quality in ex situ dissolution DNP using an improved transfer device. *Appl Magn Reson*, 46:723, 2015.
- [94] Haze O, Corzilius B, Smith AA, Griffin RG, and Swager TM. Water-soluble narrow-line radicals for dynamic nuclear polarization. *J Am Chem Soc*, 134(35):14287–14290, 2012.
- [95] Michaelis VK, Smith AA, Corzilius B, Haze O, Swager TM, and Griffin RG. High-field ^{13}C dynamic nuclear polarization with a radical mixture. *J Am Chem Soc*, 135(8):2935–2938, 2013.
- [96] Can TV, Walish JJ, Swager TM, and Griffin RG. Time domain DNP with the NOVEL sequence. *J Chem Phys*, 143(5):054201, 2015.
- [97] Can TV, Caporini MA, Mentink-Vigier F, et al. Overhauser effects in insulating solids. *J Chem Phys*, 141(6):064202, 2014.
- [98] Smith AA, Corzilius B, O Haze, Swager TM, and Griffin RG. Observation of strongly forbidden solid effect dynamic nuclear polarization transitions via electron-electron double resonance detected NMR. *J Chem Phys*, 139(21):214201, 2013.
- [99] Lumata L, Kovacs Z, Sherry AD, et al. Electron spin resonance studies of trityl OX063 at a concentration optimal for DNP. *Phys Chem Chem Phys*, 15(24):9800–9807, 2013.

References

- [100] Walker SA, Edwards DT, Siaw TA, Armstrong BD, and Han SI. Temperature dependence of high field ^{13}C dynamic nuclear polarization processes with trityl radicals below 35 kelvin. *Phys Chem Chem Phys*, 15(36):15106–15120, 2013.
- [101] Schmugge TJ and Jeffries CD. High dynamic polarization of protons. *Phys Rev*, 138(6A):A1785, 1965.
- [102] Wenckebach WTh. *Essentials of dynamic nuclear polarization*. 2016.
- [103] de Boer W. Dynamic orientation of nuclei at low temperatures. *J Low Temp Phys*, 22(1-2):185–212, 1976.
- [104] Kundu K, Feintuch A, and Vega S. Electron–electron cross-relaxation and spectral diffusion during dynamic nuclear polarization experiments on solids. *J Phys Chem Lett*, 9(7):1793–1802, 2018.
- [105] Niinikoski TO. *The Physics of Polarized Targets*. Cambridge University Press, 2020.
- [106] Muñoz-Gómez JL, Monteagudo E, Lloveras V, Parella T, Veciana J, and Vidal-Gancedo J. A benzyl alcohol derivative of the BDPA radical for fast dissolution dynamic nuclear polarization NMR spectroscopy. *Org Biomol Chem*, 13(9):2689–2693, 2015.
- [107] Muñoz-Gómez JL, Monteagudo E, Lloveras V, Parella T, Veciana J, and Vidal-Gancedo J. Optimized polarization build-up times in dissolution DNP-NMR using a benzyl amino derivative of BDPA. *RSC Adv*, 6(32):27077–27082, 2016.
- [108] Khattri RB, Sirusi AA, Suh EH, Kovacs Z, and Merritt ME. The influence of Ho^{3+} doping on ^{13}C DNP in the presence of BDPA. *Phys Chem Chem Phys*, 21(34):18629–18635, 2019.
- [109] Equbal A, Li Y, Tabassum T, and Han SI. Crossover from a Solid Effect to Thermal Mixing ^1H Dynamic Nuclear Polarization with Trityl-OX063. *J Phys Chem Lett*, 11(9):3718–3723, 2020.
- [110] Batel M, Däpp A, Hunkeler A, Meier BH, Kozerke S, and M Ernst. Cross-polarization for dissolution dynamic nuclear polarization. *Phys Chem Chem Phys*, 16(39):21407–21416, 2014.
- [111] Cheng T, Capozzi A, Takado Y, Balzan R, and Comment A. Over 35% liquid-state ^{13}C polarization obtained via dissolution dynamic nuclear polarization at 7 T and 1 K using ubiquitous nitroxyl radicals. *Phys Chem Chem Phys*, 15(48):20819–20822, 2013.
- [112] Jähnig F, Himmler A, Kwiatkowski G, et al. A spin-thermodynamic approach to characterize spin dynamics in TEMPO-based samples for dissolution DNP at 7 T field. *J Magn Reson*, 303:91–104, 2019.
- [113] Abragam A, Bouffard V, Roinel Y, and Roubeau P. A new polarized target material: 6LiD . *Journal de Physique Lettres*, 41(13):309–310, 1980.
- [114] Bültmann S, Crabb DG, Day DB, et al. A study of lithium deuteride as a material for a polarized target. *Nucl Instrum Methods Phys Res A*, 425(1-2):23–36, 1999.

-
- [115] Ball J, Baum G, Berglund P, et al. First results of the large COMPASS 6LiD polarized target. *Nucl Instrum Methods Phys Res A*, 498(1-3):101–111, 2003.
- [116] Wolf T, Kumar S, Singh H, et al. Endogenous dynamic nuclear polarization for natural abundance ^{17}O and lithium NMR in the bulk of inorganic solids. *Journal of the American Chemical Society*, 141(1):451–462, 2018.
- [117] Harchol A, Reuveni G, Ri V, et al. Endogenous dynamic nuclear polarization for sensitivity enhancement in solid-state NMR of electrode materials. *J Phys Chem C*, 124(13):7082–7090, 2020.
- [118] van Heeswijk RB, Uffmann K, Comment A, et al. Hyperpolarized lithium-6 as a sensor of nanomolar contrast agents. *Magn Reson Med*, 61(6):1489–1493, 2009.
- [119] Balzan R, Mishkovsky M, Simonenko Y, et al. Hyperpolarized ^6Li as a probe for hemoglobin oxygenation level. *Contrast Media Mol Imaging*, 11(1):41–46, 2016.
- [120] Flatt E, Radaelli A, Hyacinthe JN, et al. Exploring the potential of hyperpolarized ^6Li to study lithium biodistribution in the rat brain. Proc. of the 6th International Conference on Nuclear Hyperpolarization (HYP18), 2018.
- [121] Hyacinthe JN Lê TP and Capozzi A. Design and performance of a fluid path compatible with dDNP/LOD-ESR probe: how to improve the efficiency of a traditional polarizer. Manuscript in preparation.
- [122] Wenckebach WTh, Swanenburg TJB, and Poulis NJ. Thermodynamics of spin systems in paramagnetic crystals. *Phys Rep*, 14(5):181–255, 1974.
- [123] Pinon AC, Capozzi A, and Ardenkjær-Larsen JH. Hyperpolarized water through dissolution dynamic nuclear polarization with UV-generated radicals. *Commun Chem*, 3(1):1–9, 2020.
- [124] Slichter CP. *Principles of magnetic resonance*. Springer Science & Business Media, 2013.
- [125] Capozzi A, Roussel C, Comment A, and Hyacinthe JN. Optimal glass-forming solvent brings sublimation dynamic nuclear polarization to ^{129}Xe hyperpolarization biomedical imaging standards. *J Phys Chem C*, 119(9):5020–5025, 2015.
- [126] Goertz ST. The dynamic nuclear polarization process. *Nucl Instrum Methods Phys Res A*, 526(1-2):28–42, 2004.
- [127] Capozzi A, Hyacinthe JN, Cheng T, et al. Photoinduced nonpersistent radicals as polarizing agents for X-nuclei dissolution dynamic nuclear polarization. *J Phys Chem C*, 119(39):22632–22639, 2015.
- [128] Linde AJP, Bornet A, Milani J, et al. Cross polarization from ^1H to quadrupolar ^6Li nuclei for dissolution DNP. *Phys Chem Chem Phys*, 16(45):24813–24817, 2014.
- [129] Luan Y and Xu W. The structure and main functions of aminopeptidase N. *Curr Med Chem*, 14(6):639–647, 2007.

References

- [130] Pasqualini R, Koivunen E, Kain R, et al. Aminopeptidase N is a receptor for tumor-homing peptides and a target for inhibiting angiogenesis. *Cancer Res*, 60(3):722–727, 2000.
- [131] Wickström M, Larsson R, Nygren P, and Gullbo J. Aminopeptidase N (CD13) as a target for cancer chemotherapy. *Cancer Sci*, 102(3):501–508, 2011.
- [132] Hingorani DV, Yoo B, Bernstein AS, and Pagel MD. Detecting enzyme activities with exogenous MRI contrast agents. *Chemistry*, 20(32):9840–9850, 2014.
- [133] Hata R, Nonaka H, Takakusagi Y, Ichikawa K, and Sando S. Design of a hyperpolarized molecular probe for detection of aminopeptidase N activity. *Angew Chem Int Ed Engl*, 128(5):1797–1800, 2016.
- [134] Koeppen BM and Steinmetz PR. Basic mechanisms of urinary acidification. *Med Clin North Am*, 67(4):753–770, 1983.
- [135] Burke TJ, Malhotra D, and Shapiro JJ. Factors maintaining a pH gradient within the kidney: role of the vasculature architecture. *Kidney Int*, 56(5):1826–1837, 1999.
- [136] Alpern RJ and Chambers M. Cell pH in the rat proximal convoluted tubule. regulation by luminal and peritubular pH and sodium concentration. *J Clin Invest*, 78(2):502–510, 1986.
- [137] Adam WR, Koretsky AP, and Weiner MW. ³¹P-NMR in vivo measurement of renal intracellular pH: effects of acidosis and K⁺ depletion in rats. *Am J Physiol Renal Physiol*, 251(5):F904–F910, 1986.
- [138] Raghunand N, Howison C, Sherry AD, Zhang S, and Gillies RJ. Renal and systemic pH imaging by contrast-enhanced MRI. *Magn Reson Med*, 49(2):249–257, 2003.
- [139] Klocke RA. Carbon dioxide transport. *Compr Physiol*, pages 173–197, 2011.
- [140] Ferguson JKW and Roughton FJW. The direct chemical estimation of carbamino compounds of CO₂ with haemoglobin. *J Physiol*, 83(1):68, 1934.
- [141] Morrow JS, Matthew JB, Wittebort RJ, and Gurd FR. Carbon 13 resonances of ¹³CO₂ carbamino adducts of alpha and beta chains in human adult hemoglobin. *J Biol Chem*, 251(2):477–484, 1976.
- [142] Linthwaite VL, Janus JM, Brown AP, et al. The identification of carbon dioxide mediated protein post-translational modifications. *Natures*, 9(1):1–11, 2018.
- [143] Gallagher FA, Sladen H, Kettunen MI, et al. Carbonic anhydrase activity monitored in vivo by hyperpolarized ¹³C-magnetic resonance spectroscopy demonstrates its importance for pH regulation in tumors. *Cancer Res*, 75(19):4109–4118, 2015.
- [144] Michelotti A, Rodrigues F, and Roche M. Development and scale-up of stereoretentive α -deuteration of amines. *Org Process Res Dev*, 21(11):1741–1744, 2017.
- [145] Florini N, Arnaud GF, Kónya B, Zucchi C, and Pályi G. Synthesis of a water-soluble chiral NMR shift reagent:(S)-PDTA. *Tetrahedron Asymmetry*, 20(9):1036–1039, 2009.

-
- [146] Wishart DS, Feunang YD, Marcu A, et al. HMDB 4.0: the human metabolome database for 2018. *Nucleic Acids Res*, 46(D1):D608–D617, 2017.
- [147] Gordon JW, Niles DJ, Adamson EB, Johnson KM, and Fain SB. Application of flow sensitive gradients for improved measures of metabolism using hyperpolarized ^{13}C MRI. *Magn Reson Med*, 75(3):1242–1248, 2016.
- [148] Crane JC, Olson MP, and Nelson SJ. SIVIC: open-source, standards-based software for DICOM MR spectroscopy workflows. *Int J Biomed Imaging*, 2013, 2013.
- [149] Jardinaud F, Banisadr G, Noble F, et al. Ontogenic and adult whole body distribution of aminopeptidase N in rat investigated by in vitro autoradiography. *Biochimie*, 86(2):105–113, 2004.
- [150] Eisenbach GM, Weise M, and Stolte H. Amino acid reabsorption in the rat nephron. *Pflügers Arch Gesamte Physiol Menschen Tiere*, 357(1-2):63–76, 1975.
- [151] Silbernagl S. Renal transport of amino acids. *Klin Wochenschr*, 57(19):1009–1019, 1979.
- [152] Hundshammer C, Düwel S, Ruseckas D, et al. Hyperpolarized amino acid derivatives as multivalent magnetic resonance pH sensor molecules. *Sensors*, 18(2):600, 2018.
- [153] Teicher BA, Liu SD, Liu JT, Holden SA, and Herman TS. A carbonic anhydrase inhibitor as a potential modulator of cancer therapies. *Anticancer Res*, 13:1549–1556, 1993.
- [154] Lee H, Lee J, Joe E, et al. Flow-suppressed hyperpolarized ^{13}C chemical shift imaging using velocity-optimized bipolar gradient in mouse liver tumors at 9.4 T. *Magnetic resonance in medicine*, 78(5):1674–1682, 2017.
- [155] Kettunen MI, Kennedy BWC, Hu DE, and Brindle KM. Spin echo measurements of the extravasation and tumor cell uptake of hyperpolarized $[1-^{13}\text{C}]\text{lactate}$ and $[1-^{13}\text{C}]\text{pyruvate}$. *Magn Reson Med*, 70(5):1200–1209, 2013.
- [156] Maunsbach AB, Giebisch GH, and Stanton BA. Effects of flow rate on proximal tubule ultrastructure. *Am J Physiol Renal Physiol*, 253(3):F582–F587, 1987.
- [157] Foiret J, Zhang H, Ilovitsh T, Mahakian L, Tam S, and Ferrara KW. Ultrasound localization microscopy to image and assess microvasculature in a rat kidney. *Sci Rep*, 7(1):1–12, 2017.
- [158] Vaupel P, Ruppert H, and Hutten H. Splenic blood flow and intrasplenic flow distribution in rats. *Pflügers Arch Gesamte Physiol Menschen Tiere*, 369(3):193–201, 1977.
- [159] Romero CA, Cabral G, Knight RA, Ding G, Peterson EL, and Carretero OA. Noninvasive measurement of renal blood flow by magnetic resonance imaging in rats. *Am J Physiol Renal Physiol*, 314(1):F99–F106, 2018.
- [160] Young JD, Wolowyk MW, Jones SM, and Ellory JC. Red-cell amino acid transport. evidence for the presence of system ASC in mature human red blood cells. *Biochem J*, 216(2):349–357, 1983.

References

- [161] Guy RD, Razi MT, and Rabenstein DL. Measurement of rates of transport across erythrocyte membranes by ¹H nuclear magnetic resonance spectroscopy. *J Magn Reson*, 66(3):434–444, 1986.
- [162] Gallagher FA, Kettunen MI, Day SE, et al. Magnetic resonance imaging of pH in vivo using hyperpolarized ¹³C-labelled bicarbonate. *Nature*, 453(7197):940–943, 2008.
- [163] McCann N, Phan D, Wang X, et al. Kinetics and mechanism of carbamate formation from CO₂ (aq), carbonate species, and monoethanolamine in aqueous solution. *J Phys Chem A*, 113(17):5022–5029, 2009.
- [164] Ciftja AF, Hartono A, and Svendsen HF. Selection of amine amino acids salt systems for CO₂ capture. *Energy Procedia*, 37:1597–1604, 2013.
- [165] Myers TG and SD Nelson. Neuroactive carbamate adducts of beta-N-methylamino-L-alanine and ethylenediamine. detection and quantitation under physiological conditions by ¹³C NMR. *J Biol Chem*, 265(18):10193–10195, 1990.
- [166] DuBose TD, Pucacco LR, Seldin DW, et al. Direct determination of PCO₂ in the rat renal cortex. *J Clin Invest*, 62(2):338–348, 1978.
- [167] Ohide H, Miyoshi Y, Maruyama R, Hamase K, and Konno R. D-amino acid metabolism in mammals: biosynthesis, degradation and analytical aspects of the metabolic study. *J Chromatogr B Analyt Technol Biomed Life Sci*, 879(29):3162–3168, 2011.
- [168] Sasabe J, Suzuki M, Miyoshi Y, et al. Ischemic acute kidney injury perturbs homeostasis of serine enantiomers in the body fluid in mice: early detection of renal dysfunction using the ratio of serine enantiomers. *PloS one*, 9(1):e86504, 2014.
- [169] Verrall L, Burnet PWJ, Betts JF, and Harrison PJ. The neurobiology of D-amino acid oxidase and its involvement in schizophrenia. *Mol Psychiatry*, 15(2):122, 2010.
- [170] Sasabe J, Miyoshi Y, Suzuki M, et al. D-amino acid oxidase controls motoneuron degeneration through D-serine. *PNAS*, 109(2):627–632, 2012.
- [171] Kondori NR, Paul P, Robbins JP, et al. Focus on the role of D-serine and D-amino acid oxidase in amyotrophic lateral sclerosis/motor neuron disease (als). *Front Mol Biosci*, 5:8, 2018.
- [172] Lin CH, Yang HT, Chiu CC, and Lane HY. Blood levels of D-amino acid oxidase vs. D-amino acids in reflecting cognitive aging. *Sci Rep*, 7(1):14849, 2017.
- [173] Cline MJ and Lehrer RI. D-amino acid oxidase in leukocytes: a possible D-amino-acid-linked antimicrobial system. *Proc Natl Acad Sci U S A*, 62(3):756–763, 1969.
- [174] Robinson JM, Briggs RT, and Karnovsky MJ. Localization of D-amino acid oxidase on the cell surface of human polymorphonuclear leukocytes. *J Cell Biol*, 77(1):59–71, 1978.
- [175] Eckstein MR, Baehner RL, and Nathan DG. Amino acid oxidase of leukocytes in relation to H₂O₂-mediated bacterial killing. *J Clin Invest*, 50(9):1985–1991, 1971.

- [176] D'Aniello A, D'Onofrio G, Pischetola M, et al. Biological role of D-amino acid oxidase and D-aspartate oxidase. effects of D-amino acids. *J Biol Chem*, 268(36):26941–26949, 1993.
- [177] Hasegawa H, Shinohara Y, Akahane K, Hashimoto T, and Ichida K. Altered D-methionine kinetics in rats with renal impairment. *Amino acids*, 40(4):1205–1211, 2011.
- [178] Hasegawa H, Matsukawa T, Shinohara Y, Konno R, and Hashimoto T. Role of renal D-amino-acid oxidase in pharmacokinetics of D-leucine. *Am J Physiol Endocrinol Metab*, 287(1):E160–E165, 2004.
- [179] Katritzky A, Mohapatra PP, Fedoseyenko D, Duncton M, and Steel PJ. 1-Benzotriazol-1-yl-3,3,3-trifluoro-2-methoxy-2-phenylpropan-1-ones: Mosher-Bt reagents. *J Org Chem*, 72(11):4268–4271, 2007.
- [180] Jensen PR, Karlsson M, Meier S, Duus JØ, and Lerche MH. Hyperpolarized amino acids for in vivo assays of transaminase activity. *Chem Eur J*, 15(39):10010–10012, 2009.
- [181] Sparey T, Abeywickrema P, Almond S, et al. The discovery of fused pyrrole carboxylic acids as novel, potent D-amino acid oxidase (dao) inhibitors. *Bioorg Med Chem Lett*, 18(11):3386–3391, 2008.
- [182] McClelland GB, Khanna S, González GF, Butz CE, and Brooks GA. Peroxisomal membrane monocarboxylate transporters: evidence for a redox shuttle system? *Biochem Biophys Res Commun*, 304(1):130–135, 2003.
- [183] Baumgart E, Fahimi HD, Stich A, and Völkl A. L-lactate dehydrogenase a-and ab isoforms are bona fide peroxisomal enzymes in rat liver evidence for involvement in intraperoxisomal nadh reoxidation. *J Biol Chem*, 271(7):3846–3855, 1996.
- [184] DeRosa G and Swick R. Metabolic implications of the distribution of the alanine aminotransferase isoenzymes. *JBC*, 250(20):7961–7967, 1975.
- [185] Rosenhagen M and Segal S. Stereospecificity of amino acid uptake by rat and human kidney cortex slices. *Am J Physiol*, 227(4):843–847, 1974.
- [186] Jenssen H, Vorum H, Jørgensen KE, and Sheikh MI. Characteristics of D-alanine transport by luminal membrane vesicles from pars convoluta and pars recta of rabbit proximal tubule. *Biochim Biophys Acta Biomembr*, 942(2):262–270, 1988.
- [187] Chan AW, Perry SG, Burch HB, Fagioli S, Alvey TR, and Lowry OH. Distribution of two aminotransferases and D-amino acid oxidase within the nephron of young and adult rats. *J Histochem Cytochem*, 27(3):751–755, 1979.
- [188] Brachet P, Carreira S, and Puigserver S. Differential effect of sunflower seed oil on hepatic and renal D-amino acid oxidase in the rat. *Int J Biochem*, 23(11):1255–1260, 1991.
- [189] A. Dölle. Metabolism of D- and L-[13C] alanine in rat liver detected by 1h and 13c nmr spectroscopy in vivo and in vitro. *NMR Biomed*, 13(2):72–81, 2000.

References

- [190] Yang RZ, Park S, Reagan WJ, et al. Alanine aminotransferase isoenzymes: molecular cloning and quantitative analysis of tissue expression in rats and serum elevation in liver toxicity. *Hepatology*, 49(2):598–607, 2009.
- [191] Gaunt GL and De Duve C. Subcellular distribution of D-amino acid oxidase and catalase in rat brain. *J Neurochem*, 26(4):749–759, 1976.
- [192] Smith QR, Momma S, Aoyagi M, and Rapoport SI. Kinetics of neutral amino acid transport across the blood-brain barrier. *J Neurochem*, 49(5):1651–1658, 1987.
- [193] Bauer D, Hamacher K, Bröer S, et al. Preferred stereoselective brain uptake of D-serine – a modulator of glutamatergic neurotransmission. *Nucl Med Biol*, 32(8):793–797, 2005.
- [194] Neims AH, Zieverink WD, and Smilack JD. Distribution of D-amino acid oxidase in bovine and human nervous tissues. *J Neurochem*, 13(3):163–168, 1966.
- [195] Weimar WR and Neims AH. The development of D-amino acid oxidase in rat cerebellum. *J Neurochem*, 29(4):649–656, 1977.
- [196] Yamaguchi M. Distribution of D-amino acid oxidase in rat tissues. *Showa Igakkai Zasshi*, 28(7):443–445, 1968.
- [197] HE Sauberlich. Studies on the toxicity and antagonism of amino acids for weanling rats. *J Nutr*, 75(1):61–72, 1961.
- [198] Kaltenbach JP, Ganote CE, and Carone FA. Renal tubular necrosis induced by compounds structurally related to D-serine. *Exp Mol Pathol*, 30(2):209–214, 1979.
- [199] Tsai GE, Yang P, Chang YC, and Chong MY. D-alanine added to antipsychotics for the treatment of schizophrenia. *Biol Psychiatry*, 59(3):230–234, 2006.
- [200] Neumann KD, Villanueva-Meyer JE, Mutch CA, et al. Imaging active infection in vivo using d-amino acid derived pet radiotracers. *Sci Rep*, 7(1):7903, 2017.
- [201] Yen YF, Le Roux P, Bok R, et al. Apparent T2 of 13C-labeled metabolites in vivo. In *Proceedings of the 16th Annual Meeting of ISMRM*, volume 1747, 2008.

Acknowledgements

I would certainly not be here without the help and support of many people.

To my thesis advisor, Rolf, thank you welcoming in your lab and giving me the opportunity to work in such an extraordinary environment. I was inspired by your deep knowledge in everything MR-related and am grateful for the feedbacks and comments you provided through the years.

To my thesis co-advisor, Hikari, thank you for being so patient in guiding me, for bearing with all my questions seemingly not minding having to repeat the same concept over and over, and for making chemistry understandable to me. I feel lucky to have had the chance to work and learn from you.

To Prof. Jensen, Prof. Wagner and Prof. Ansermet, thank you for accepting to be part of my thesis committee, for reviewing my manuscript and for providing me with insightful comments and feedback on my research.

To the CIBM vet team: Analina, Mario, Stefan and Valentine, I am forever grateful for your assistance in all that concerned animal experiments throughout the years and for the many late nights you put up with. I would not have been able to get to the end of my PhD without your precious help.

To the DNP and modeling team: thank you for the fruitful discussions, insights, support and help you provided through the years. Un grosso grazie goes to Andrea, thank you for your guidance on the solid-state projects, I really enjoyed working with you. That one week in Denmark was definitely the most productive week of my PhD. Claudia, thank you for always being there and lending a hand or an ear whenever I needed it. I really enjoyed the time we spent together these past years, the coffee breaks, sports sessions, trips, writing retreats... I loved all of it. Emma, my ISMRM roommate. I love your contagious good mood and enthusiasm. And, looking back at them, I even loved our body-attack days. Steffen and Thanh, my two great office mates: thank you for creating a fun and supportive atmosphere in the office and for always being up for ice cream. And thank you Thanh for taking such good care of my basil. To Jérémie and Rajesh, best lunch buddies, Irene, Ting, Stefan and Radek I loved all our swimming/skiing/travelling adventures. And to the other PhDs and researchers of the lab, thank you for always being there for a chat. Thank you Yves for always being willing to help with anything coil-related, and Lillian for your invaluable support.

Acknowledgements

To Europol ITN lot, I really enjoyed being part of such a fun group and am grateful for the ideas, knowledge and experiences we shared during our yearly meetings. It was a big pleasure to know you all.

Last but not least un enorme grazie goes to my friends and family, I would not be here was it not for your constant encouragement and support.

Lausanne, March 2021

Alice

Publications and conference proceedings

Publications in peer-reviewed scientific journals

Radaelli A, Grütter R, Yoshihara HAI. “*In vivo* detection of Damino acid oxidase with hyperpolarized D[1-¹³C]alanine”. NMR in Biomed 2020, 33, 7:e4303. DOI: <https://doi.org/10.1002/nbm.4303>

Radaelli A, Yoshihara HAI, Nonaka H, Sando S, Ardenkjaer-Larsen JH, Grütter R, Capozzi A. “¹³C dynamic nuclear polarization using SA-BDPA at 6.7 T and 1.1 K: coexistence of pure thermal mixing and well-resolved solid effect”. J Phys Chem Lett 2020, 11, 16:6873-6879. DOI: <https://doi.org/10.1021/acs.jpclett.0c01473>

Radaelli A, Hata R, Sando S, Bonny O, Comment A, Grütter R, Yoshihara HAI. “Probing renal pH and aminopeptidase N activity using hyperpolarized L-[1-¹³C]alaninamide”. *Manuscript in preparation*.

Zanella CC, Capozzi A, Yoshihara HAI, **Radaelli A**, Arn LP, Grütter R, Bastiaansen JAM. “Radical-free hyperpolarized MRI using endogenous pyruvate analogs and UV-induced nonpersistent radicals”. *In revision, NMR in Biomed*.

Previous work

Adelnia F, Arosio P, Mariani M, Orsini F, **Radaelli A**, Sangregorio C, Borsa F, Walsh JP, Winpenny R, Timco G, Lascialfari A. “NMR study of spin dynamics in V₇Zn and V₇Ni molecular rings”. Appl Magn Reson 2020. DOI: <https://doi.org/10.1007/s00723-020-01281-3>

Publications in peer-reviewed conference proceedings

Radaelli A, Capozzi A, Yoshihara HAI, Mishkovsky M, Comment A, Grütter R. “Effects of glassing matrix deuteration on ⁶Li dynamic nuclear polarization at 7 T”. Experimental Nuclear Magnetic Resonance Conference (ENC), Asilomar (USA) 2017 (traditional poster).

Publications and conference proceedings

Radaelli A, Yoshihara HAI, Grütter R. “Detection of D-amino acid oxidase activity using hyperpolarized molecular probes”. Annual meeting of the International Society for Magnetic Resonance (ISMRM), Paris (FR) 2018 (oral presentation).

Radaelli A, Yoshihara HAI, Hata R, Sando S, Grütter R. “Probing renal pH and aminopeptidase N activity with hyperpolarized [1-¹³C]alaninamide”. Annual meeting of the International Society for Magnetic Resonance (ISMRM), Paris (FR) 2018 (electronic poster).

Radaelli A, Hata R, Sando S, Bonny O, Comment A, Grütter R, Yoshihara HAI. “Probing renal pH using hyperpolarized [1-¹³C]alaninamide”. HYP18: An International Conference on Nuclear Hyperpolarization, Southampton (UK) 2018 (oral presentation).

Flatt E, **Radaelli A**, Capozzi A, Hyacinthe JN, Yoshihara HAI, Grütter R, Mishkovsky M. “Exploring the potential of hyperpolarized ⁶Li to study lithium bio-distribution in the rat brain”. HYP18: An International Conference on Nuclear Hyperpolarization, Southampton (UK) 2018 (traditional poster).

Radaelli A, Grütter R, Yoshihara HAI. “Flow attenuation and saturation-recovery to discriminate between intracellular and inflowing species in renal hyperpolarized ¹³C MRS”. Annual meeting of the International Society for Magnetic Resonance (ISMRM), Montreal (CA) 2019 (electronic poster).

Radaelli A, Capozzi A, Can E, Nonanka H, Sando S, Comment A, Ardenkjaer-Larsen JH, Grütter R, Yoshihara HAI. “¹³C dDNP with SA-BDPA at 6.7 T, 1.1 K: an ideal system to discriminate transfer of Zeeman energy from dipolar energy”. Experimental Nuclear Magnetic Resonance Conference (ENC), Baltimore (USA) 2020 (traditional poster).

Zanella CC, Capozzi A, Yoshihara HAI, **Radaelli A**, Arn LP, Grütter R, Bastiaansen JAM. “Radical-free and metal-free hyperpolarized MRI using endogenous pyruvate analogs”. (Virtual) annual meeting of the International Society for Magnetic Resonance (ISMRM), 2020 (electronic poster).

ALICE RADAELLI

alice.radaelli@epfl.ch

+41 (0)21 6930586

EDUCATION

2015-present	PhD student in physics EPFL (CH)
2013–2015	Master of Physics , with a focus on condensed matter physics Università degli Studi di Milano (IT) Graduation grade: 110/110 with honors
2009-2013	Bachelor of Physics Università degli Studi di Milano (IT) Graduation grade: 104/110

FELLOWSHIPS

2015-2018	Partner fellow of the Marie Curie Europol ITN , within Horizon 2020
09/2013-03/2014	LLP Erasmus scholarship at Universität Leipzig (DE)

WORK EXPERIENCE

2016-2020	Teaching assistant for general physics 1 and 2 courses, EPFL
-----------	---

TECHNICAL SKILLS

Experimental	Liquid- and solid-state nuclear magnetic resonance (NMR), <i>in vivo</i> and <i>ex vivo</i> magnetic resonance spectroscopy and imaging (MRS, MRSI) experiments, cryogenics, dynamic nuclear polarization (DNP), electron spin resonance (ESR, EPR), SQUID magnetometry, handling of small animals, basic analytical chemistry techniques.
IT	C++, Matlab, LabView, Mathematica, OriginLab, Latex, Microsoft Office Windows and Linux operating systems

LANGUAGES

English	Fluent (C1/C2)
French	Intermediate (B2)
German	Beginner (A1)
Italian	Mother tongue

ADDITIONAL INFORMATION

Birth date: 15/11/1990, Italian citizenship